Système de Subduction

Séries calc-alcaline et Tholeitique

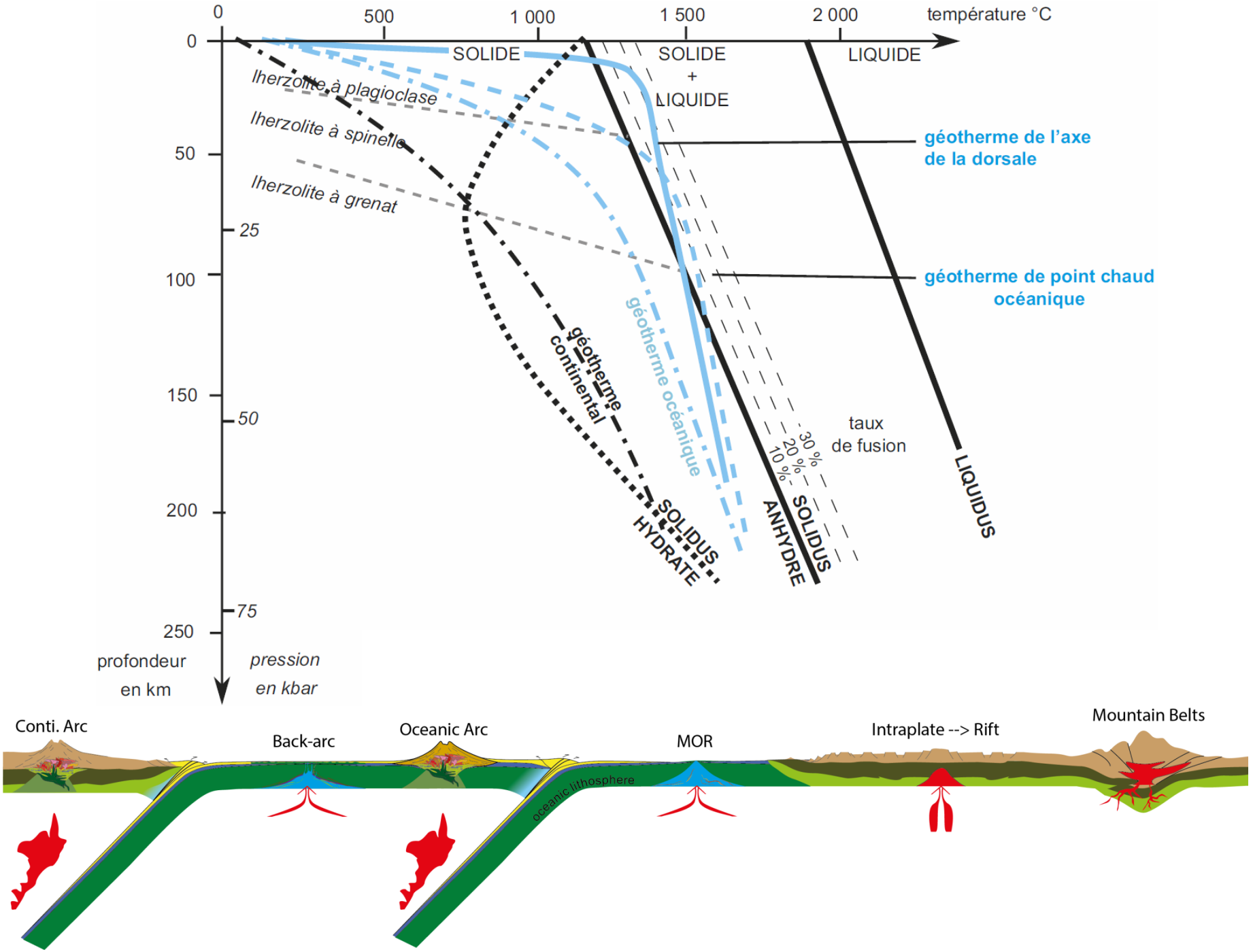
0
500
1 000
1 500
2 000
température °C
0
50
100
150
200
250
25
50
75
profondeur
en km
pression
en kbar
SOLIDE
SOLIDE
+
LIQUIDE
LIQUIDE
lherzolite à plagioclase
lherzolite à spinelle
lherzolite à grenat
géotherme de l'axe
de la dorsale
géotherme de point chaud
océanique
géotherme
continental
géotherme océanique
SOLIDUS
HYDRATE
SOLIDUS
ANHYDRE
LIQUIDUS
taux
de fusion
30 %
20 %
10 %
Conti. Arc
Back-arc
Oceanic Arc
MOR
Intraplate --> Rift
Mountain Belts
oceanic lithosphere

Les magmas d'arcs sont la deuxieme forme dominante du volc. actif

MORB: 20 km^3/yr
Arc: 6 km^3/yr
OIB: 2 km^3/yr

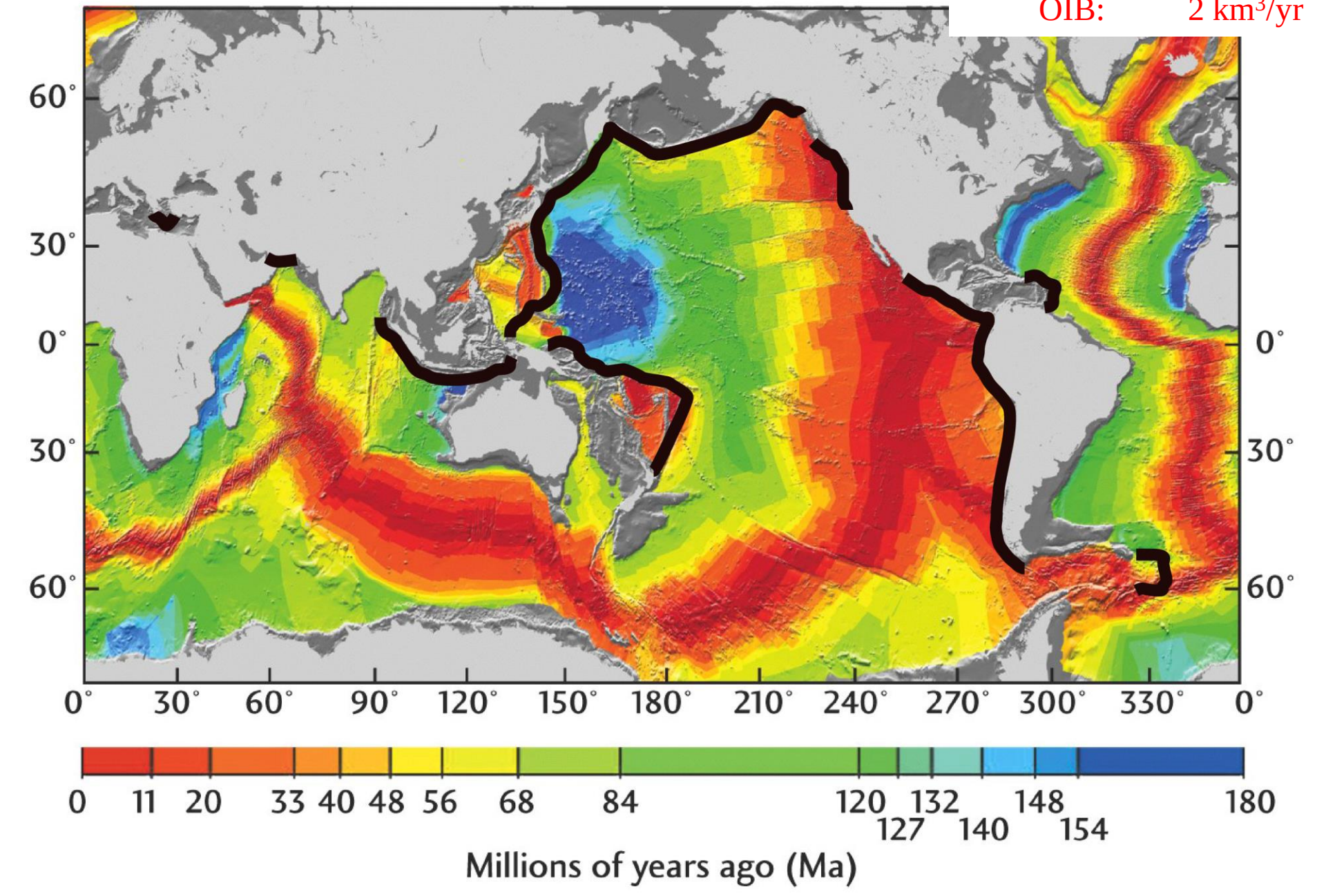

Les magmas d'arcs sont la deuxieme forme dominante du volc. actif

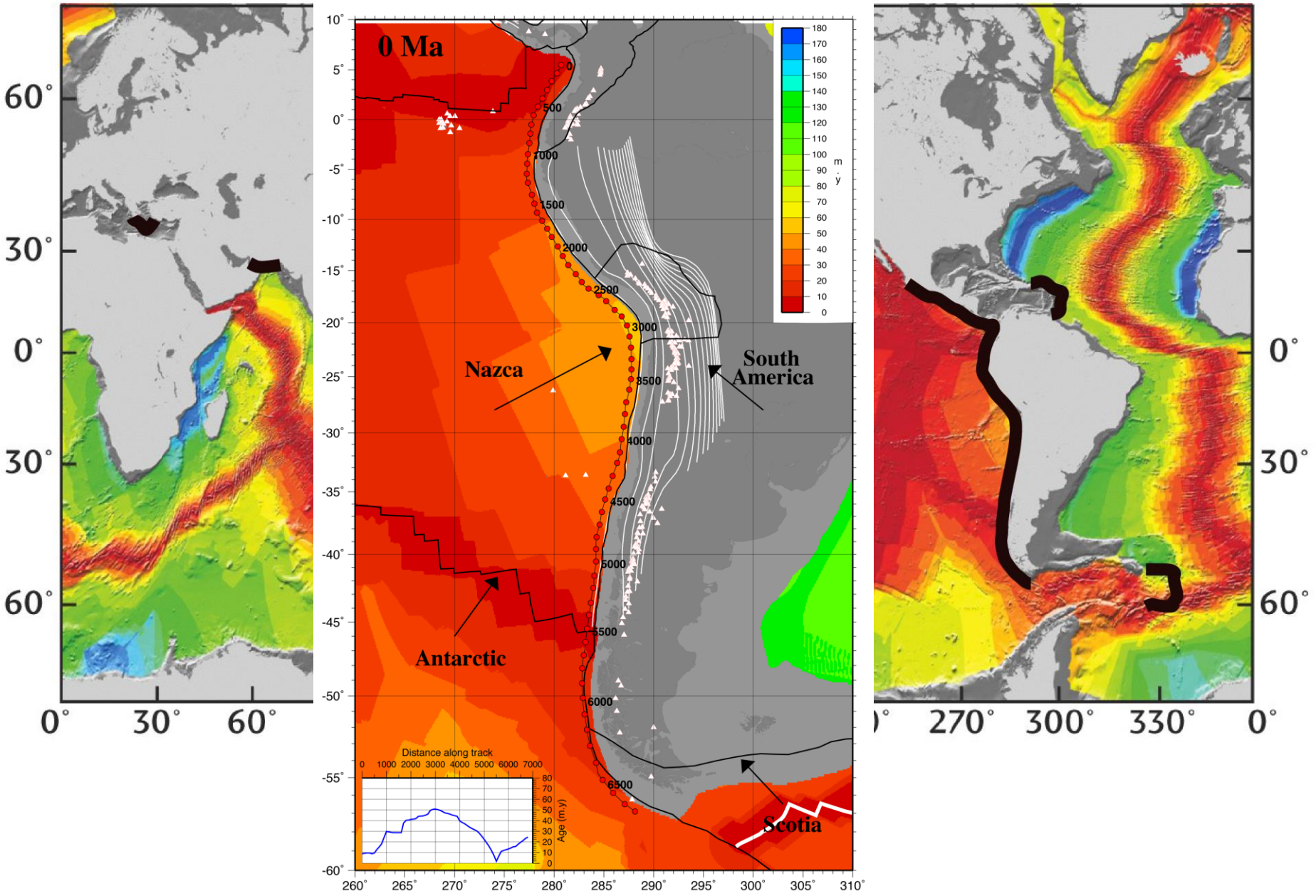

Les magmas d'arcs sont la deuxieme forme dominante du volc. actif

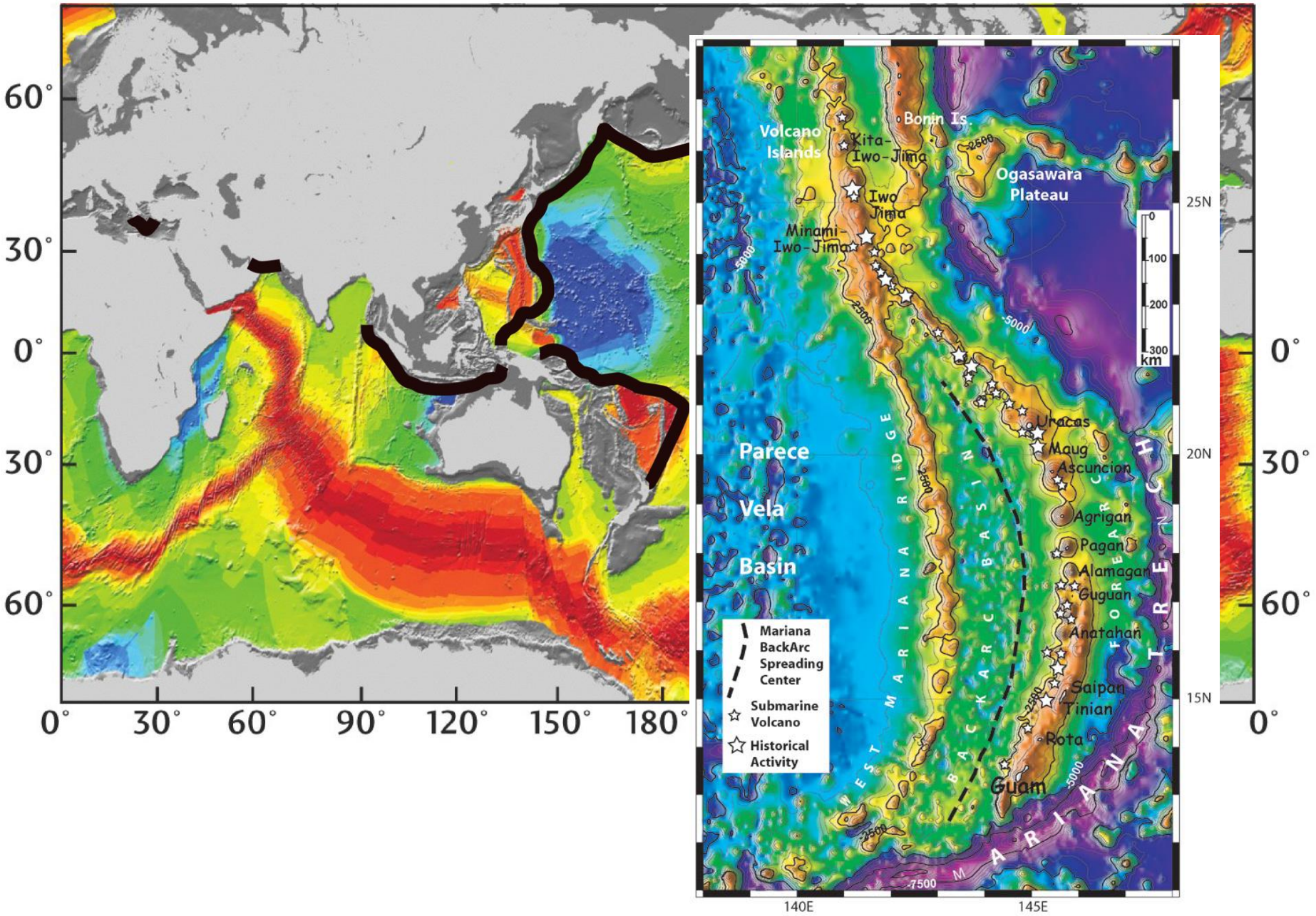

Site de recyclage des elements

Croute

Metaux precieux, Risque volcanique

Climats

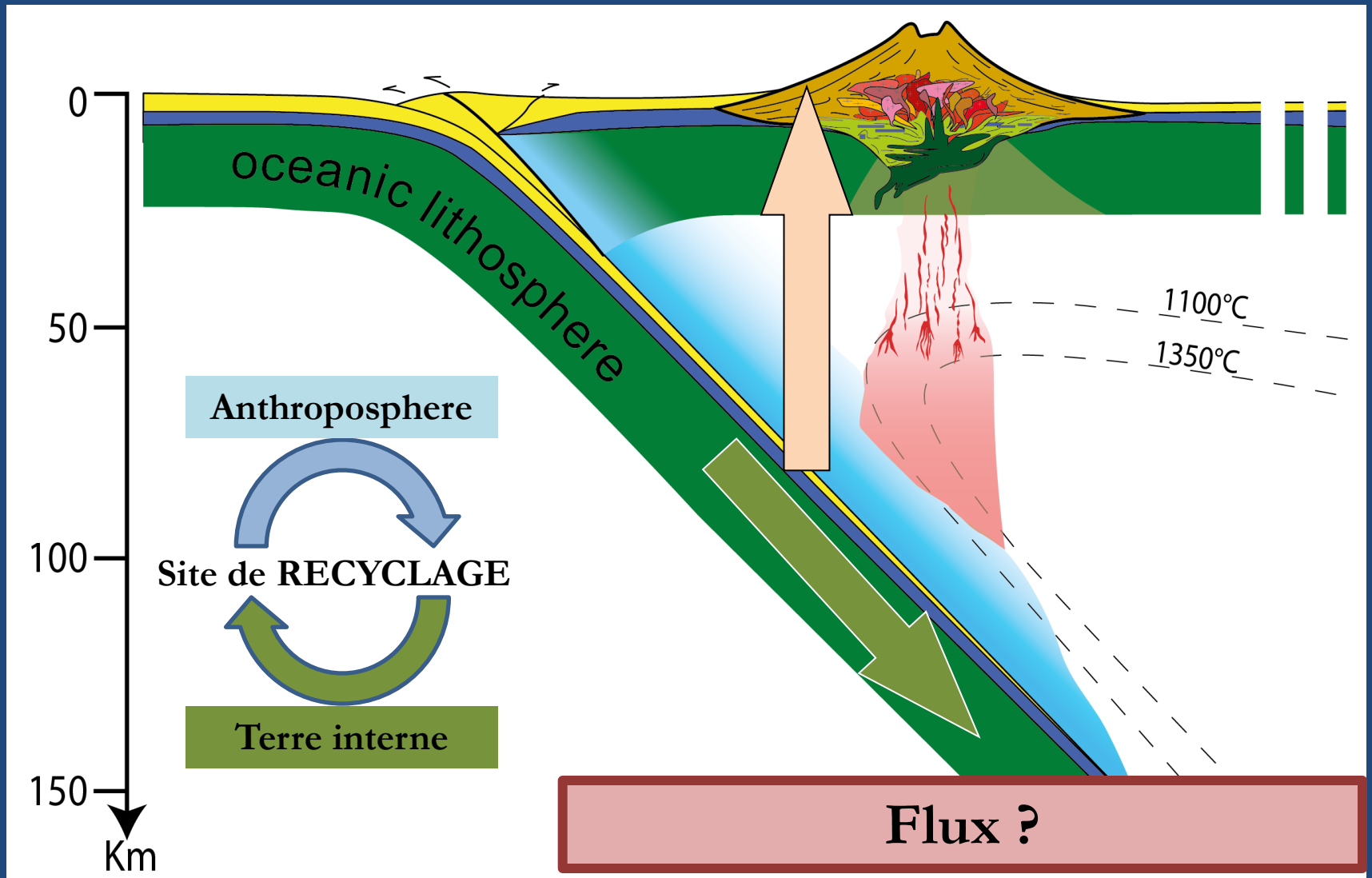

GEOPHYSICAL RESEARCH LETTERS, VOL. 10, NO. 11, PAGES 1061-1064, NOVEMBER 1983

NO WATER, NO GRANITES - NO OCEANS, NO CONTINENTS

I.H. Campbell* and S.R. Taylor

Conclusions

Our main thesis is simple. Water is essential for the formation of granites and granite, in turn, is essential for the formation of stable continents. The earth is the only planet with granite and continents because it is the only planet with abundant water.

H_2O et croute continentale

Oceans (Basaltique) ← **Subduction = Arcs** → **Continents** (Evolués)

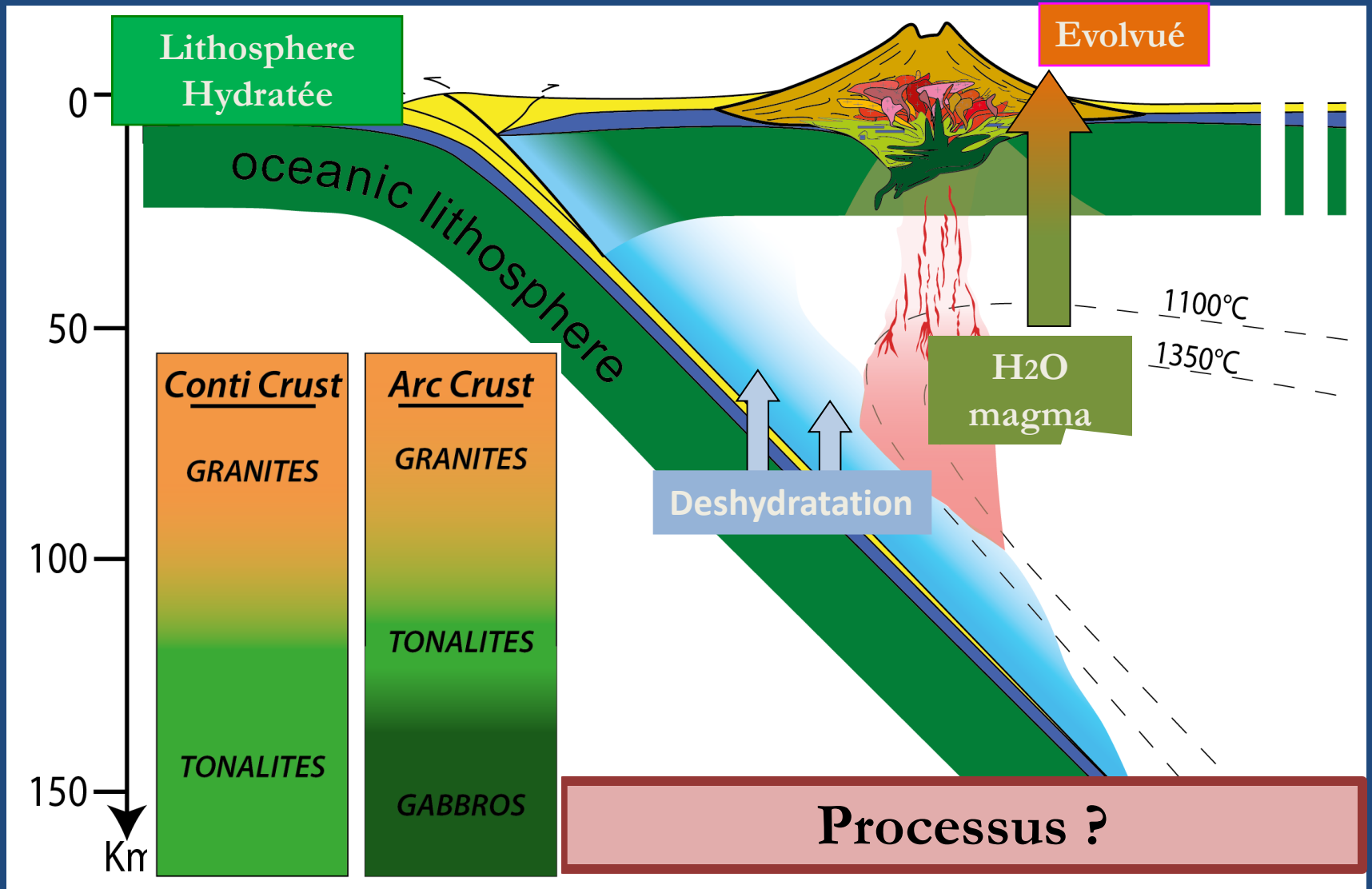

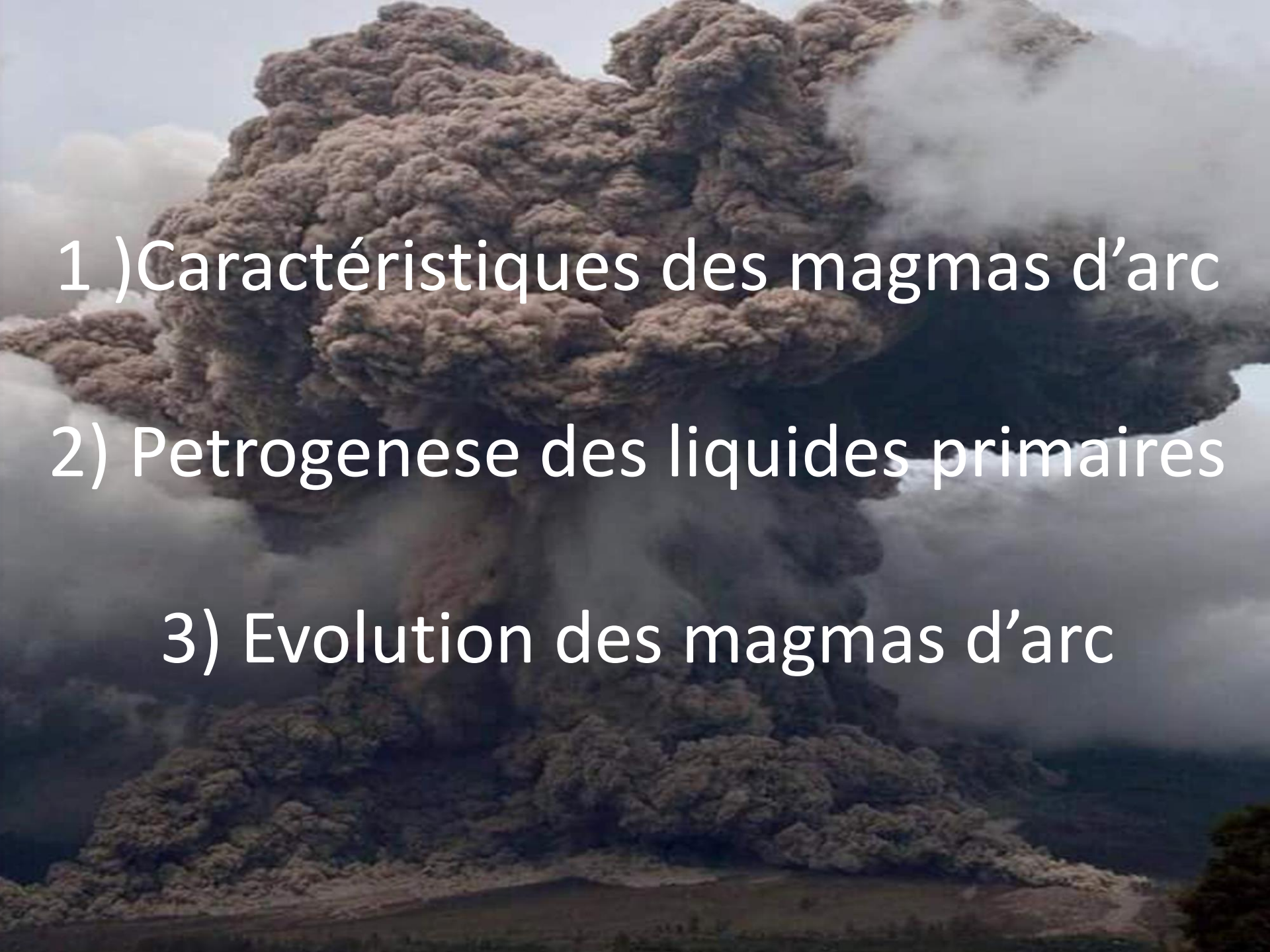

1)Caractéristiques des magmas d’arc

2) Petrogenese des liquides primaires

3) Evolution des magmas d’arc

1)Caractéristiques des magmas d’arc

Magma d'Arc =

Hydraté

(Phases hydratés / nature explosive / cortège minéralisé)

En géneral calc-alcalin

(Tholeitique / alcalin existe)

Plus Oxydé

que les autres magmas

Géochimie particulière

influencé par la plaque plongeante

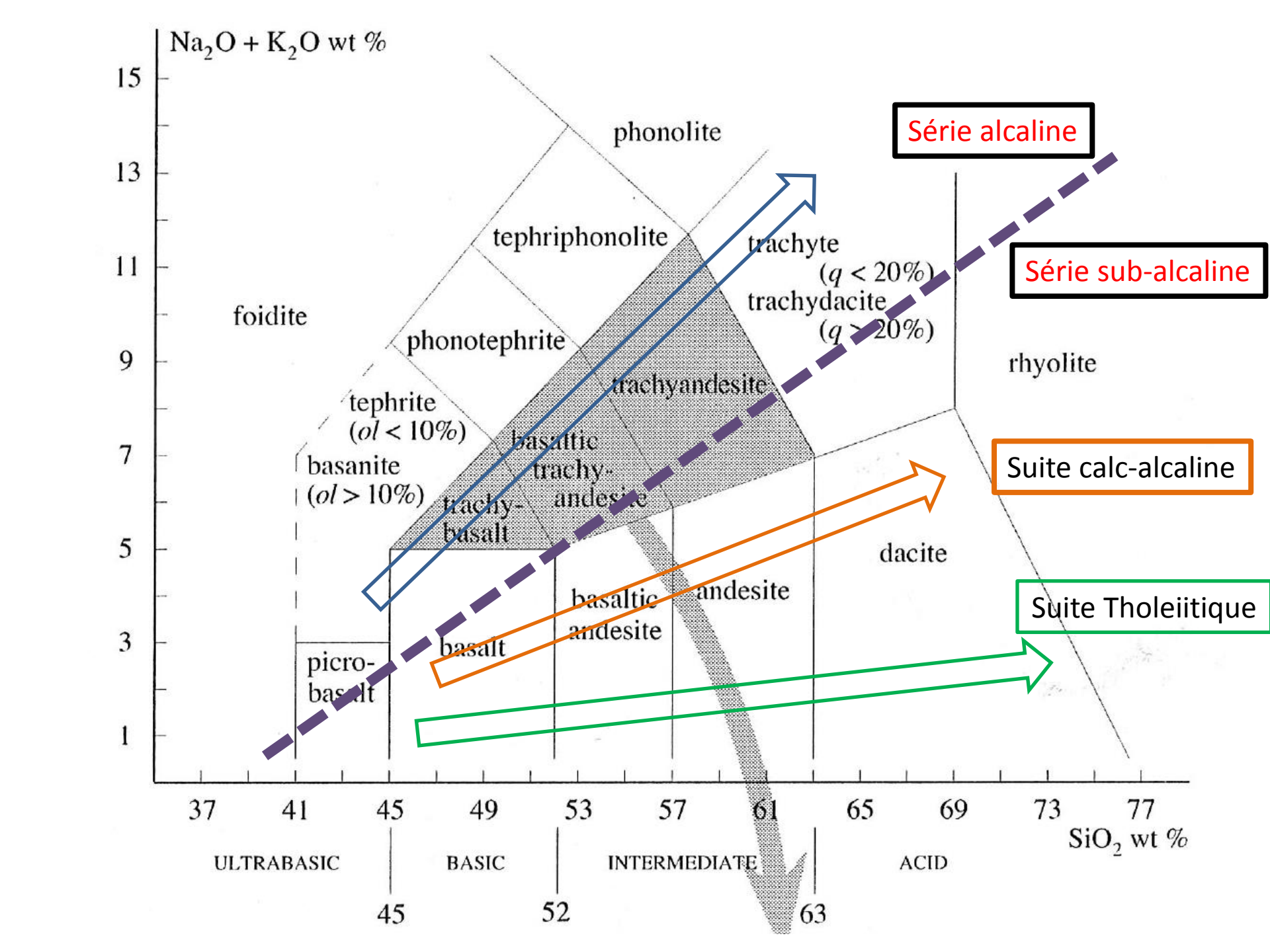
Na2O + K2O wt %
15
13
11
9
7
5
3
1
phonolite
tephriphonolite
foidite
phonotephrite
tephrite
(ol < 10%)
basanite
(ol > 10%)
trachyandesite
basaltic
trachy-
andesite
trachy-
basalt
trachyte
(q < 20%)
trachydacite
(q > 20%)
rhyolite
dacite
basaltic
andesite
andesite
basalt
picro-
basalt
37
41
45
49
53
57
61
65
69
73
77
SiO2 wt %
ULTRABASIC
BASIC
INTERMEDIATE
ACID
45
52
63
Série alcaline
Série sub-alcaline
Suite calc-alcaline
Suite Tholeiitique

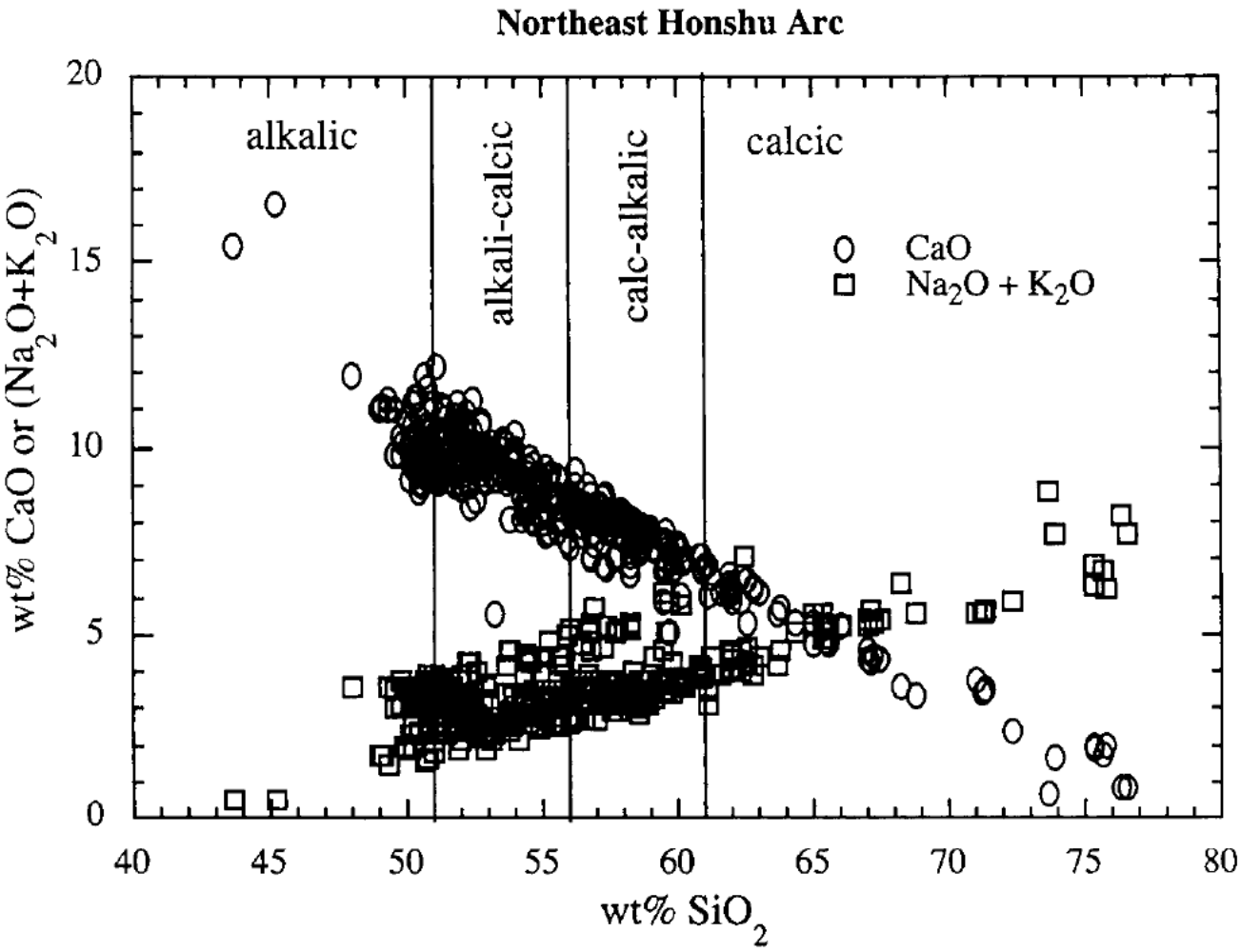

Fig. 1. Variations of wt % CaO and $Na_2O + K_2O$ vs wt % SiO_2 for bulk-rock compositions (major oxides, volatile-free, normalized to 100% totals) from the volcanic front of the NE Honshu (Japan) arc. Original named fields within wt % SiO_2 ranges are from Peacock (1931) and are applied to suites whose oxide variation trends intersect within a given field.

Zimmer 2010

Enrichissement en Fer

Etat d'oxydation → présence d'oxyde

H2O→ changement dans la suite de cristallisation

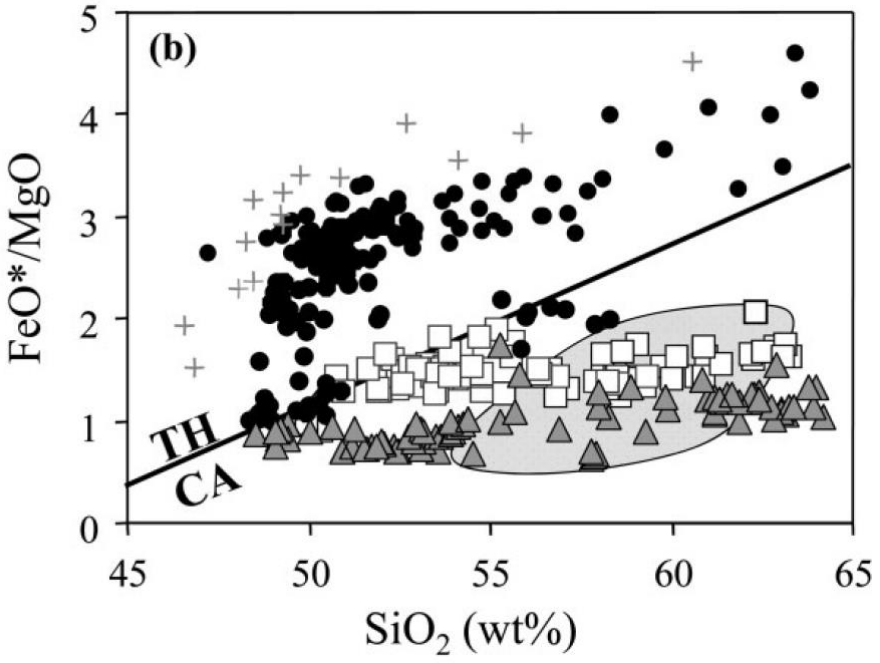

Miyashiro 1974

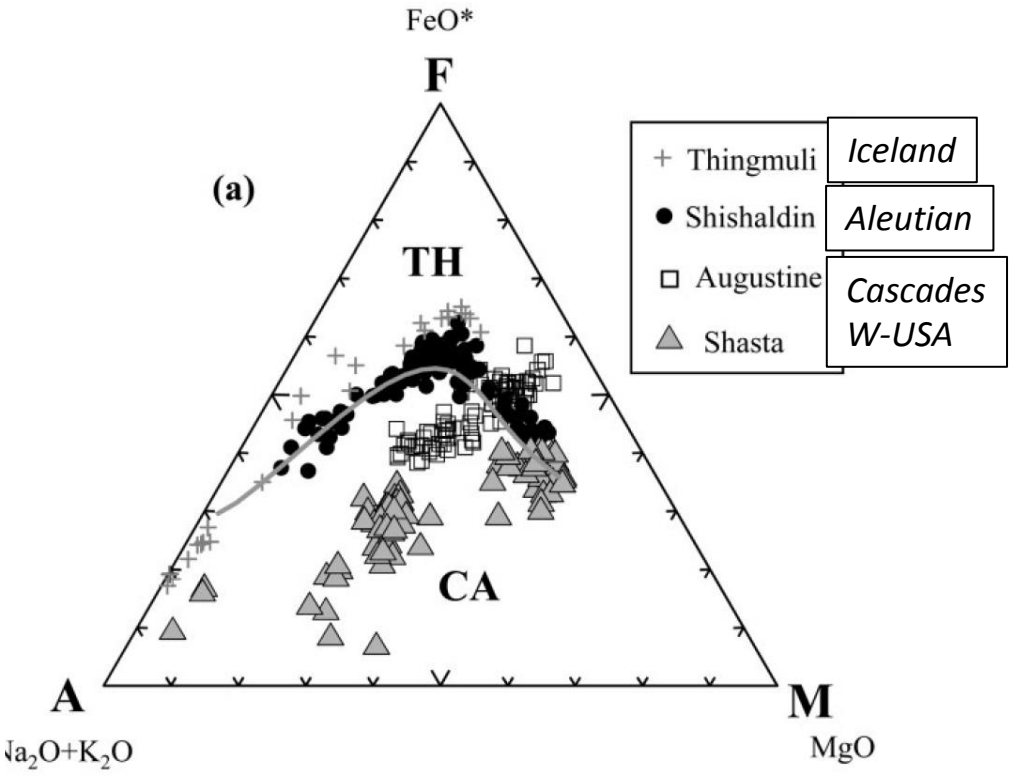

Irvine & Baragar, 1971

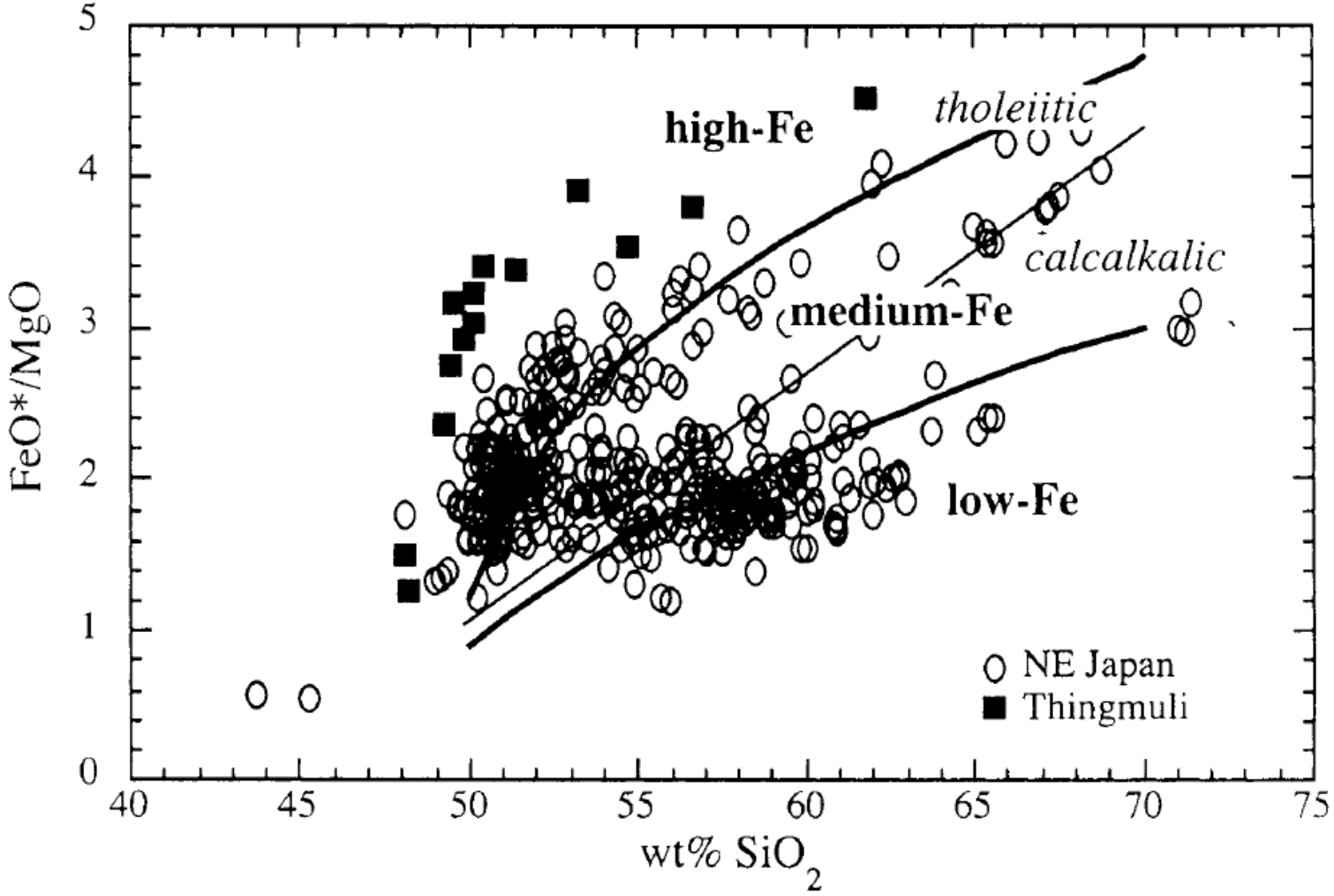

Fig. 3. Bulk-rock compositions from the volcanic front of the NE Honshu (Japan) arc (○) and Thingmuli volcano in Iceland from Carmichael (1964) (■) projected in terms of FeO^*/MgO vs wt % SiO_2 (major oxides, volatile-free, normalized to 100% totals). The discriminant boundary (fine line) between tholeiitic and calcalkalic (italicized) suites is from Miyashiro (1974). Coordinates for the proposed discriminant boundaries (bold lines) between low-, medium-, and high-Fe suites in FeO^*/MgO vs wt % SiO_2 space are:

wt % SiO_2	50	52·5	55	57·5	60	62·5	65	67·5	70
$FeO^*/MgO_{high\text{-}medium}$	1·20	2·25	2·85	3·32	3·67	3·95	4·24	4·50	4·80
$FeO^*/MgO_{medium\text{-}low}$	0·90	1·30	1·65	1·90	2·20	2·40	2·65	2·85	3·00

Serie Shoshonitique

Low K → Tholeitique
High K → Alcalin

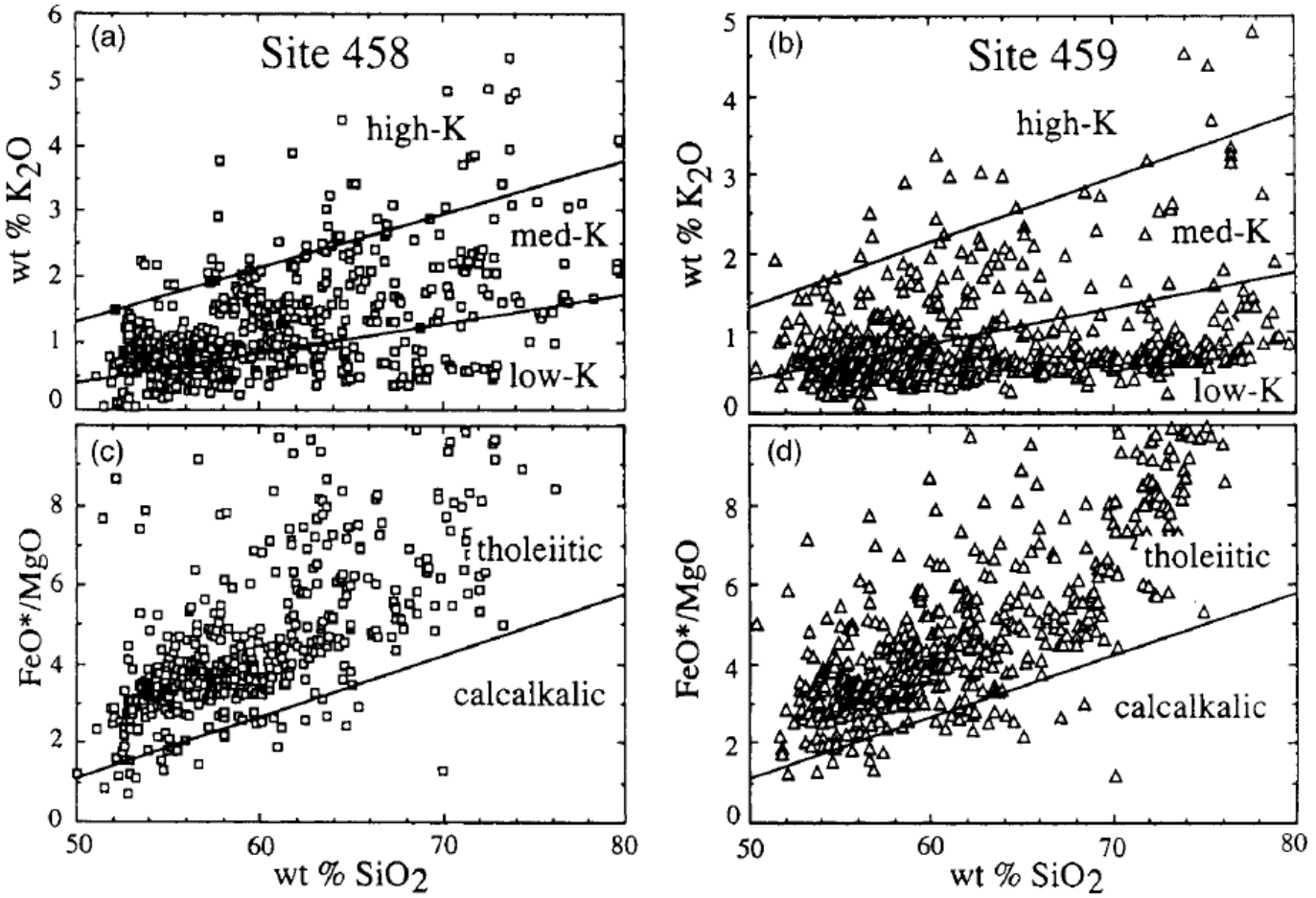

Fig. 4. Plots of wt % K_2O and FeO^*/MgO vs wt % SiO_2 for individual glass shard compositions (determined by electron microprobe analysis; Arculus *et al.*, 1995) recovered in the Mariana forearc (Deep Sea Drilling Project Sites 458 and 459), sourced from Tertiary–Quaternary arc eruptions. Discriminant boundaries in (a) and (b) are from Gill (1981) and in (c) and (d) from Miyashiro (1974). It should be noted that for both Sites, there is no coupled relationship between the K_2O contents and the FeO^*/MgO as a function of wt % SiO_2, wherein med-K samples by the Gill (1981) criterion are automatically calcalkalic by the Miyashiro (1974) discriminant.

Zimmer 2010

THI = Fe4 / Fe8

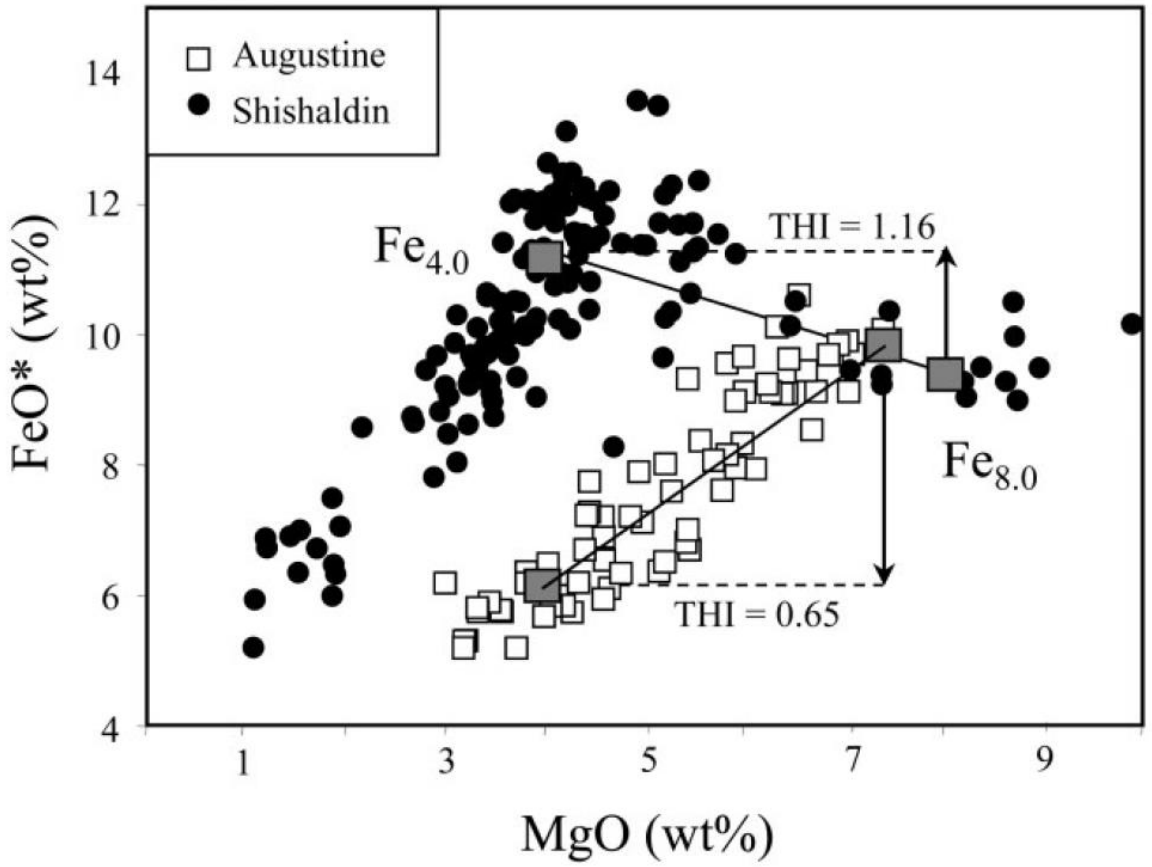

Fig. 3. Calculation of the THI (Tholeiitic Index) = $Fe_{4\cdot0}/Fe_{8\cdot0}$. $Fe_{4\cdot0}$ is the average FeO* concentration of samples between 3 and 5 wt % MgO. If there are sufficient data (as for Shishaldin), $Fe_{8\cdot0}$ is the average FeO* concentration of samples between 7 and 9 wt % MgO; if not, then the sample with the highest MgO is used to approximate $Fe_{8\cdot0}$ (as for Augustine). Shishaldin has a tholeiitic trend (THI > 1); Augustine has a strongly calc-alkaline trend (THI < 1).

Zimmer 2010

THI = Fe4 / Fe8

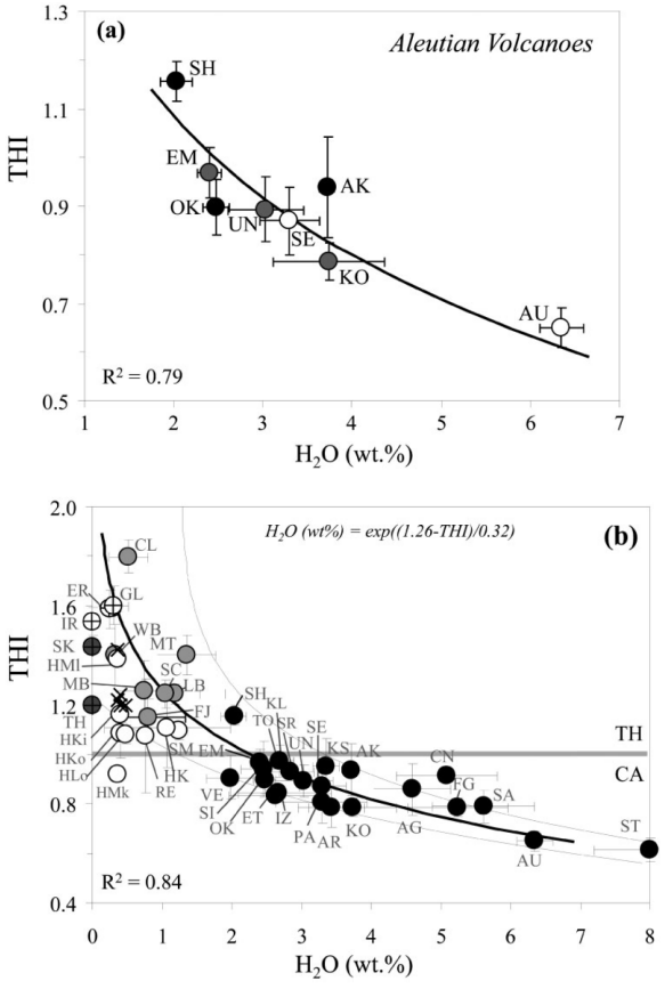

Fig. 7. THI vs H_2O. (a) THI and average maximum magmatic water content measured in melt inclusions (as in Fig. 6) for eight volcanoes from the Aleutian volcanic arc (Table 1). Abbreviations as in Fig. 5. Filled circles are TH, open circles are CA, and gray circles are transitional, based on the SiO_2 vs FeO*/MgO diagram of Miyashiro (1974). (b) THI vs H_2O for arcs (filled circles), back-arc basins (gray circles), ocean islands (open circles), and mid-ocean ridges (open circles with crosses). THI for two layered mafic intrusions (gray circles with crosses) shown at 0 wt % H_2O (no measured H_2O). THI for Hawaii is also shown as calculated at maximum FeO* (×; see text for details). Regions lacking water data (plotted at 0% H_2O) and ocean islands are not included in regression. THI error bars (2σ standard error) are propagated from standard deviation of the mean $Fe_{4\text{-}0}$ and $Fe_{8\text{-}0}$, and H_2O error bars are 1σ standard deviation (see Table 1 for values and abbreviations). Best-fit curve (logarithmic) to data determined by reduced major axis regression. The 95% confidence interval on H_2O (dashed lines, read horizontally off the *x*-axis) gives a roughly similar error (~±2 wt %) at both high and low water contents. Data sources and a description of THI and H_2O calculations for volcanoes outside the Aleutians are given in Electronic Appendix A.

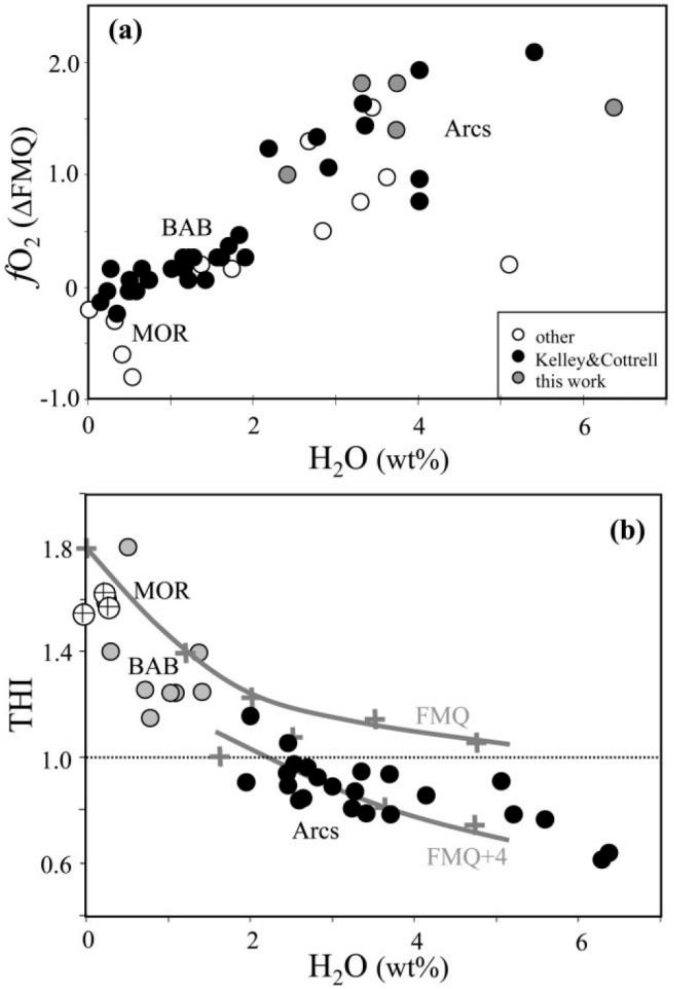

Fig. 9. (a) Estimates of fO_2 vs H_2O in different magmas. Most data are from Kelley & Cottrell (2009) and this study (see Table 2 for data summary and Electronic Appendix G for a more detailed list of data, techniques, and references). (b) Interplay of H_2O and fO_2 on the THI. Data points as in Fig. 7b (excluding OIB and degassed Shishaldin). Grey plus signs and thick lines were calculated from the experimental study of Berndt *et al.* (2005) for MORB composition (B1) equilibrated along two fO_2 buffers. The data point at FMQ and 0 wt % H_2O is estimated from Galapagos data of Juster *et al.* (1989).

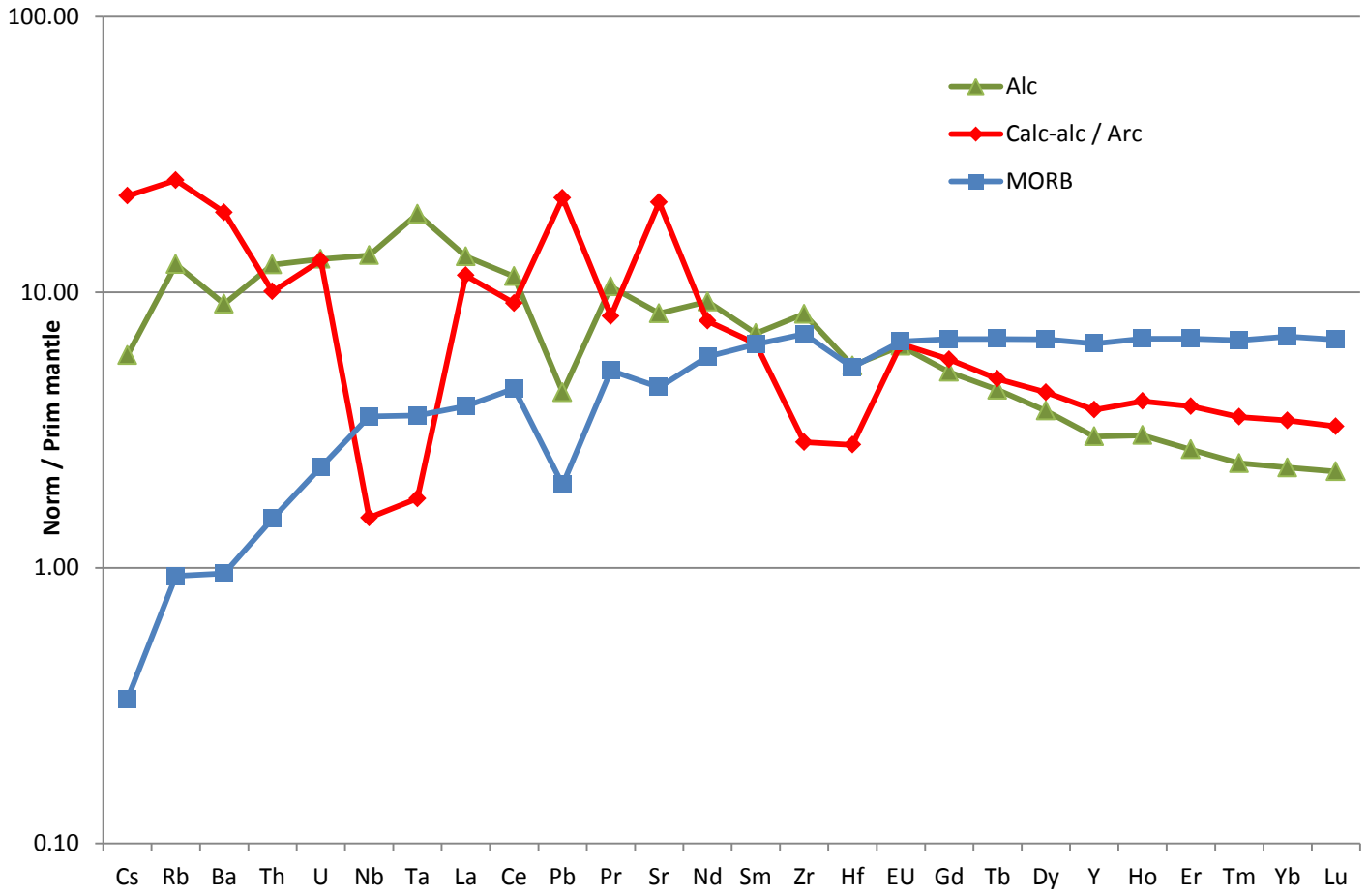
100.00
10.00
1.00
0.10
Norm / Prim mantle
Alc
Calc-alc / Arc
MORB
Cs Rb Ba Th U Nb Ta La Ce Pb Pr Sr Nd Sm Zr Hf EU Gd Tb Dy Y Ho Er Tm Yb Lu

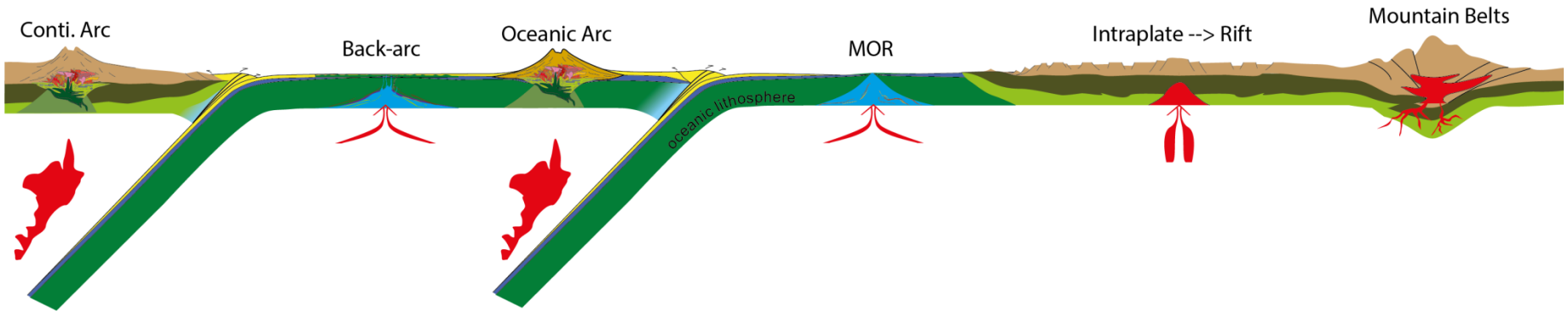
Conti. Arc
Back-arc
Oceanic Arc
MOR
Intraplate --> Rift
Mountain Belts
oceanic lithosphere

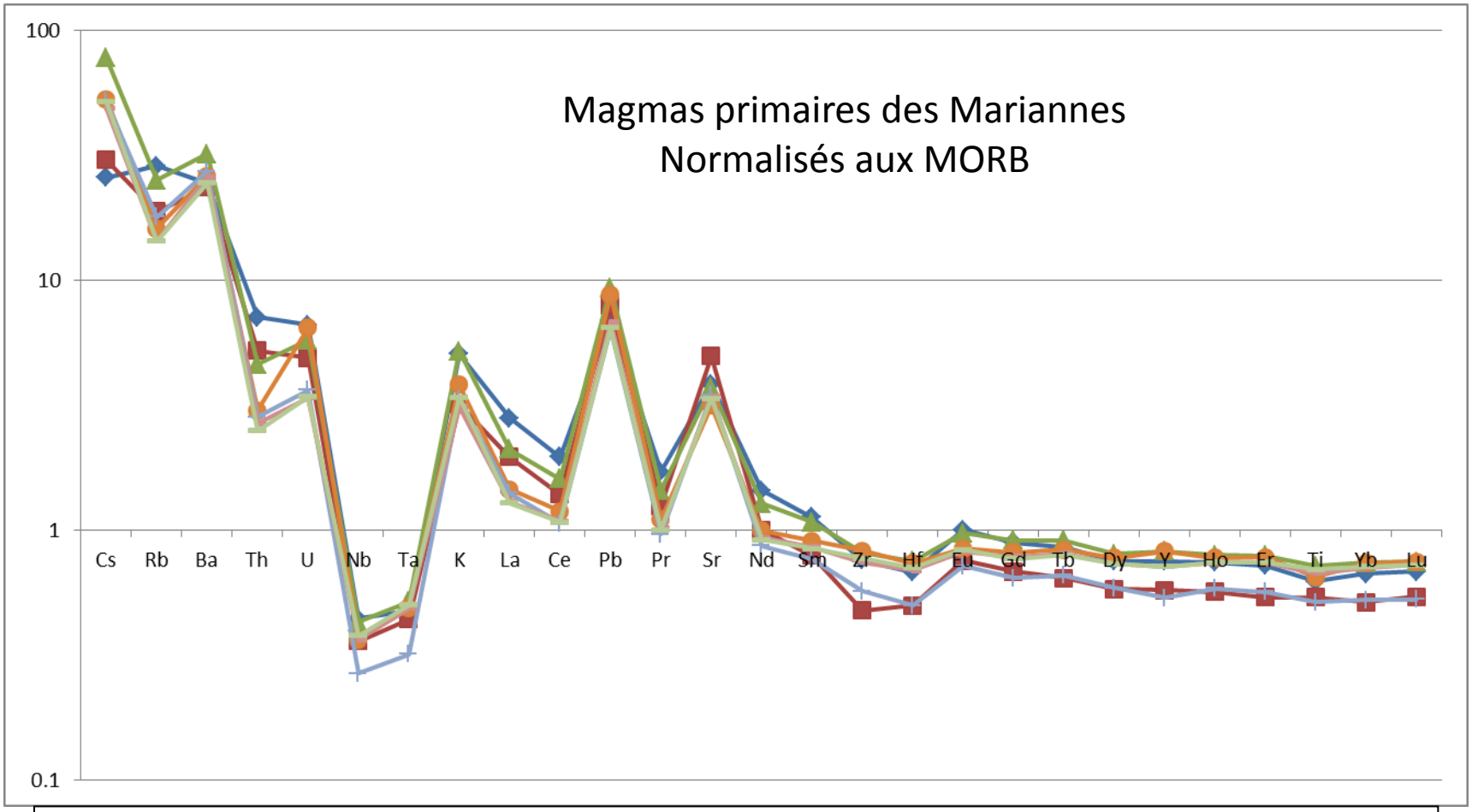

Enrichissement en LILE (Cs, Rb, Ba, Rb, K)
Pb, et Sr (Fluides mobile); mais aussi Th et U
Anomalies négative en HFSE (Nb, Ta, Zr, Hf, Ti).

Origine ?

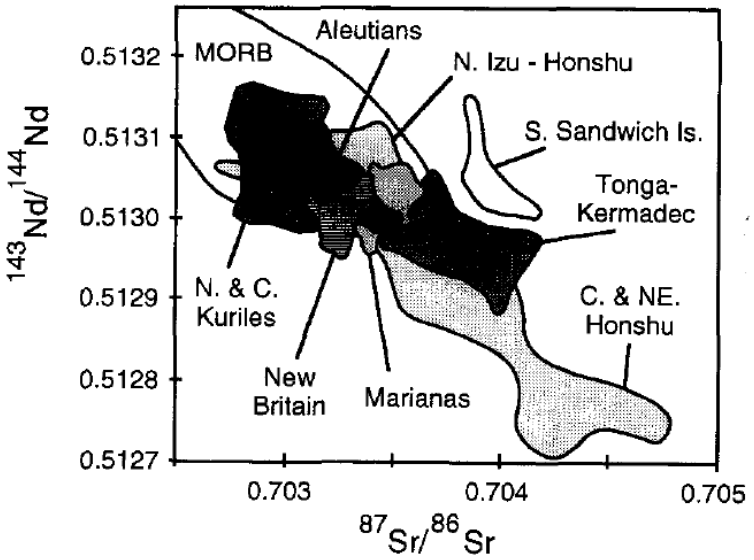

Arculus 94

Fig. 1. Variation of $^{143}Nd/^{144}Nd$ vs. $^{87}Sr/^{86}Sr$ of some intra-oceanic island arcs most similar to MORB, after Zhuravlev et al. (1985) and Hawkesworth et al. (1991). There is a considerable variation within the Hosnhu arc of Japan from MORB-like isotopic values to less (Nd) and more (Sr) radiogenic values respectively.

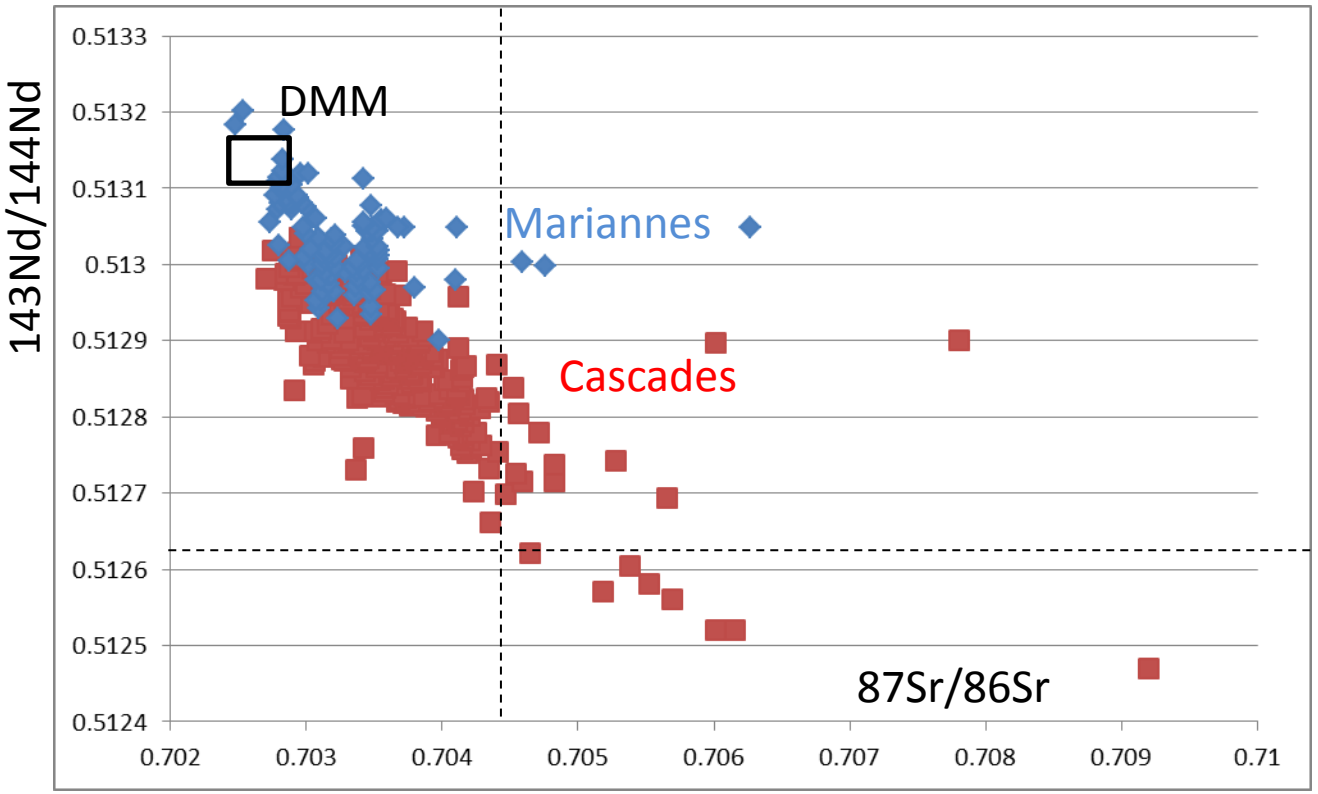

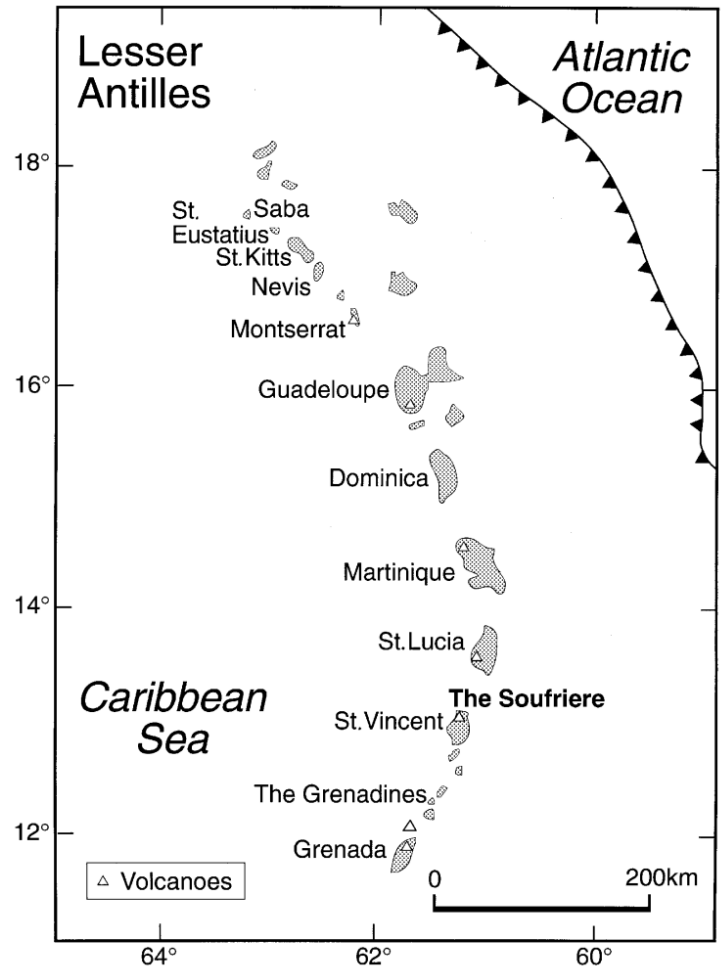
Lesser Antilles
Atlantic Ocean
Caribbean Sea
St. Eustatius
Saba
St. Kitts
Nevis
Montserrat
Guadeloupe
Dominica
Martinique
St. Lucia
The Soufriere
St. Vincent
The Grenadines
Grenada
Volcanoes
0
200km
18°
16°
14°
12°
64°
62°
60°

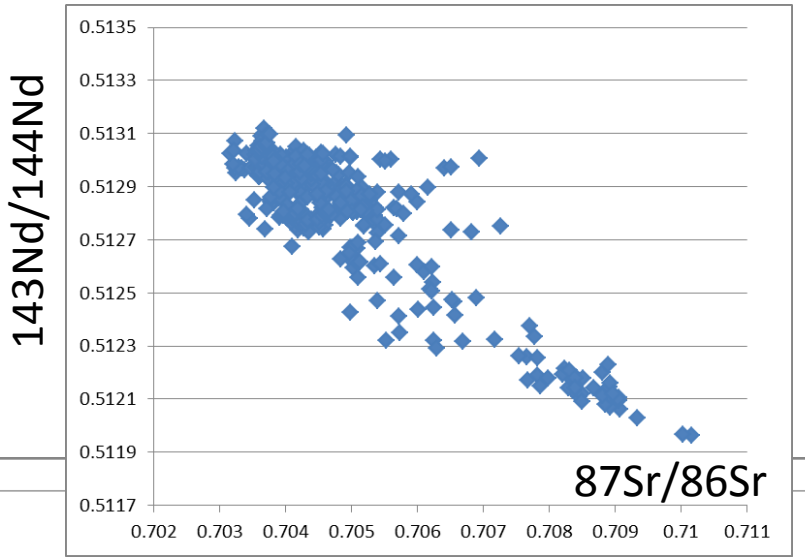
143Nd/144Nd
0.5135
0.5133
0.5131
0.5129
0.5127
0.5125
0.5123
0.5121
0.5119
0.5117
87Sr/86Sr
0.702
0.703
0.704
0.705
0.706
0.707
0.708
0.709
0.71
0.711

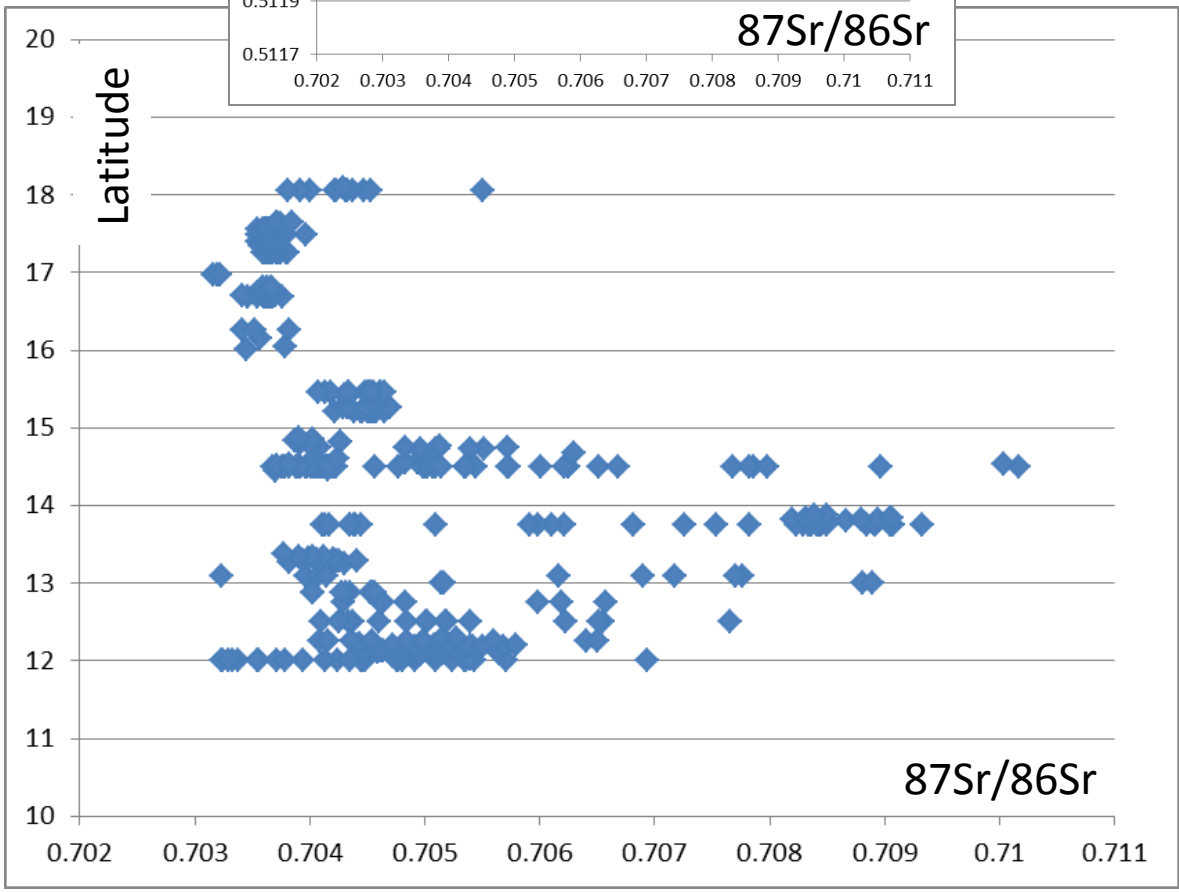
Latitude
20
19
18
17
16
15
14
13
12
11
10
87Sr/86Sr
0.702
0.703
0.704
0.705
0.706
0.707
0.708
0.709
0.71
0.711

Signature des magmas d' arc =
Processus du Slab (panneau plongeant)
Procesus de Fusion
Processus de transfert
et de differentiation

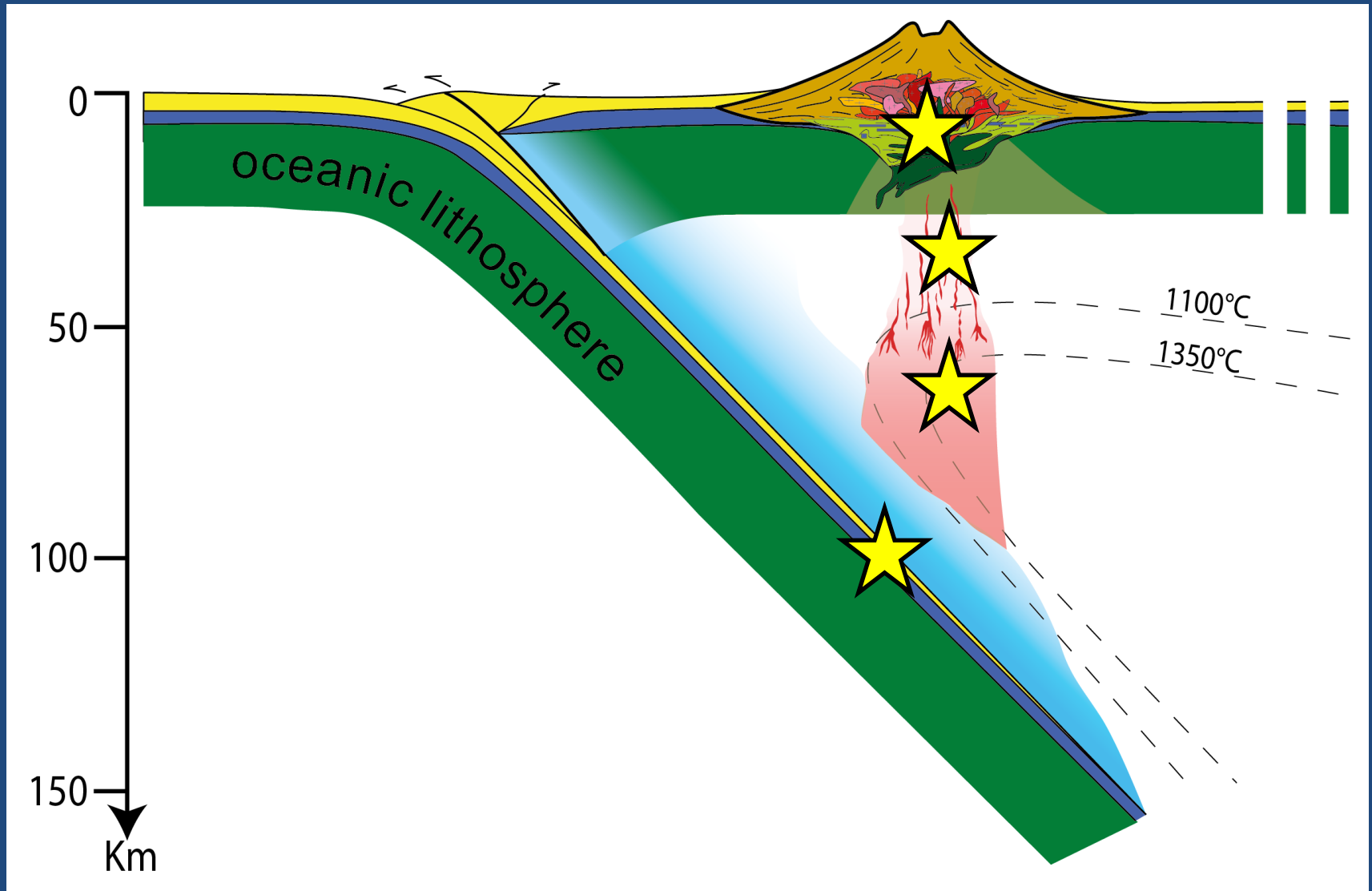

Ranero 2003

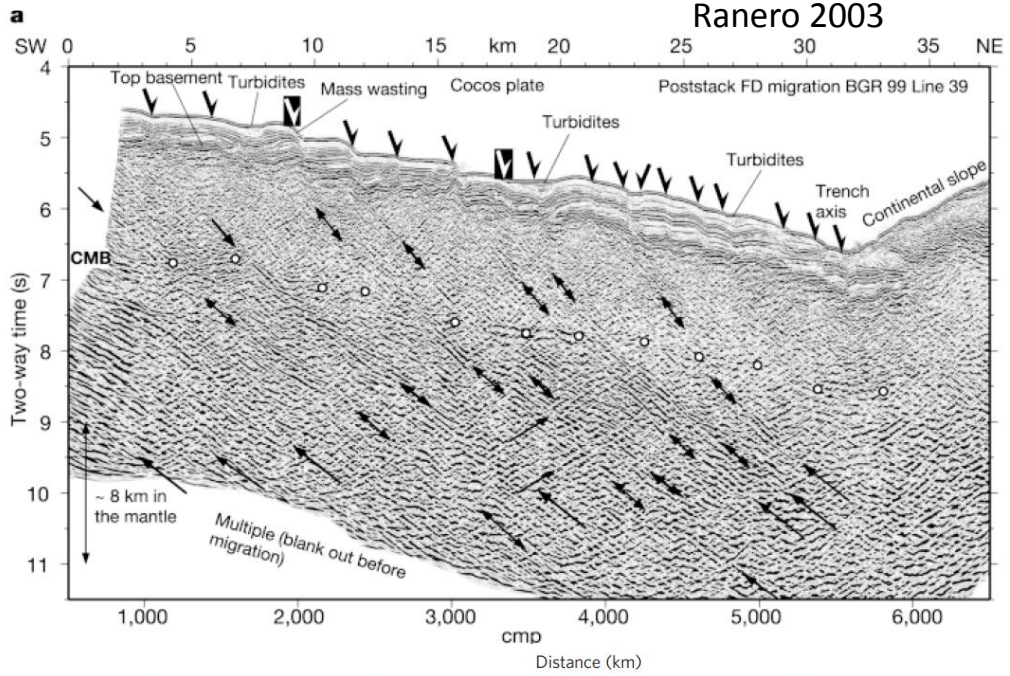

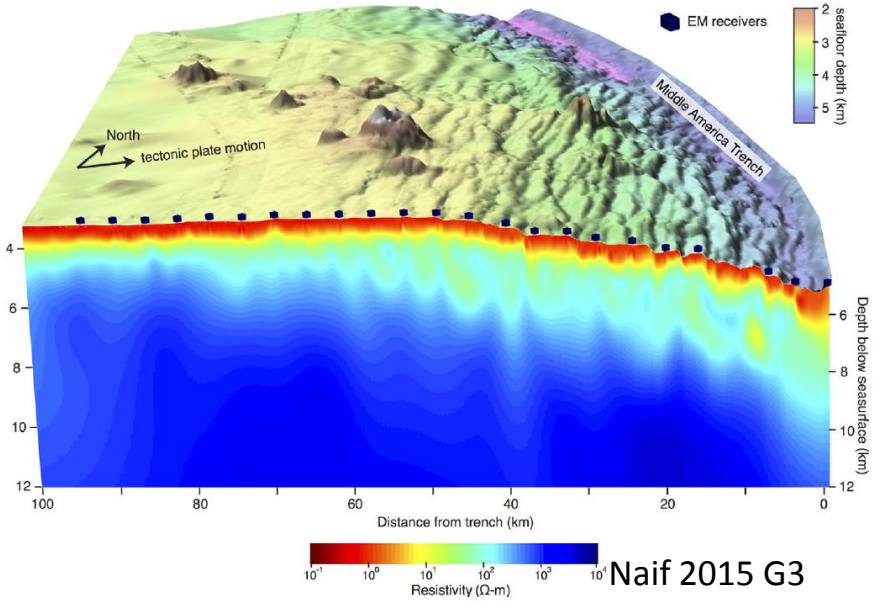

Naif 2015 G3

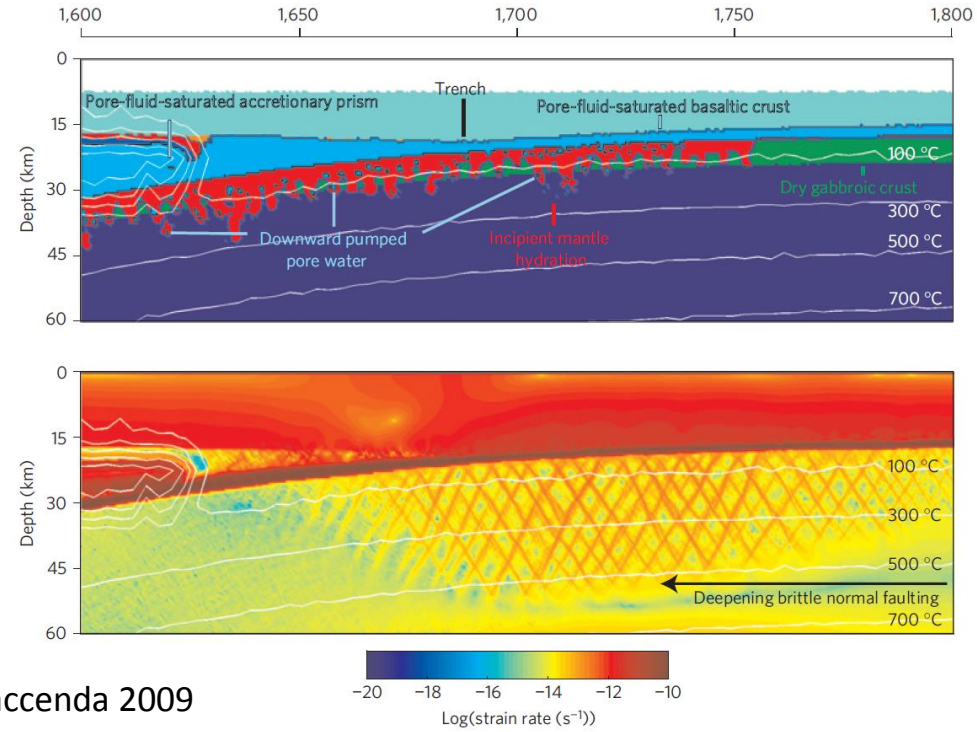

En plus de l'Hydratation à la ride
Importante hydratation
lors de la flexure du slab

Faccenda 2009

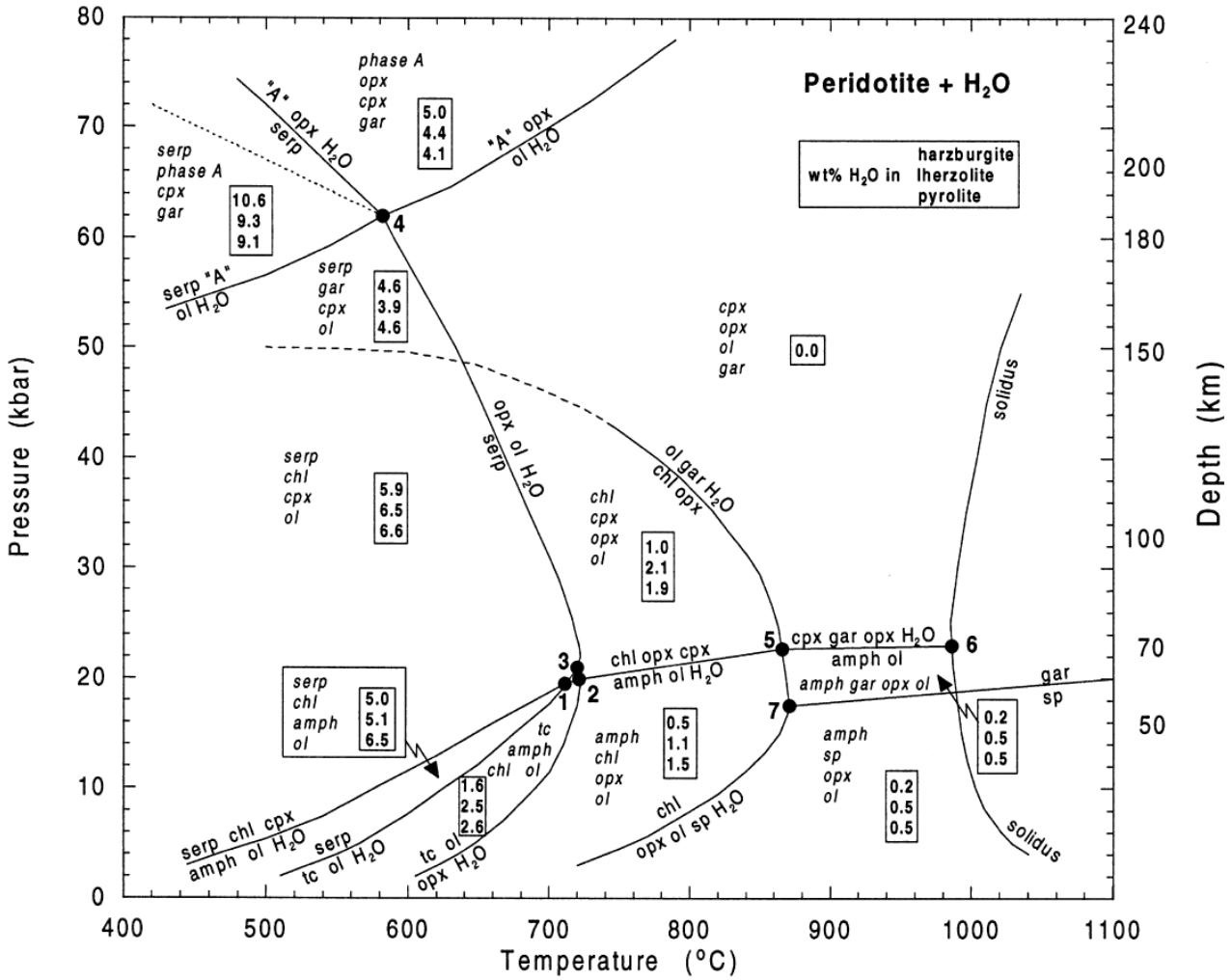

Fig. 5. Phase diagram for H_2O-saturated average mantle peridotite and maximum H_2O contents bound in hydrous phases in average peridotites. Upper value: harzburgite; middle value: lherzolite; lower value: pyrolite. The *italic* labels are assemblages in a given stability field. '*A*' = phase A, *amph* = amphibole, *chl* = chlorite, *cpx* = clinopyroxene, *gar* = garnet, *ol* = olivine, *opx* = orthopyroxene, *serp* = serpentine, *sp* = spinel, *tc* = talc.

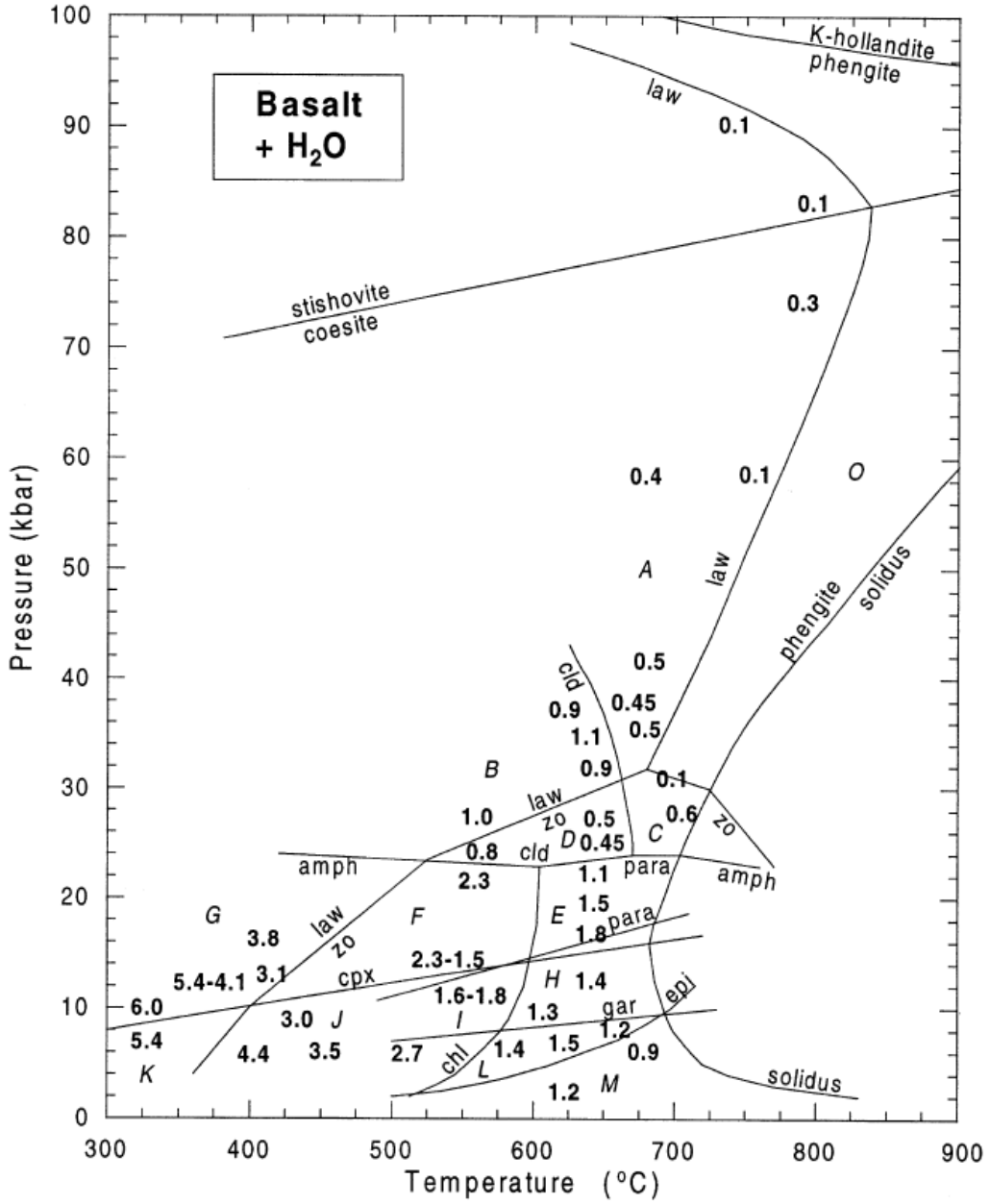

Fig. 3. Maximum H_2O contents bound in hydrous phases in H_2O-saturated MOR basalt. For assemblages and references see Table 3.

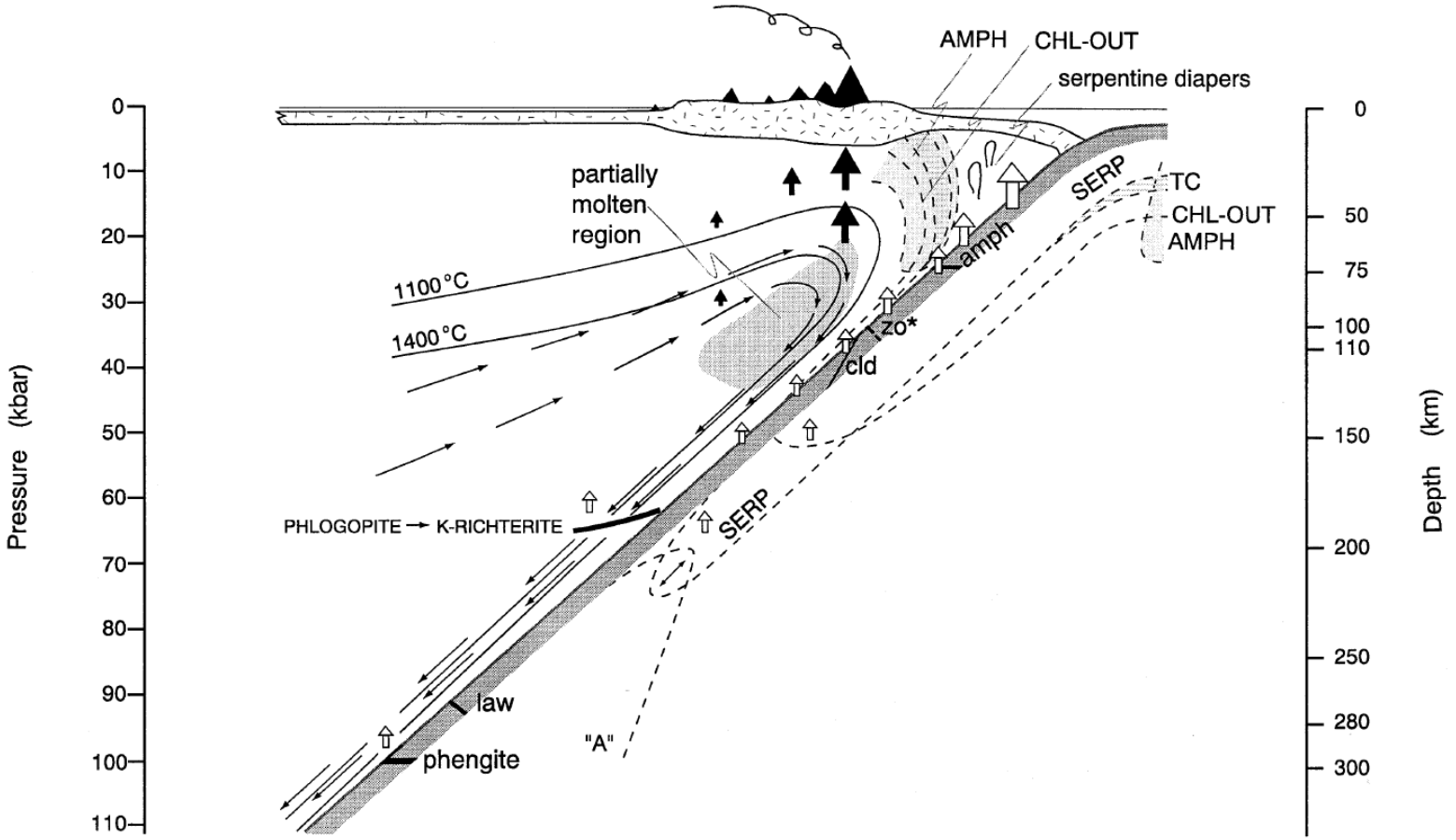

Fig. 8. Model for the formation of the volcanic front. Dehydration from peridotite and oceanic crust occurs at almost any depth to ca. 150–200 km, thus water will be generally available above the subducting lithosphere. The grey region in the mantle wedge will have a significant amount of melt present. The volcanic front forms where the amount of melt is sufficient to mechanically extract and give rise to arc magmatism. Open arrows indicate rise of fluid, short solid arrows indicate rise of melts. Long arrows indicate flow in the mantle wedge. Stippled lines outline stability fields of hydrous phases in peridotite; however, we do not want to imply that peridotite underlying the oceanic crust is fully hydrated. The striped region shows the zone where talc occurs in average peridotite compositions. In some thermal structures (Fig. 7b and c) a portion of the peridotitic lithosphere will be colder than 600°C at 62 kbar, serpentine will react to phase A and thus H_2O will be subducted to large depth. In the oceanic crust, temperatures can be low enough to preserve lawsonite and phengite to their maximum pressure stability; however, at somewhat warmer conditions (slower subduction, shallower angle, younger crust) zoisite (zo^*) will be the last potassium-free phase to decompose and the top of the oceanic crust (phengite rich sedimentary layer) might melt. Single phase transitions which cause a potassium-rich fluid pulse could be constituted by the pressure breakdown of phengite in oceanic crust and by the phlogopite to K-richterite reaction in previously K-metasomatized mantle.

Temperature !!
Slab geotherm
f (Age – Mtemp – Vitesse)

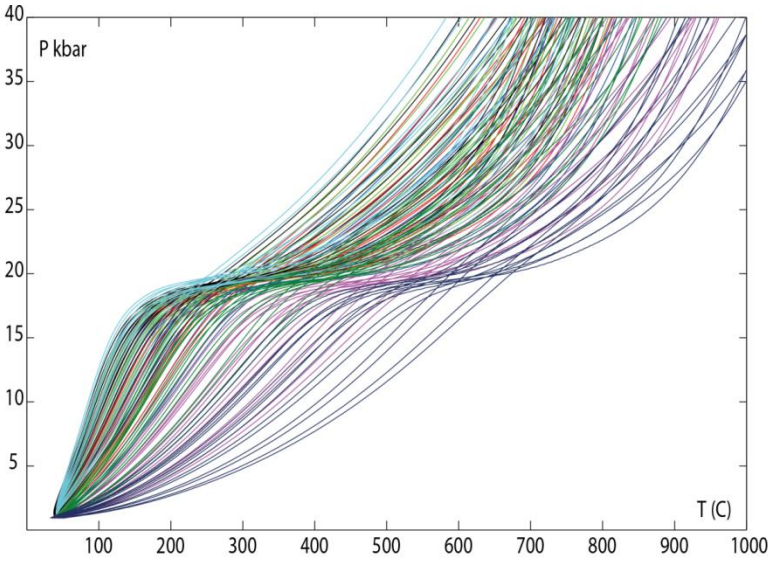

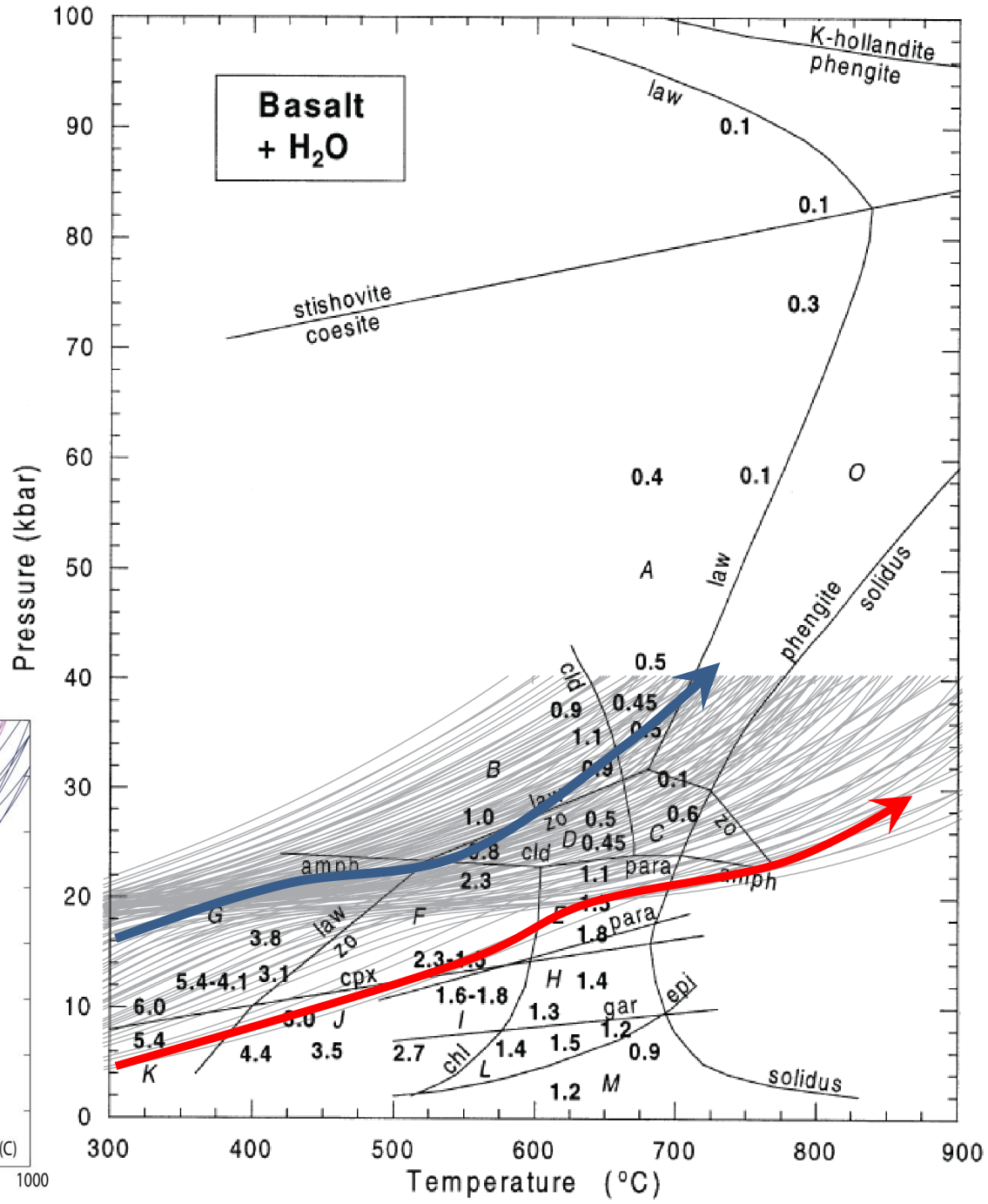

Magni et al. G3 2014

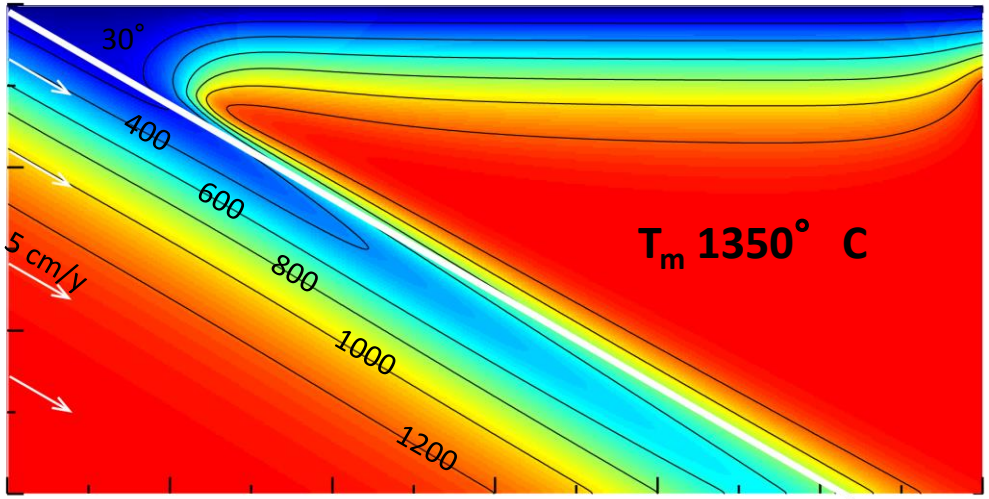

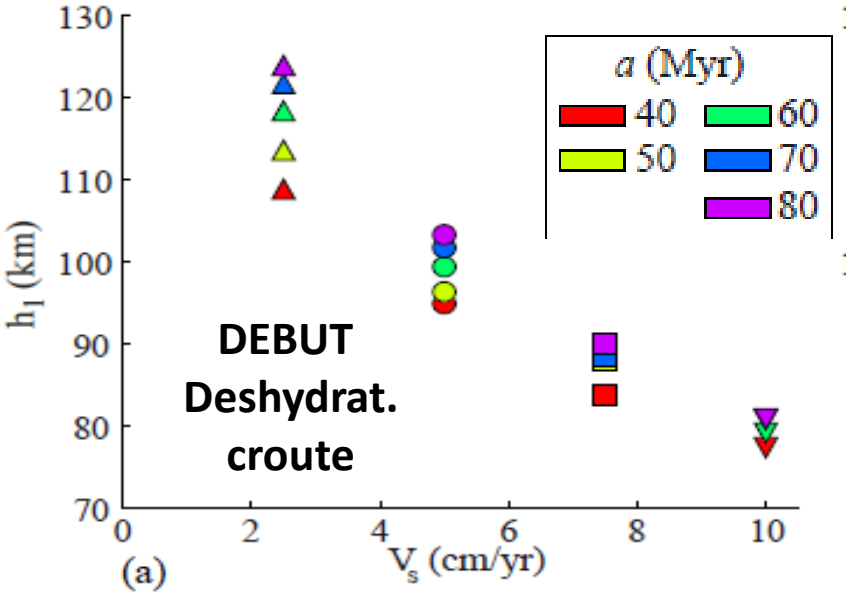

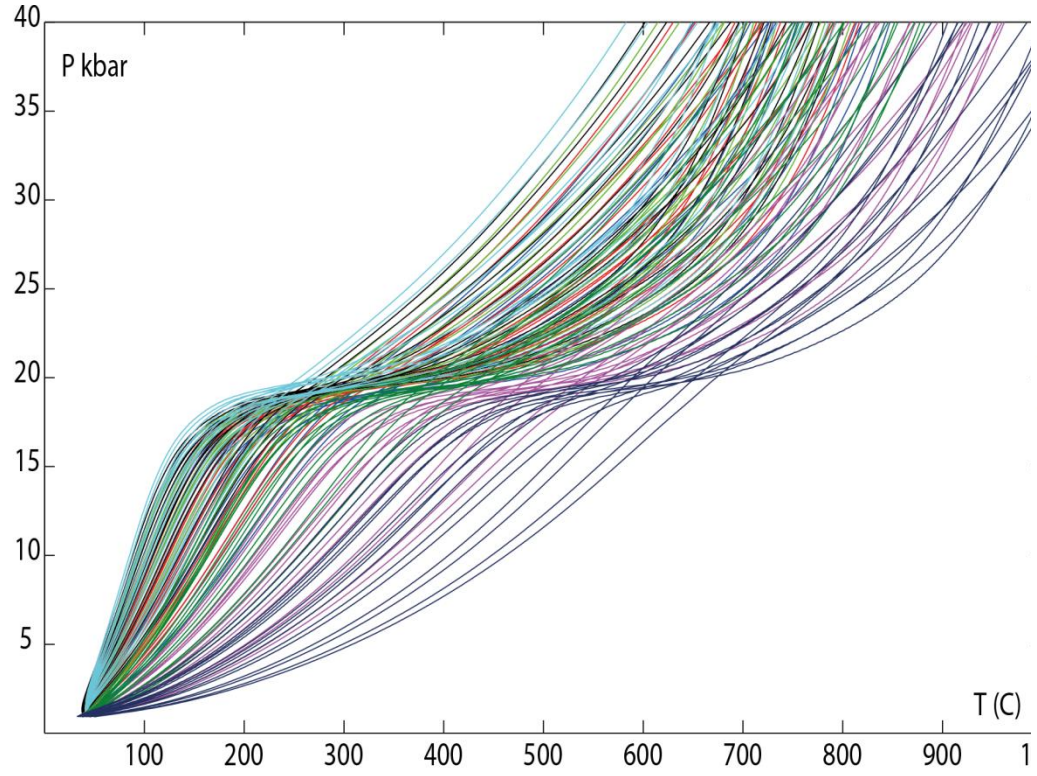

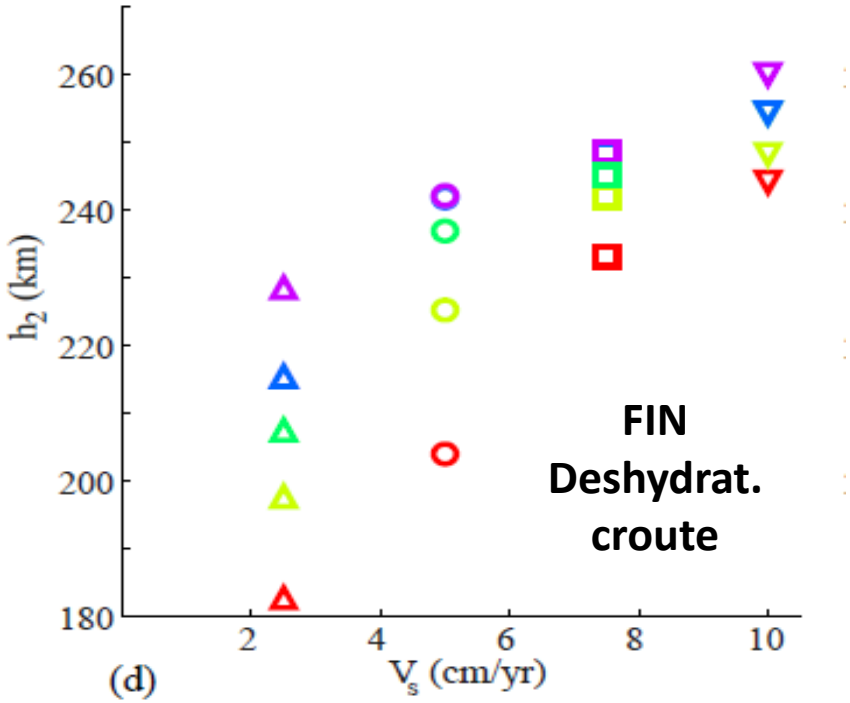

Supercritical fluids

Schmidt et Poli 2014

SCP :

Basalts: = 3.5 Gpa ?

Peridotite = 3.8 Gpa ?

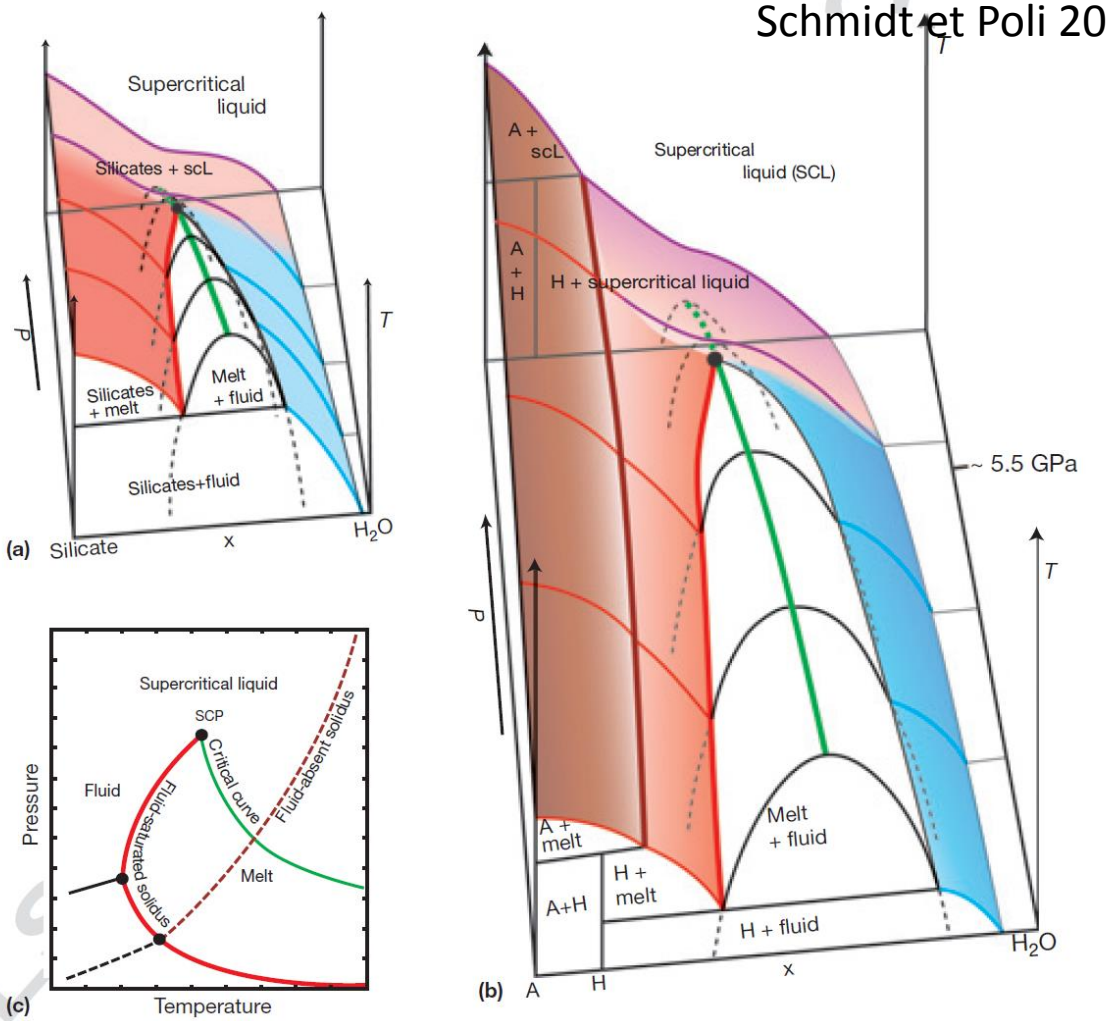

Figure 9 Simplified phase relations at the endpoint of the solidus and the end of the aqueous fluid–hydrous melt dichotomy, where continuum properties of a supercritical liquid exist. (a) With no hydrous phases stable above the solidus (as applicable for MORB at >3 GPa). (b) With hydrous phases (H) stable above the solidus (as applicable for pelites where the hydrous phase is phengite). A, anhydrous silicate. As is characteristic of supercritical liquids, a boundary between a noncritical and a supercritical fluid or melt or liquid cannot be drawn. (c) *P–T* diagram showing the wet solidus (red line), the critical curve (green line) that corresponds to the crest of the fluid–melt immiscibility gap, and the fluid-absent solidus for a hydrous phase (brown line). At low pressures, a broad miscibility gap exists between a hydrous fluid and an H_2O-bearing melt. With increasing pressure reciprocal solubilities increase, until the immiscibility gap becomes metastable at the wet solidus. At this point, a continuum between fluid-like and melt-like properties and compositions emerge for all pressures above the soldus' endpoint. The T–x section on the backside of panels (a) and (b) gives the continuum curve for pressures above the critical endpoint of the solidus. Fluid-absent melting is not affected by the endpoint, and the peritectic reaction $H = A +$ melt is stable at all pressures of (b) and (c). Note that the influence of CO_2 on the critical endpoint of the solidus of natural rock compositions is unknown, but the few available experiments seem to indicate that, in the CO_2-only system, carbonatite melts form between 3–5 and 23 GPa.

Kessel 2005

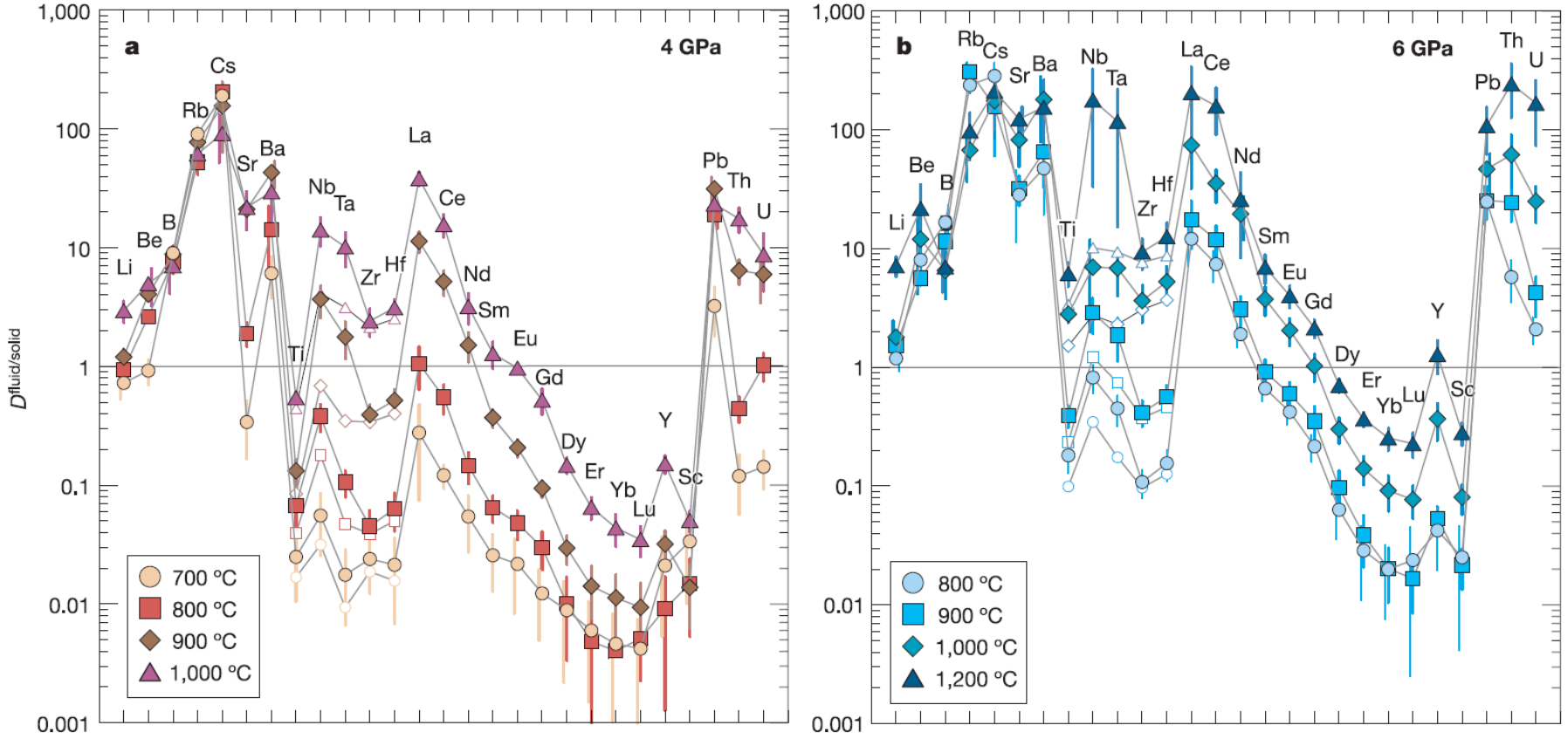

Figure 1 | Experimental fluid–solid partition coefficients for average MORB. **a**, Aqueous fluids (700–900 °C) and hydrous melt (1,000 °C) at 4 GPa; **b**, supercritical liquid (800–1,200 °C) at 6 GPa. The solid residue is calculated from the element concentrations in the solids multiplied by their abundance in the residue. Filled symbols refer to a garnet-clinopyroxene residue, open symbols to a garnet-clinopyroxene-rutile residue (see also Supplementary Information). Uncertainties are given as 1σ and were calculated by propagating uncertainties of elemental concentrations. 1σ error bars are sometimes shifted off the symbol centre for clarity.

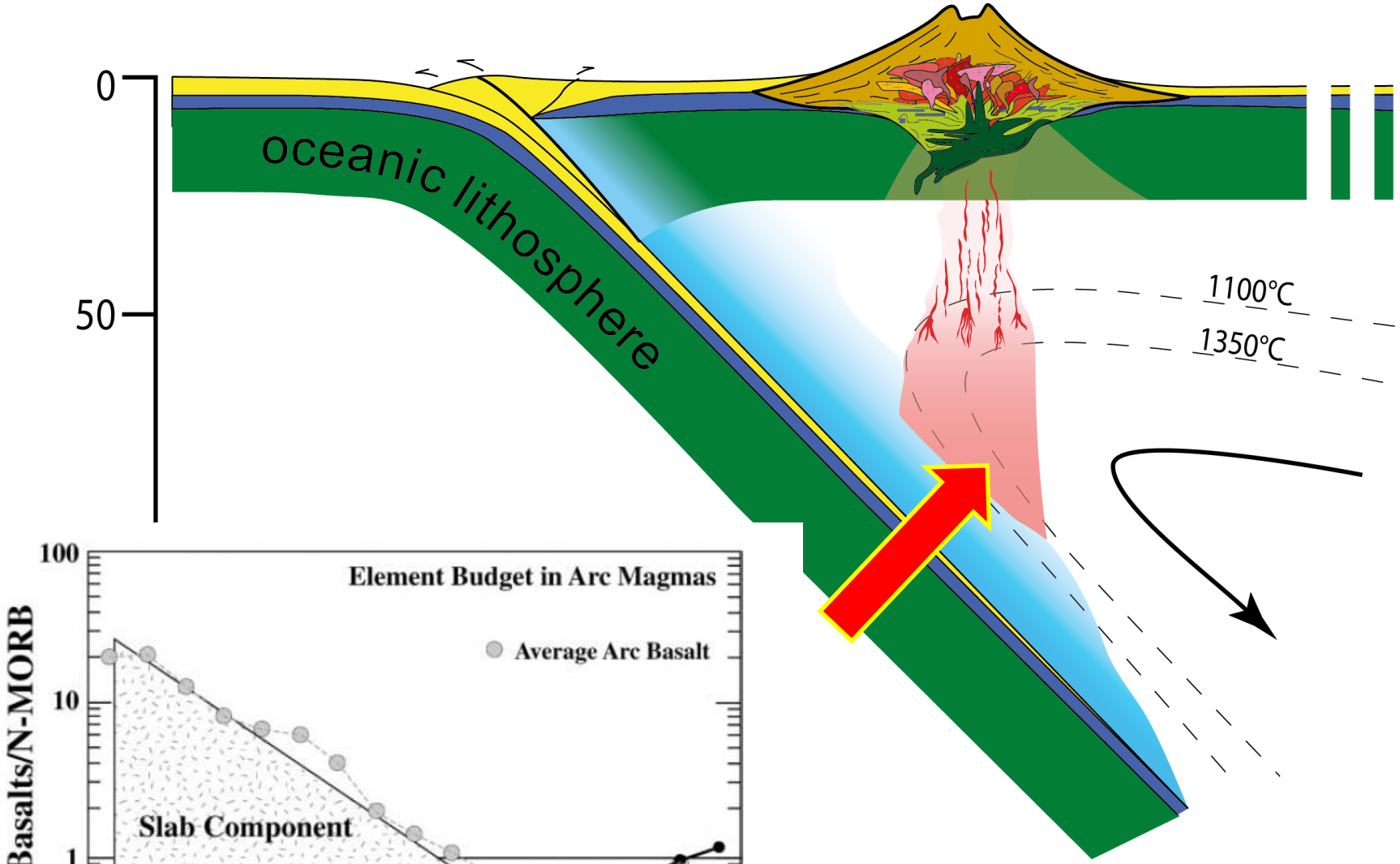

Ulmer 2001

Fig. 1. Schematic 'spidergram' modified after McCulloch and Gamble (1991). The relative contributions for slab and asthenospheric components of 'arc' basalts are shown schematically. The grey dots represent the MORB-normalized trace element abundances of average arc basalts.

2) Petrogenese des liquides primaires

Effet de l'H2O

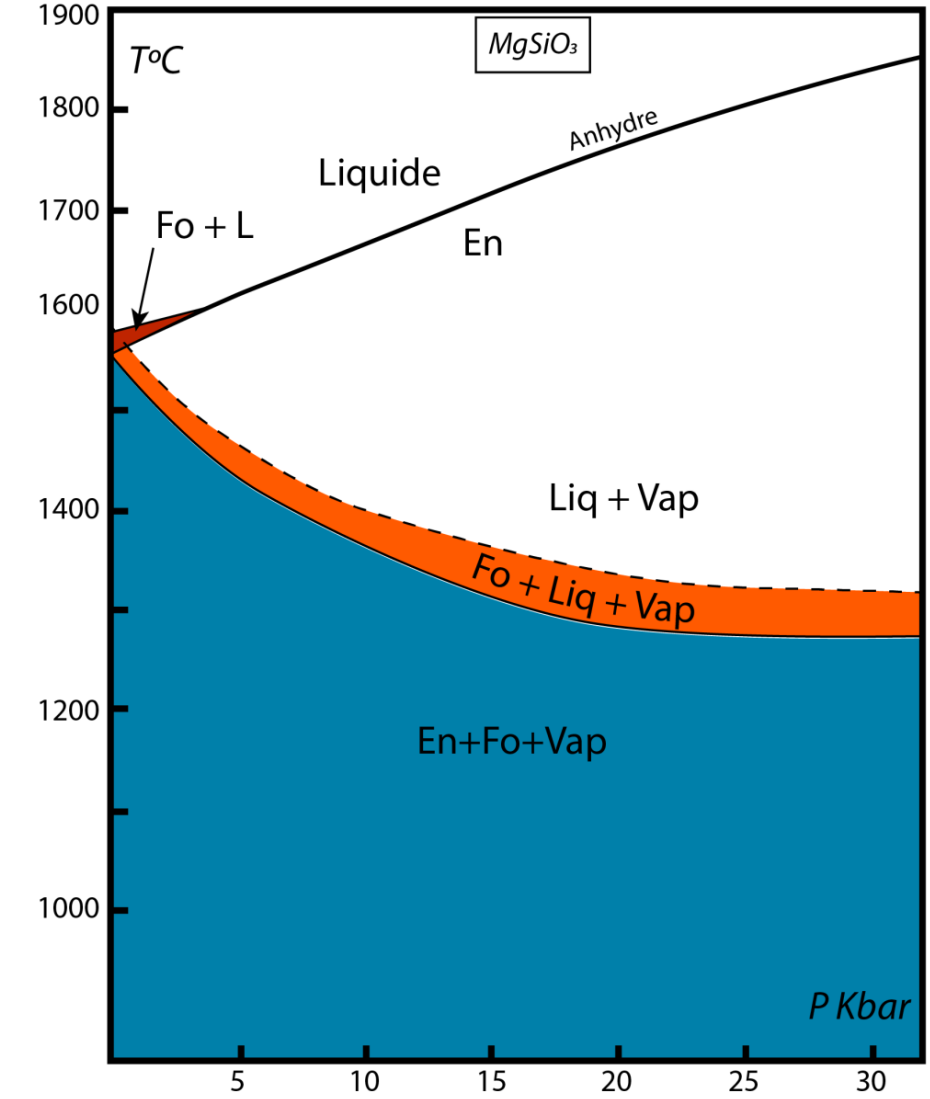

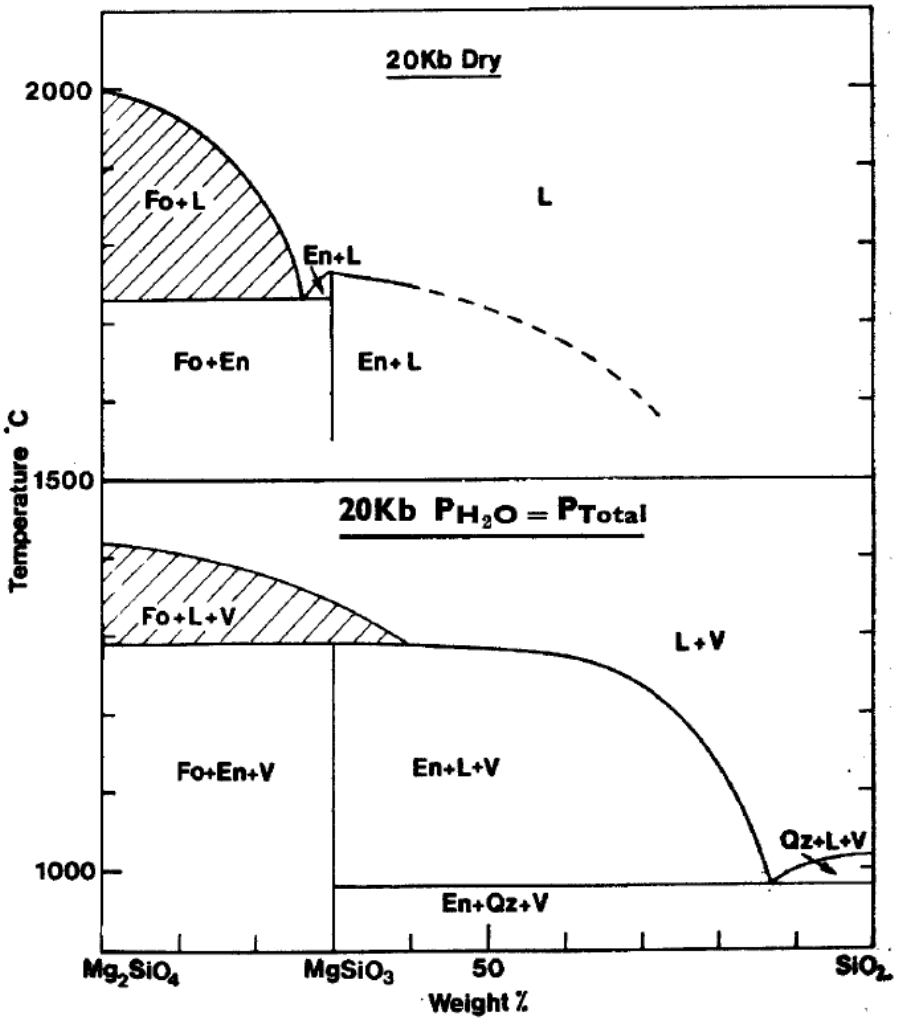

Kushiro et al. 1968

Effet de l'H2O

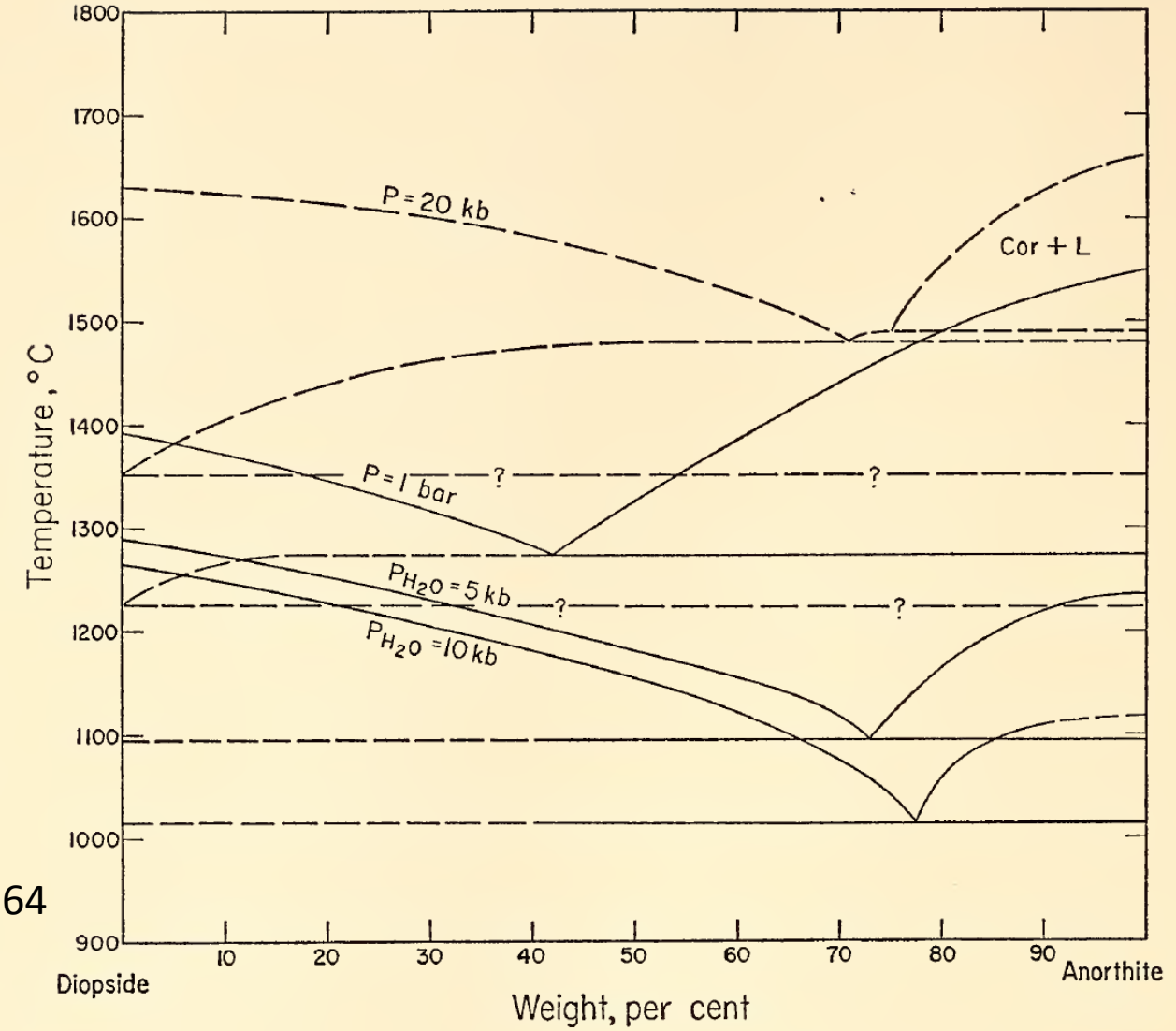

Yoder Year book 64

Fig. 11. Compilation of the projections of diopside-anorthite-water system at 20 kb, deduced mainly from Clark, Schairer, and de Neufville in *Year Book 61* (p. 67); at 1 bar, modified from Osborn (1942) in the light of Clark, Schairer, and de Neufville (*ibid.*, p. 66); at $P_{H_2O} = 5$ kb and $P_{H_2O} = 10$ kb from present studies. Completely crystalline assemblage probably includes a form of SiO_2 as well as diopside solid solution and anorthite at all pressures illustrated. Cor, corundum.

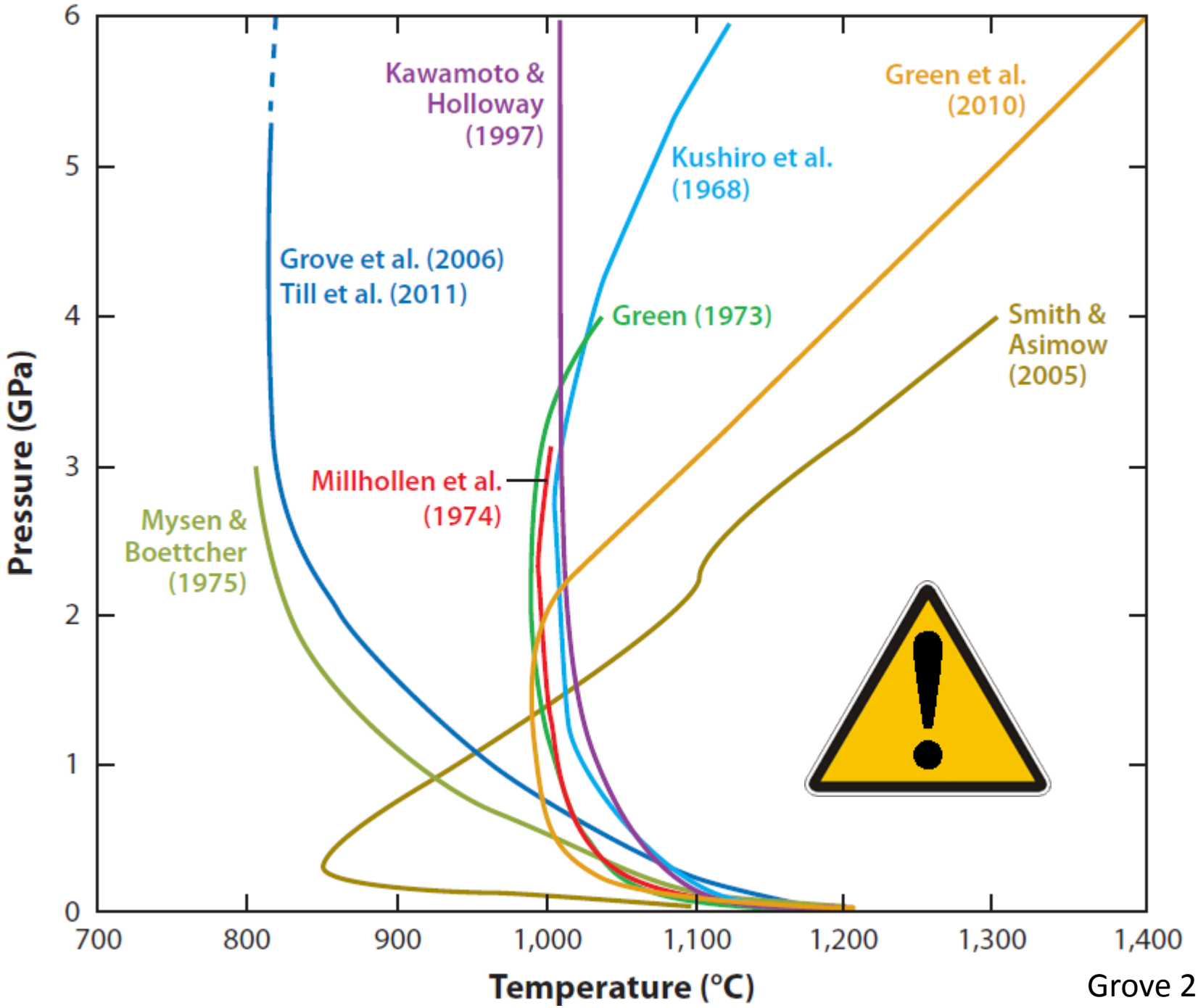
Pressure (GPa)
6
5
4
3
2
1
0
700
800
900
1,000
1,100
1,200
1,300
1,400
Temperature (°C)
Kawamoto & Holloway (1997)
Kushiro et al. (1968)
Green et al. (2010)
Grove et al. (2006)
Till et al. (2011)
Green (1973)
Smith & Asimow (2005)
Millhollen et al. (1974)
Mysen & Boettcher (1975)

Grove 2012

H2O (Sur)saturé VS sous saturé

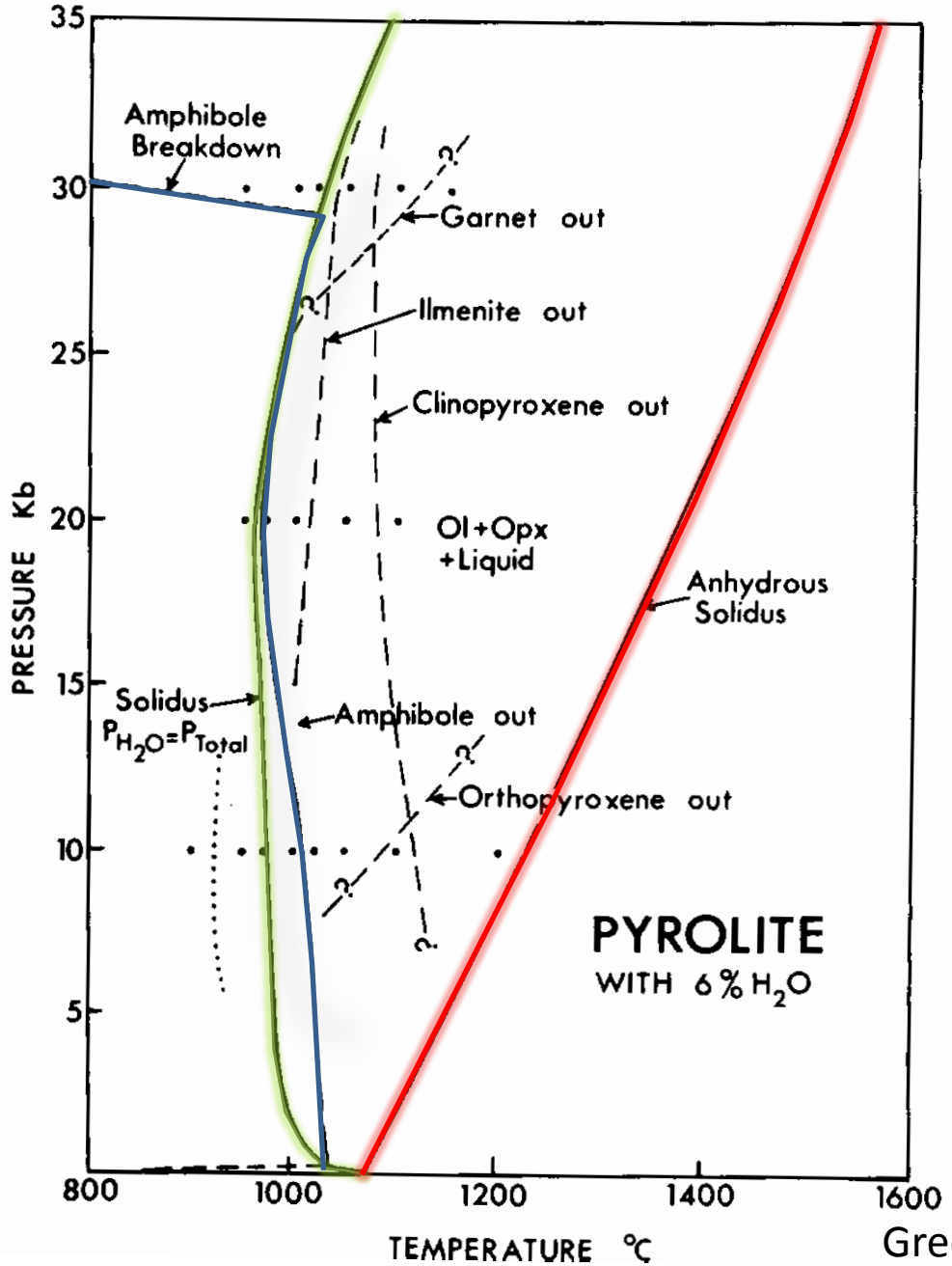

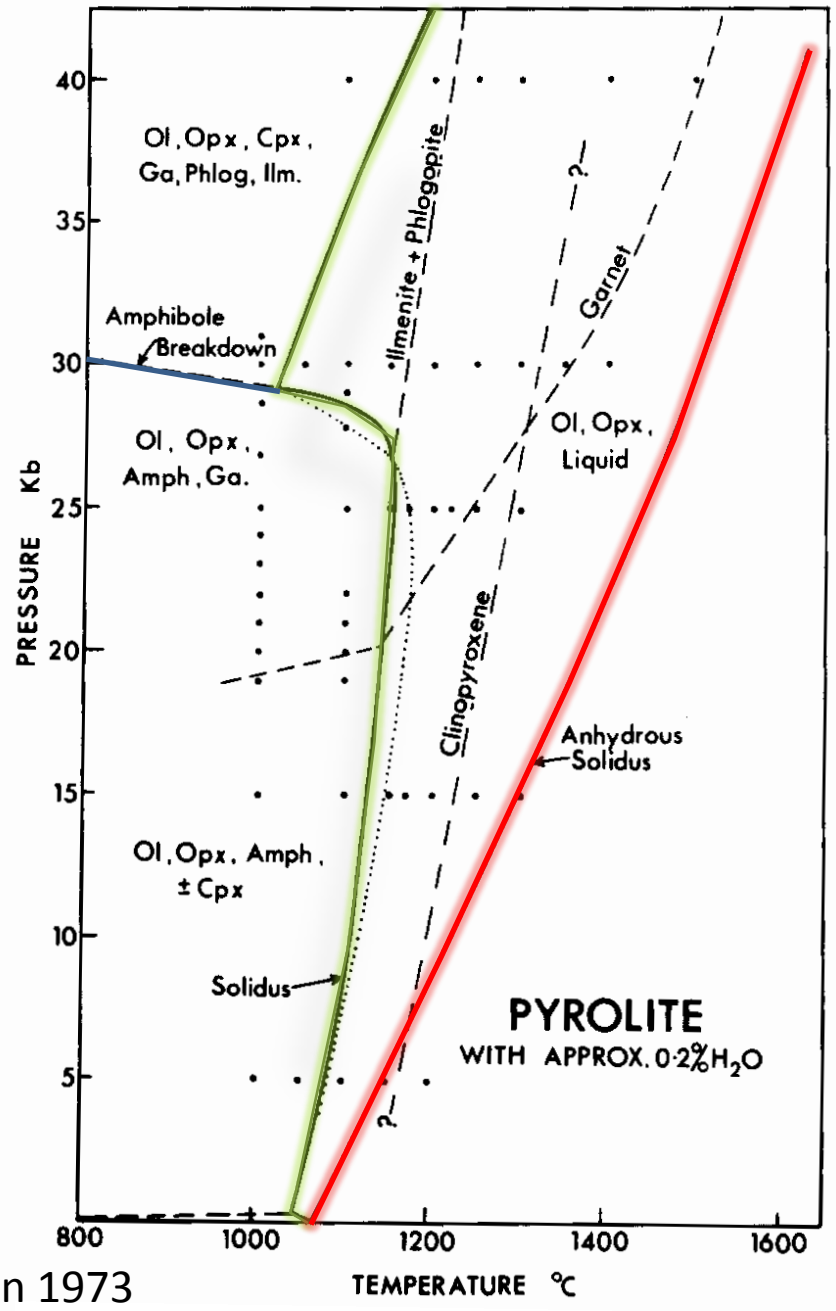

Green 1973

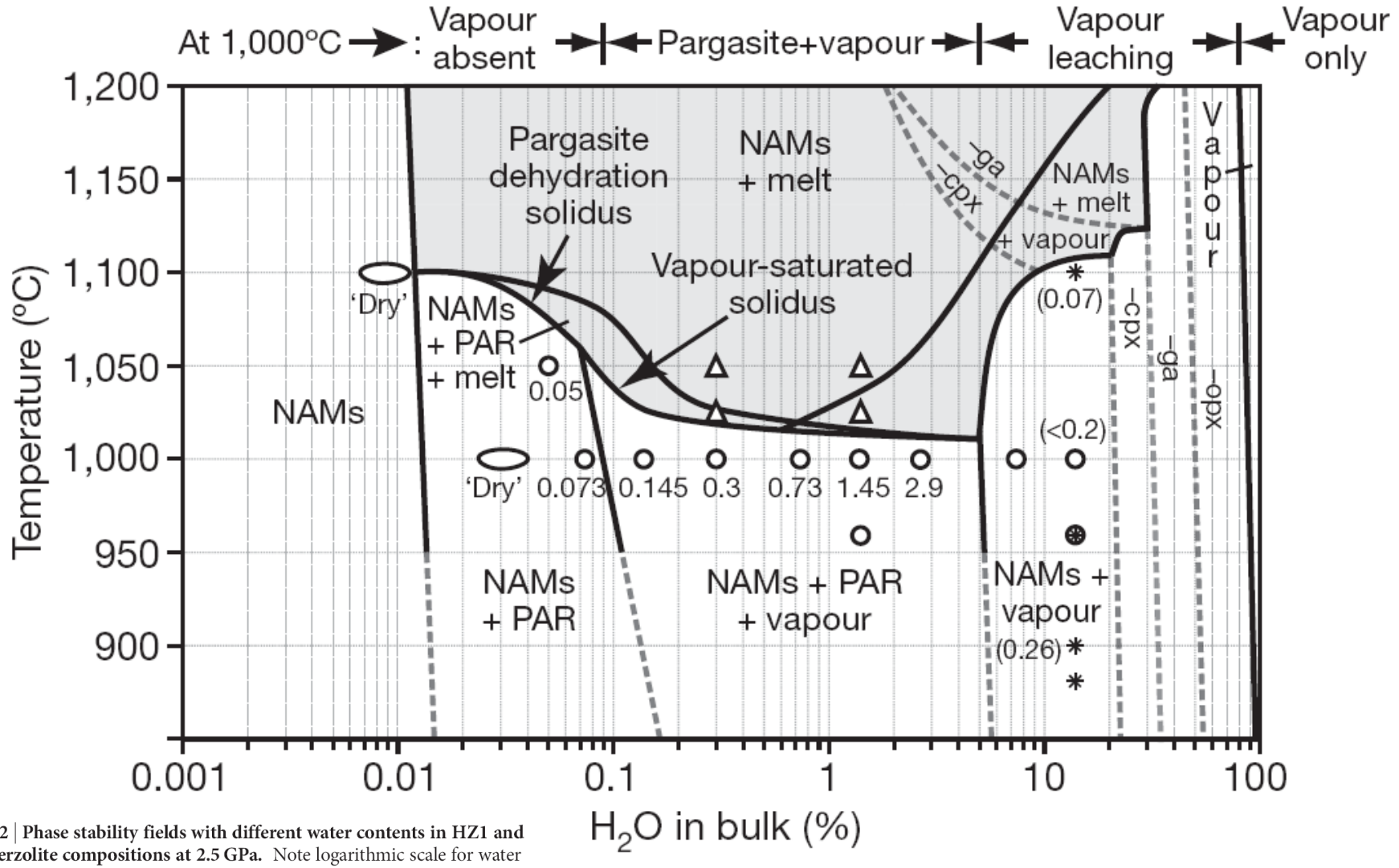

Figure 2 | Phase stability fields with different water contents in HZ1 and HZ2 lherzolite compositions at 2.5 GPa. Note logarithmic scale for water content. Referring to the sequence of experiments at 2.5 GPa, 1,000 °C, vapour is absent at less than 0.1 wt% H_2O (water is held in NAMs or NAMs+pargasite) and pargasite is unstable at more than 5 wt% H_2O, owing to dissolution of Na_2O and K_2O (essential for pargasite stability) in the increasingly water-rich vapour phase. At high water/rock ratios (more than 5 wt% H_2O), lherzolite HZ1 is composed of refractory NAMs and is leached of low-melting components by the vapour phase. It does not experience melting at low temperatures and may be leached by very large water/rock ratios to residual dunite + vapour[18,28]. Open circle and open ellipse, subsolidus; open triangle, hydrous silicate melt present; asterisk, experiments at 2.4 GPa from ref. 15; light grey shaded area, presence of melt. PAR, pargasite; ga, garnet; cpx, clinopyroxene; opx, orthopyroxene.

Green 2010

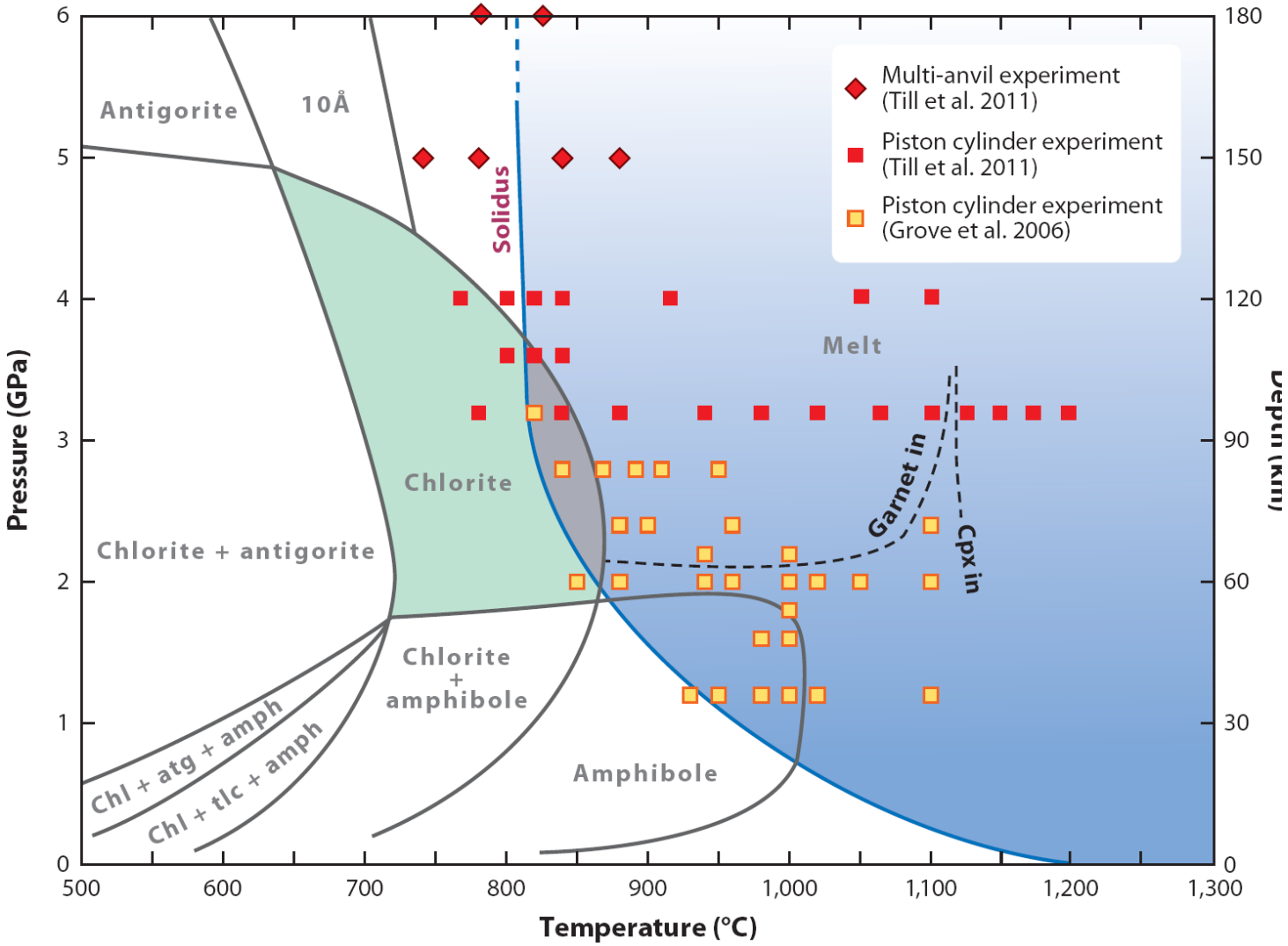

Figure 4

Experimentally determined phase diagram for H_2O-saturated peridotite from Grove et al. (2006) and Till et al. (2011). Experiments were conducted with the primitive mantle composition of Hart & Zindler (1986) Hydrous and aluminous phase stabilities that are not constrained by the experiments conducted by Grove et al. (2006) and Till et al. (2011) are derived from Ulmer & Trommsdorff (1995), Fumagalli & Poli (2005) and Pawley (2003). Abbreviations: amph, amphibole; atg, antigorite; Chl, chlorite; Cpx, clinopyroxene; tlc, talc.

Grove 2012

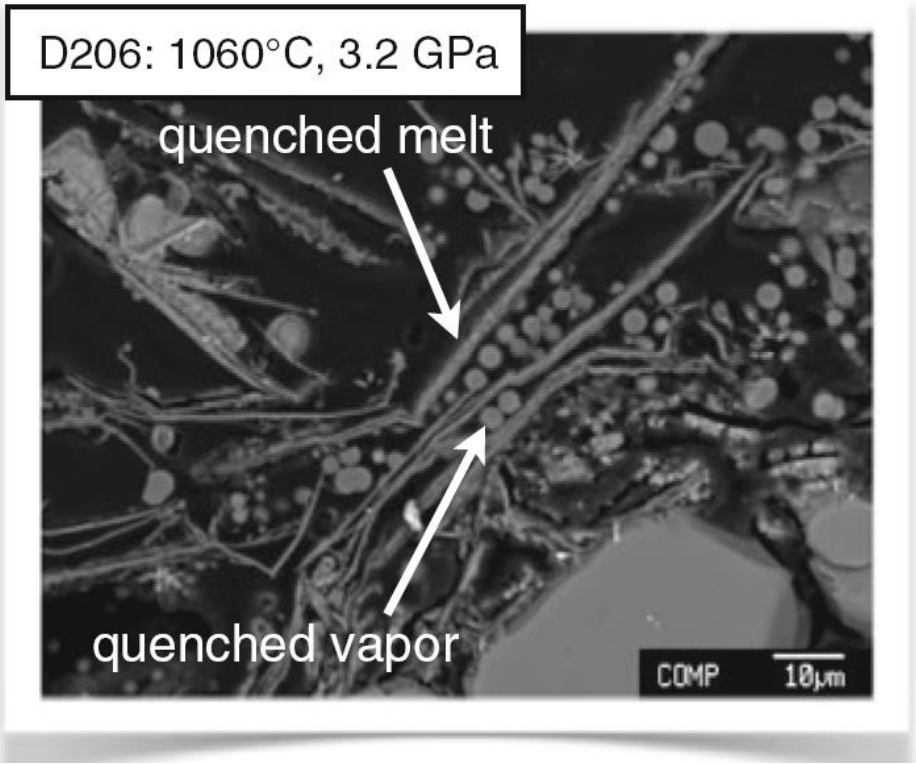
D206: 1060°C, 3.2 GPa
quenched melt
quenched vapor
COMP
10µm

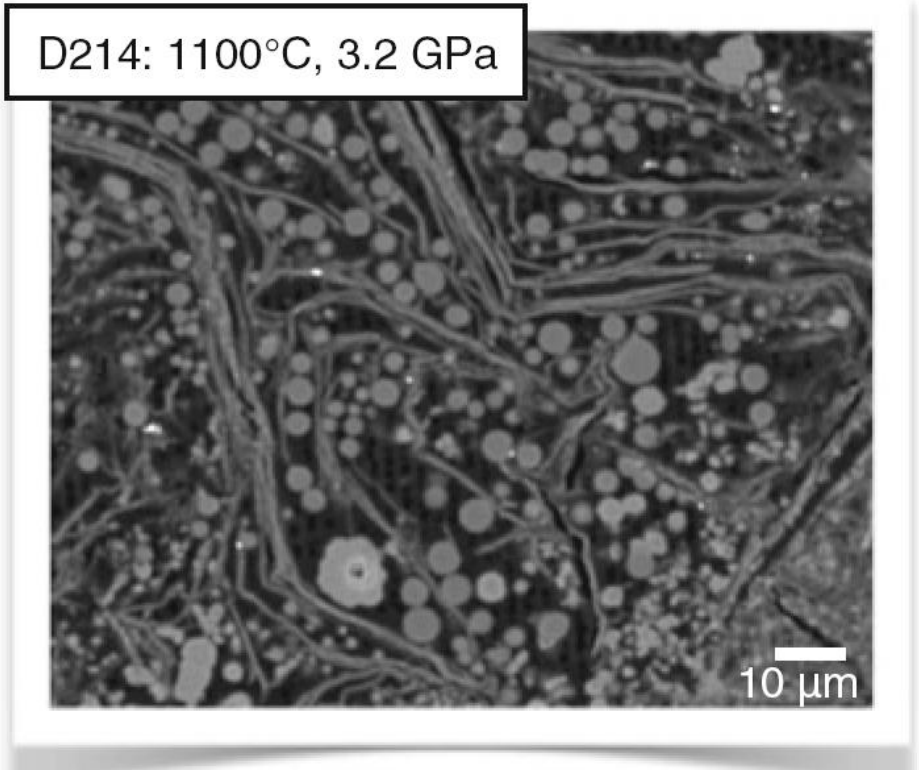
D214: 1100°C, 3.2 GPa
10 µm

Till 2012

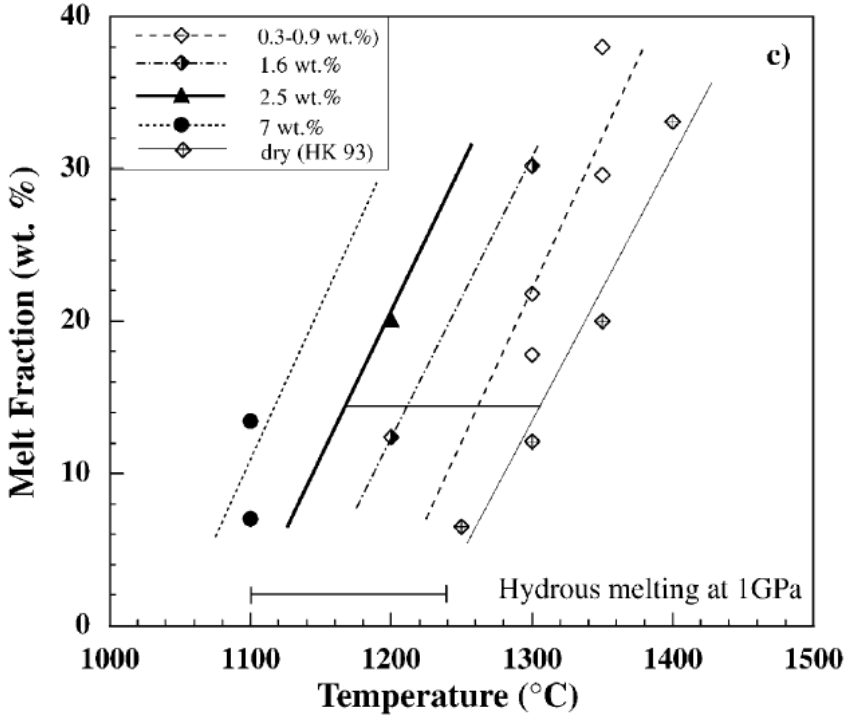
0.3-0.9 wt.%)
1.6 wt.%
2.5 wt.%
7 wt.%
dry (HK 93)
c)
Hydrous melting at 1GPa
Melt Fraction (wt. %)
Temperature (°C)
0
10
20
30
40
1000
1100
1200
1300
1400
1500

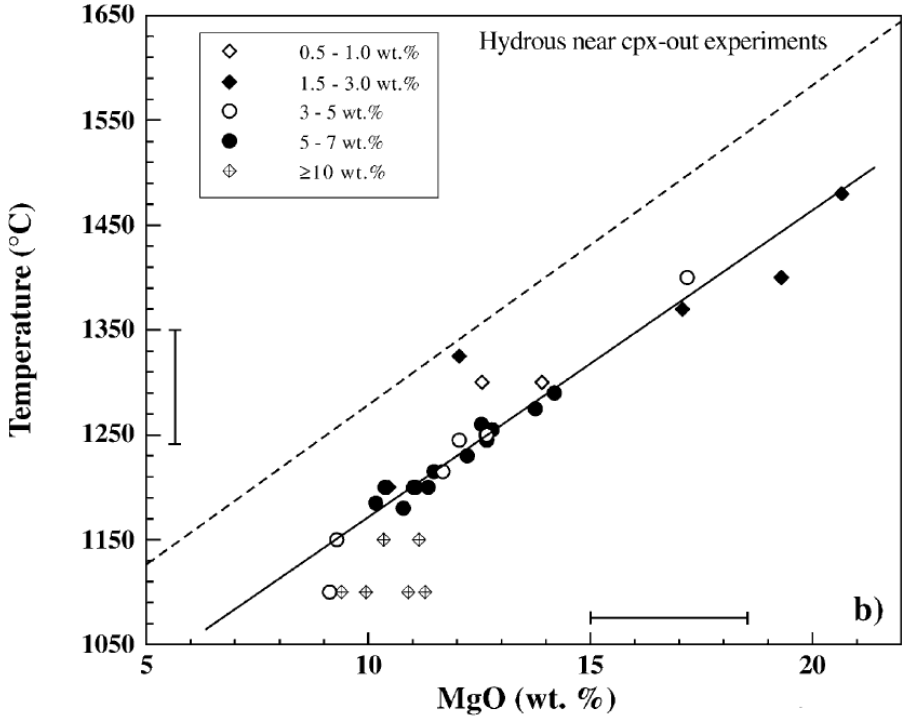
0.5 - 1.0 wt.%
1.5 - 3.0 wt.%
3 - 5 wt.%
5 - 7 wt.%
≥10 wt.%
Hydrous near cpx-out experiments
b)
Temperature (°C)
MgO (wt. %)
1050
1150
1250
1350
1450
1550
1650
5
10
15
20

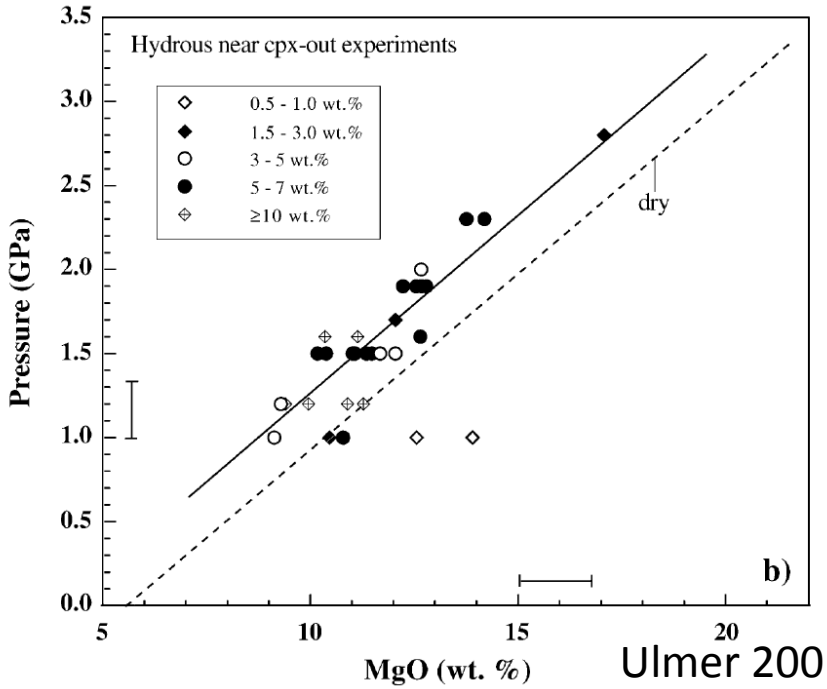
Hydrous near cpx-out experiments
0.5 - 1.0 wt.%
1.5 - 3.0 wt.%
3 - 5 wt.%
5 - 7 wt.%
≥10 wt.%
dry
b)
Pressure (GPa)
MgO (wt. %)
0.0
0.5
1.0
1.5
2.0
2.5
3.0
3.5
5
10
15
20

Ulmer 2001

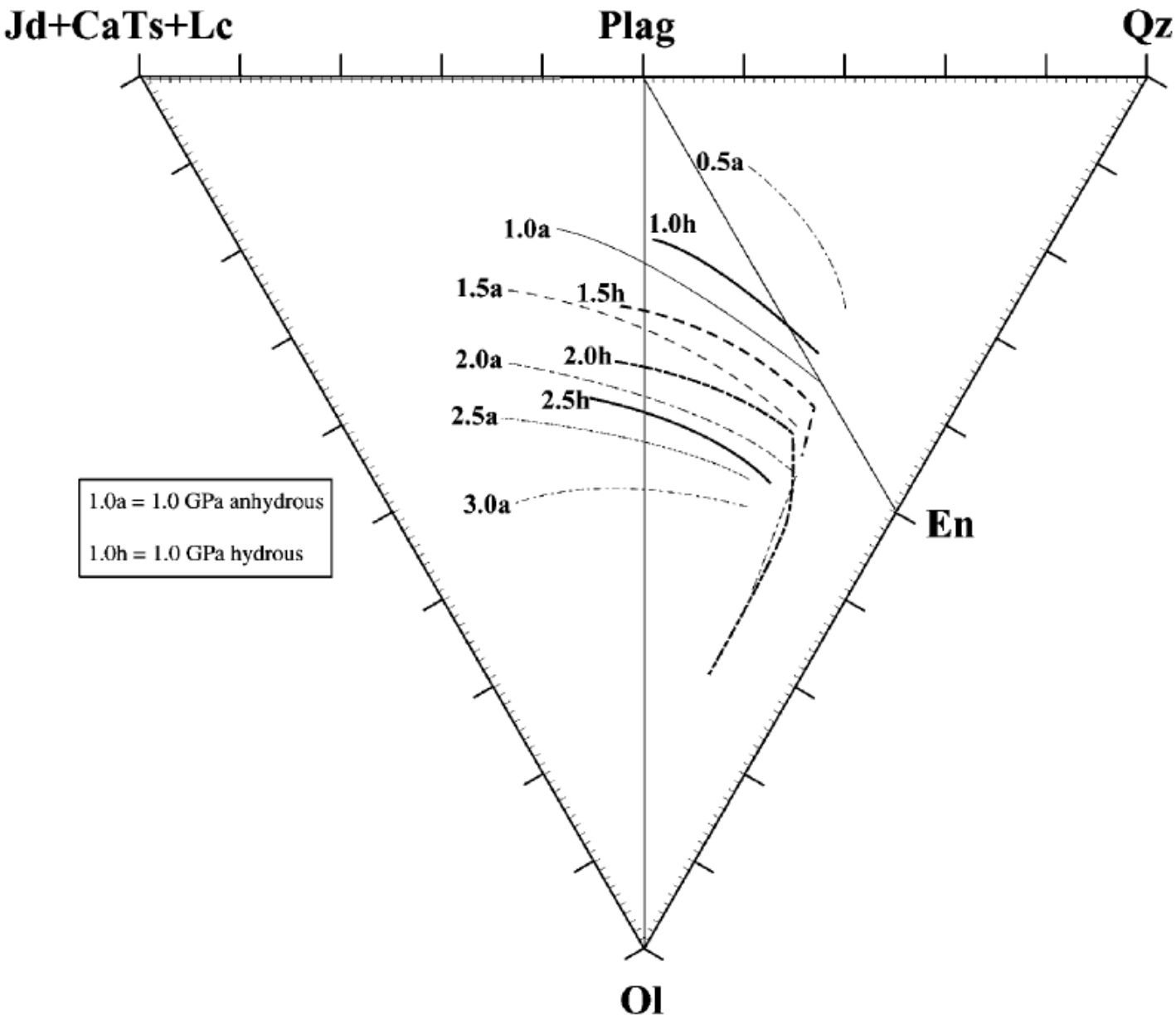
Jd+CaTs+Lc
Plag
Qz
0.5a
1.0a
1.0h
1.5a
1.5h
2.0a
2.0h
2.5h
2.5a
3.0a
1.0a = 1.0 GPa anhydrous
1.0h = 1.0 GPa hydrous
En
Ol

(c)

Primitive arc magma

	continental						intra-oceanic			continental		
	Cascades			Mexico		C.A.	Vanuatu	Palau	Izu- Bonin	Mexico	Sunda	Mexico
	thol.	calc-alkaline						thol.	depl.thol.	low-Si	shoshonitic	
	basalt	basalt	andesite	basalt	andesite	basalt	basalt	basalt	andesite	basalt	basalt	shoshonite
n	52	34	38	20	96	6	26	16	46	25	9	37
SiO_2	48.6	50.6	53.3	50.7	55.1	51.1	49.2	50.9	57.1	45.8	46.5	51.3
TiO_2	0.71	1.3	0.96	1.04	0.9	1.21	0.69	0.57	0.18	1.49	0.92	1.57
AL_2O_3	17.7	16.3	16.5	16	15.8	16.1	12.9	16.2	12.1	14.1	12.3	13.3
FeO_{tot}	8.55	8.25	7.29	7.98	6.66	8.39	9.69	8.03	8.34	10.37	8.62	7.27
MNO	0.16	0.14	0.13	0.14	0.12	0.15	0.2	0.16	0.16	0.18	0.16	0.13
MGO	10.03	9.09	8.62	9.51	8.28	8.68	12.93	10.93	11.62	13.47	11.35	9.56
CAO	11.54	9.35	8.57	9.1	7.59	9.63	11.21	10.52	8.41	10.53	12.21	8.03
NA_2O	2.45	3.29	3.35	3.55	3.81	2.76	1.99	2.38	1.69	2.61	2.14	3.14
K_2O	0.16	1.21	1.02	1.49	1.4	1.59	0.97	0.26	0.43	0.93	4.9	4.51
P_2O_5	0.08	0.42	0.28	0.44	0.28	0.47	0.2	0.06	0.04	0.46	0.89	1.23
X_{Mg}	0.677	0.663	0.678	0.68	0.689	0.649	0.704	0.708	0.713	0.698	0.701	0.701
V	211	196	178	194	150	218	294	263	203	264	267	204
Cr	279	328	385	452	378	335	687	658	781	853	622	412
Ni	194	190	182	210	205	164	246	197	196	348	176	279

Basaltes (ol norm) et Andesites (high XMg)

Compilation Schmidt & Jagoutz 2017

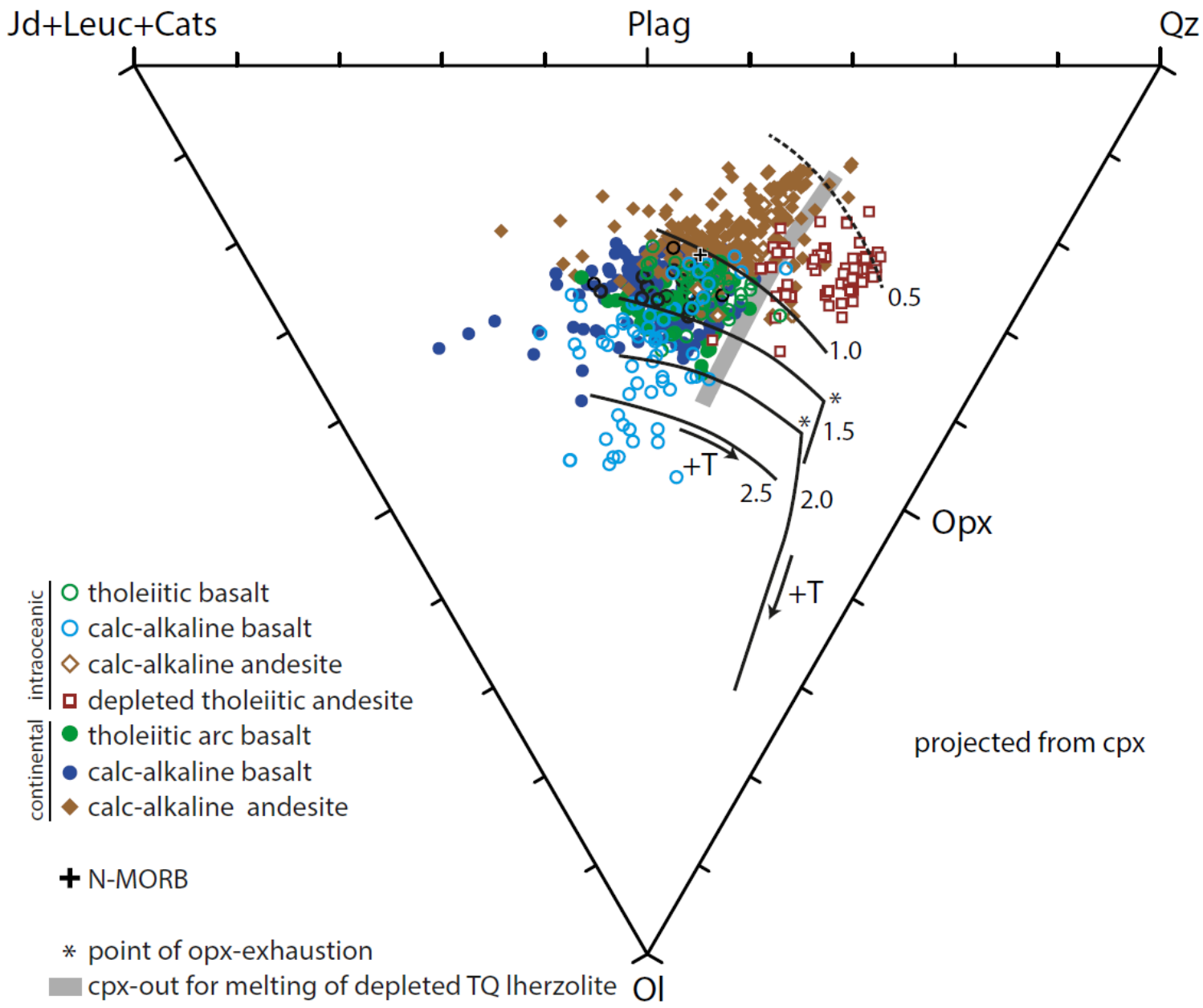

Compilation Schmidt & Jagoutz 2017

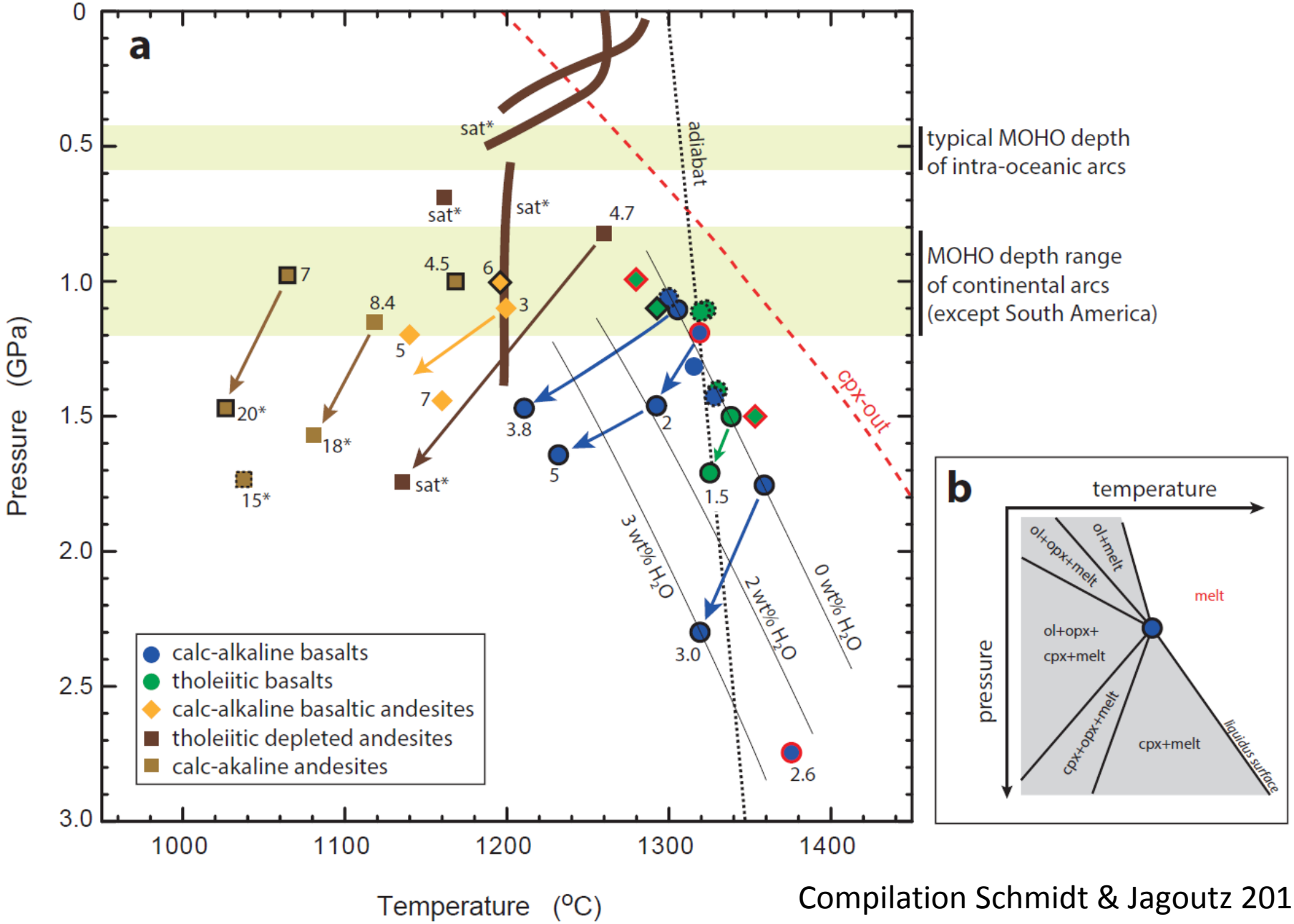

Compilation Schmidt & Jagoutz 2017

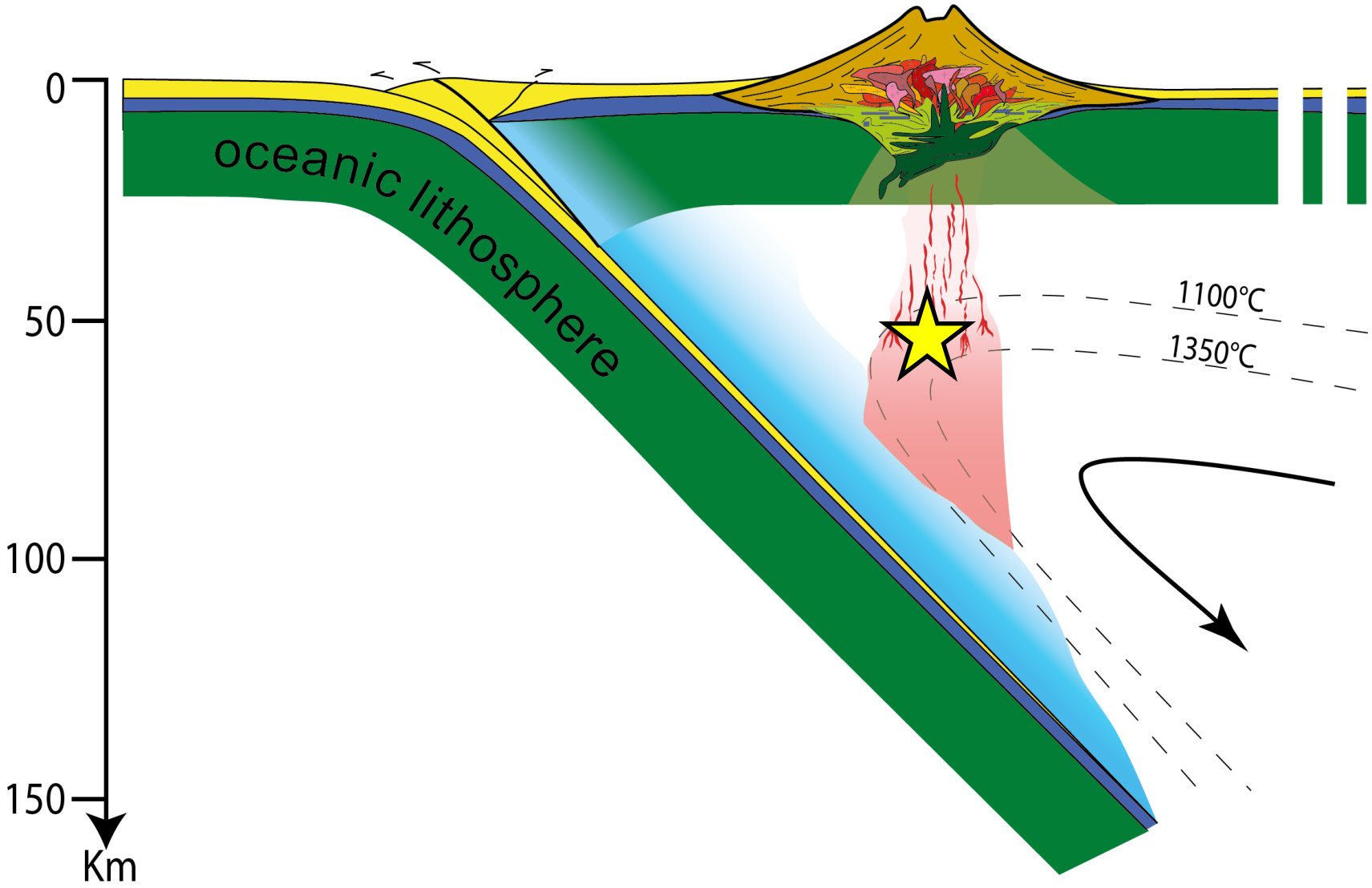

Deux types de Liquides Primaires peuvent être produit dans le Coin du Manteau (Mantle Wedge)

3) Evolution des liquides primaires

Evolution des magmas ?

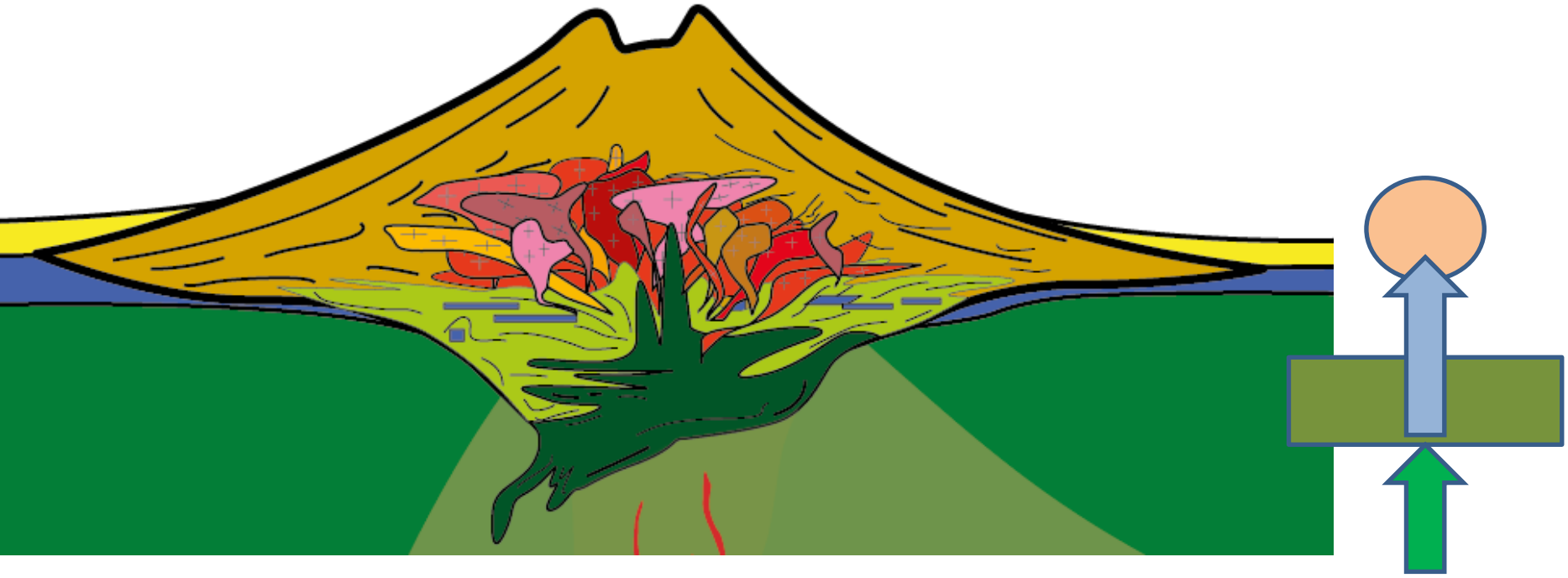

Exp. Petrology

Kohistan / Talkeetna / Urals …

Grove 2012

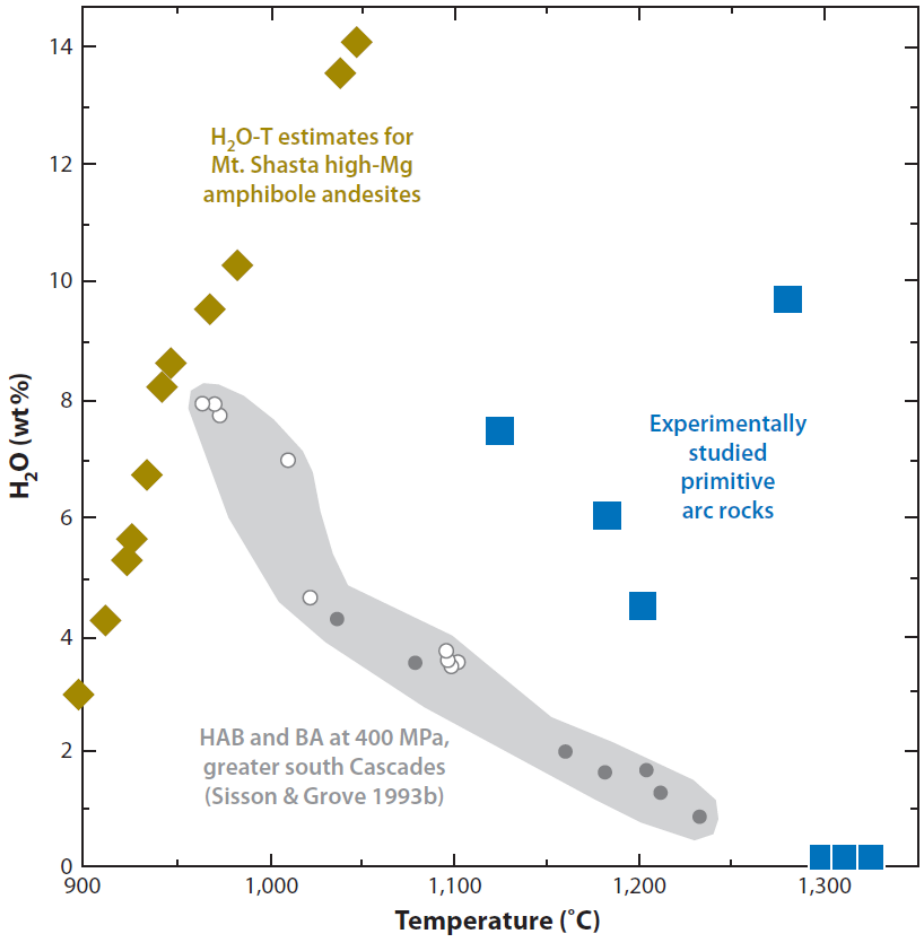

Figure 10

Temperature and H_2O contents of the near-primary arc magmas in their mantle source region from **Table 1** (*dark blue squares*) and pre-eruptive temperature and H_2O contents from mineral melt equilibria for crystallization in the continental crust and uppermost mantle. Porphyritic (*open circles*) and aphanitic lavas (*filled circles*) from the south Cascades region (Sisson & Grove 1993b) are shown in the gray field and highlight the range of H_2O contents in basaltic melts that crystallize at shallow crustal pressures. The dark yellow diamonds (Krawczynski et al. 2012) represent H_2O-saturated melts of andesite that crystallized in a magmatic crystal mush column below Mt. Shasta, California, that extends to mantle depths. A challenge is to understand the conditions that lead to the development of the high-H_2O–low-temperature melts near the mantle-crust transition below some arc volcanoes. Abbreviations: BA, basaltic andesite, HAB, high-alumina olivine tholeiite; wt%, weight percent.

Crystallization of Calc-Alkaline Andesite

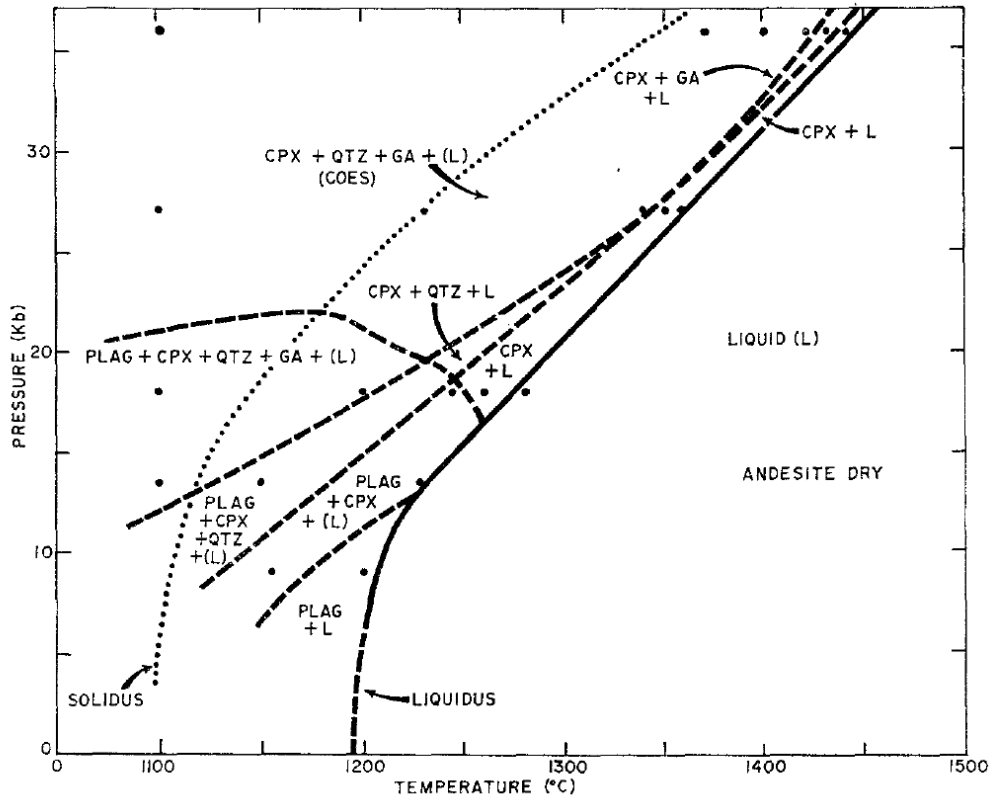

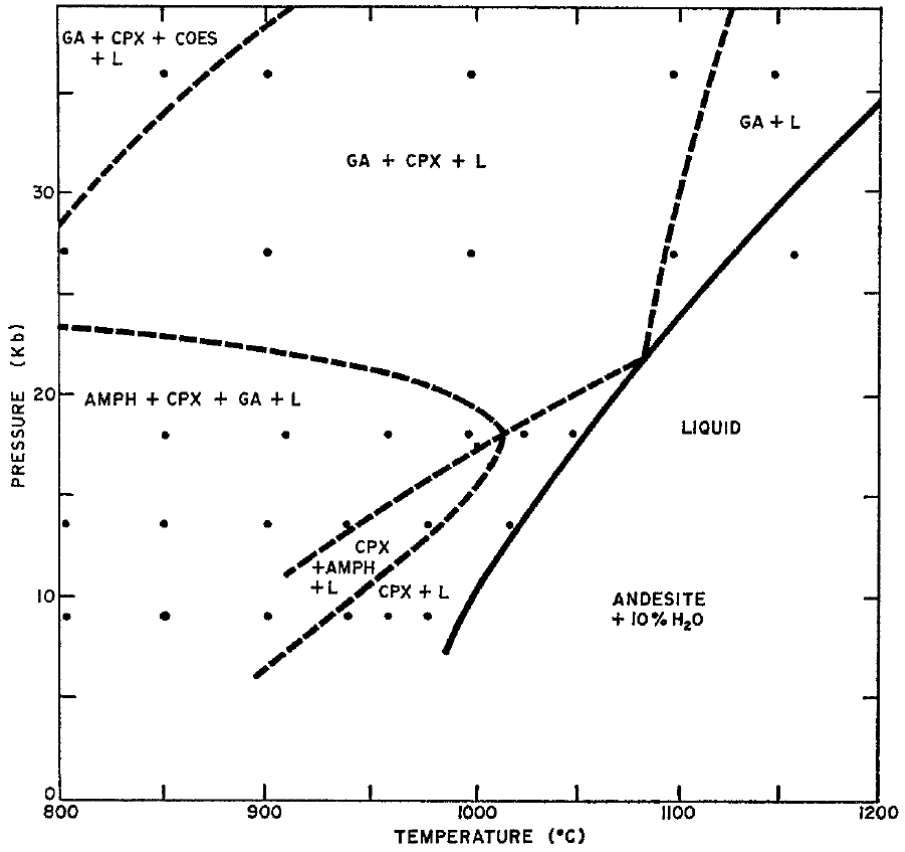

Liquidus repoussé / interval Liquidus-Solidus étendu
{ Plag ! / Grenat ! / Amph ! }

Green 1972

Melt density !

Gaetani-grove-2007

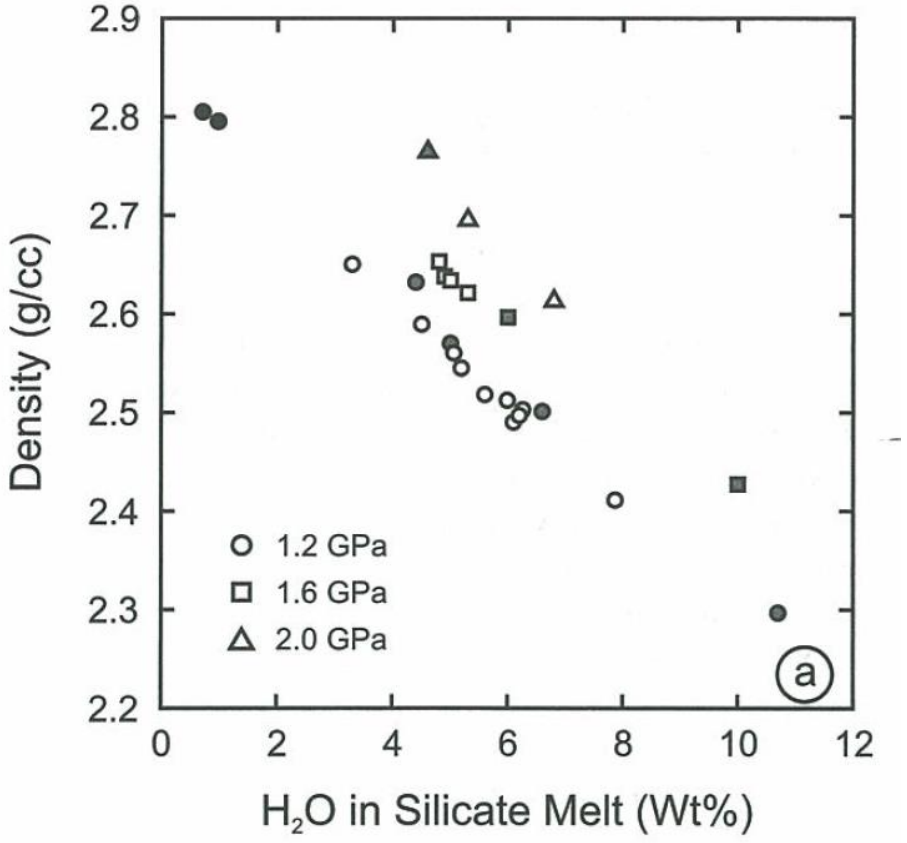

Figure 9. (a) Plot showing the relationship between the concentration of H_2O dissolved in a silicate melt and density of the melt, in g/cc, for nominally anhydrous (filled symbols) and H_2O-bearing (open and shaded symbols) melts saturated with a mantle peridotite mineral assemblage (Oliv + Opx ± Cpx ± Sp ± Gt) at 1.2 GPa (circles), 1.6 (squares), and 2.0 GPa (triangles) and temperatures of 1150 °C to 1350 °C calculated as discussed in the text. Open and filled symbols are data from Gaetani and Grove [1998]; shaded symbols are data from Kushiro [1990]. (b) Plot showing the relationship between temperature and melt density for experiments shown in (a). Arrow indicates the effect of increasing temperature on melt density.

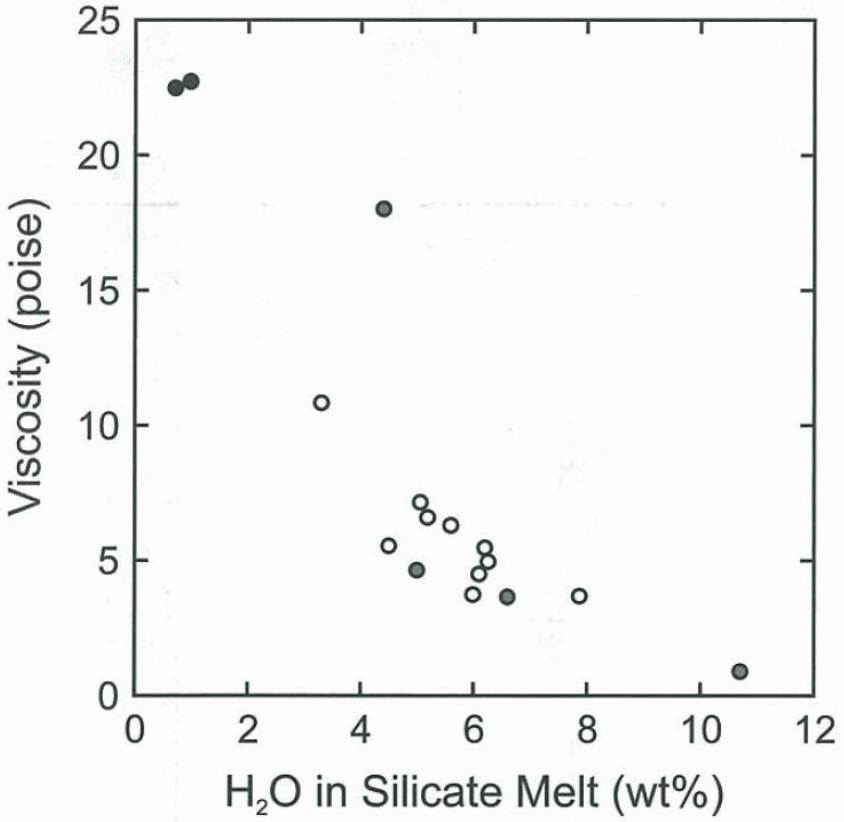

Figure 10. Plot showing the relationship between the concentration of H_2O dissolved in a silicate melt and viscosity of the melt, in poise, for nominally anhydrous (filled symbols) and H_2O-bearing (open and shaded symbols) melts saturated with a mantle peridotite mineral assemblage (Oliv + Opx ± Cpx ± Sp) at 1.2 GPa and temperatures of 1150 °C to 1350 °C calculated using the model of Shaw [1972]. Note that these calculations do not account explicitly for the effects of pressure on melt viscosity.

Hamilton 1964

Solubilité de l'eau

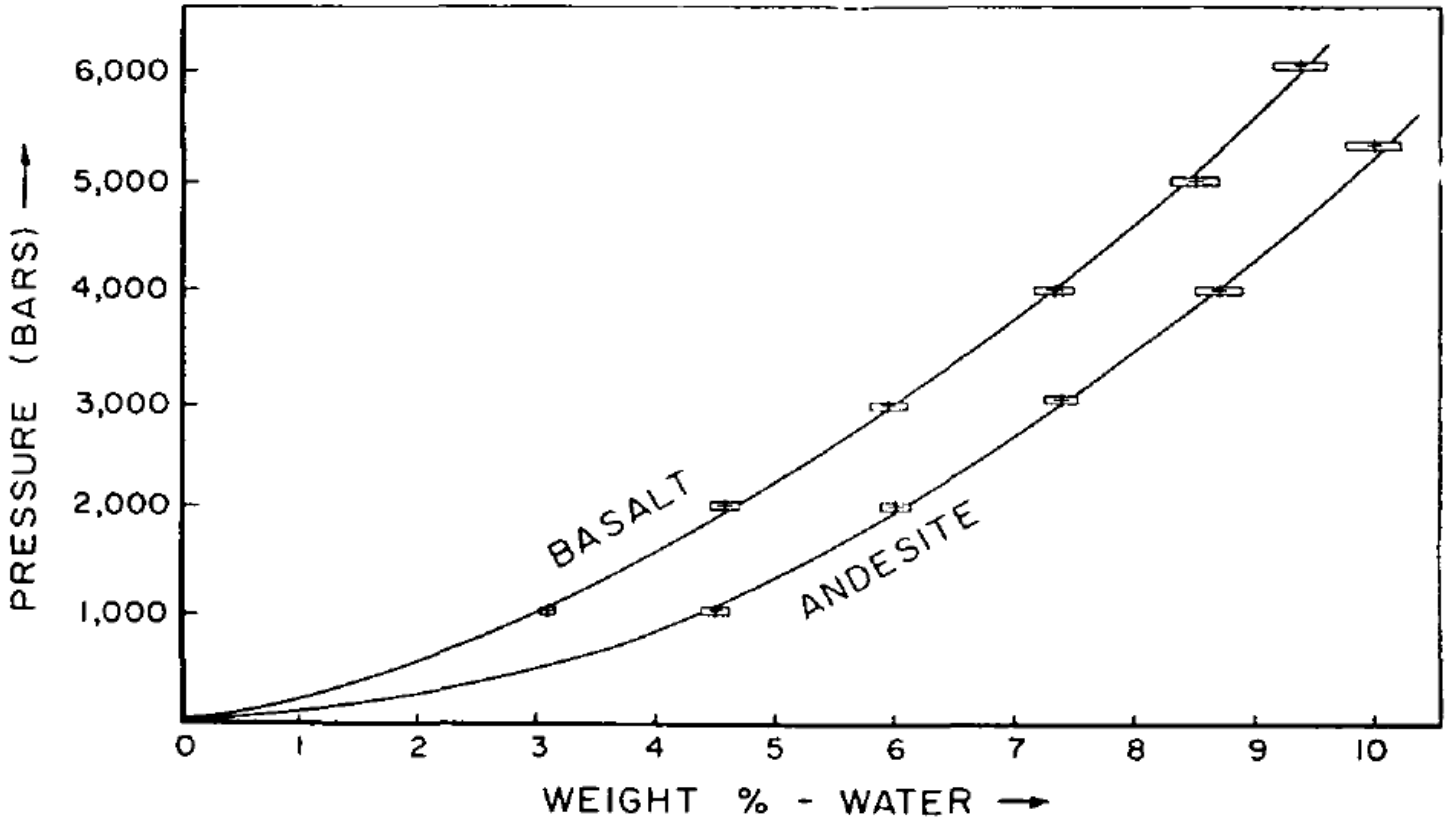

FIG. 1. The solubility of water (weight percent) in Columbia River basalt and Mount Hood andesite melts as a function of water pressure at 1,100° C. The lengths of the sides of the boxes are a measure of the estimated errors in pressure and solubility.

Evolution des magmas basaltiques

Muntener 2006

Picritic basalt

Villiger 2004

2.6 wt% H2O

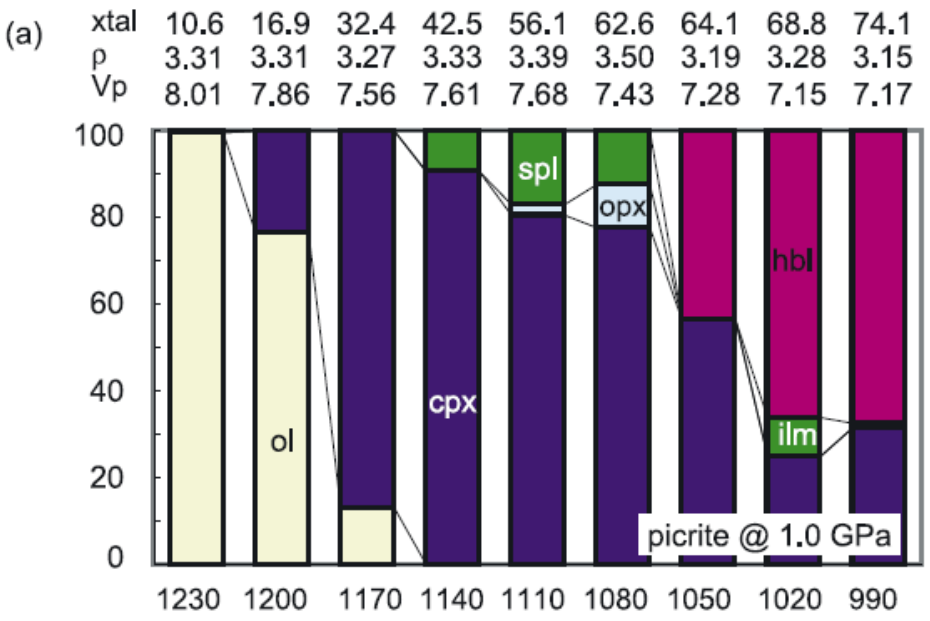

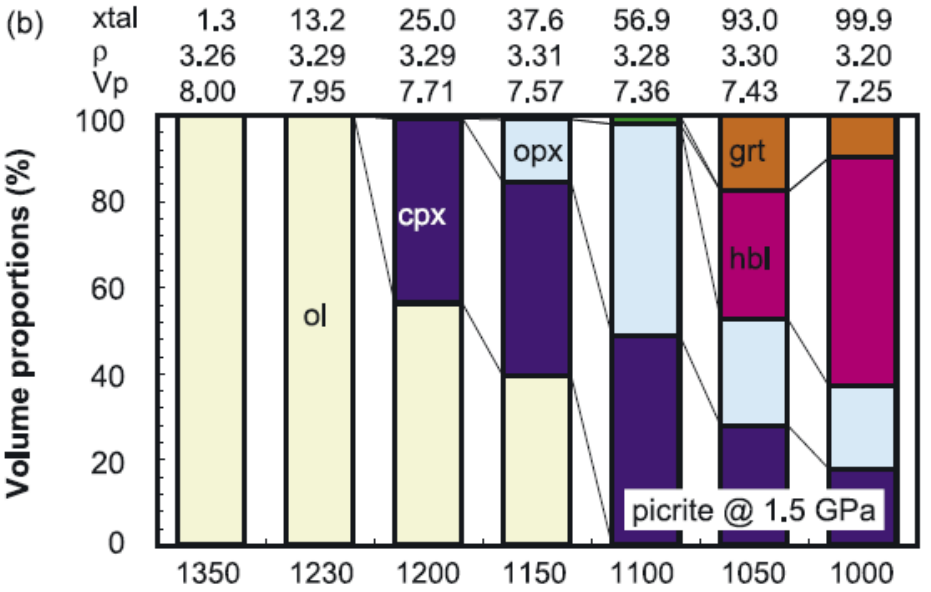

0,0 wt% H2O

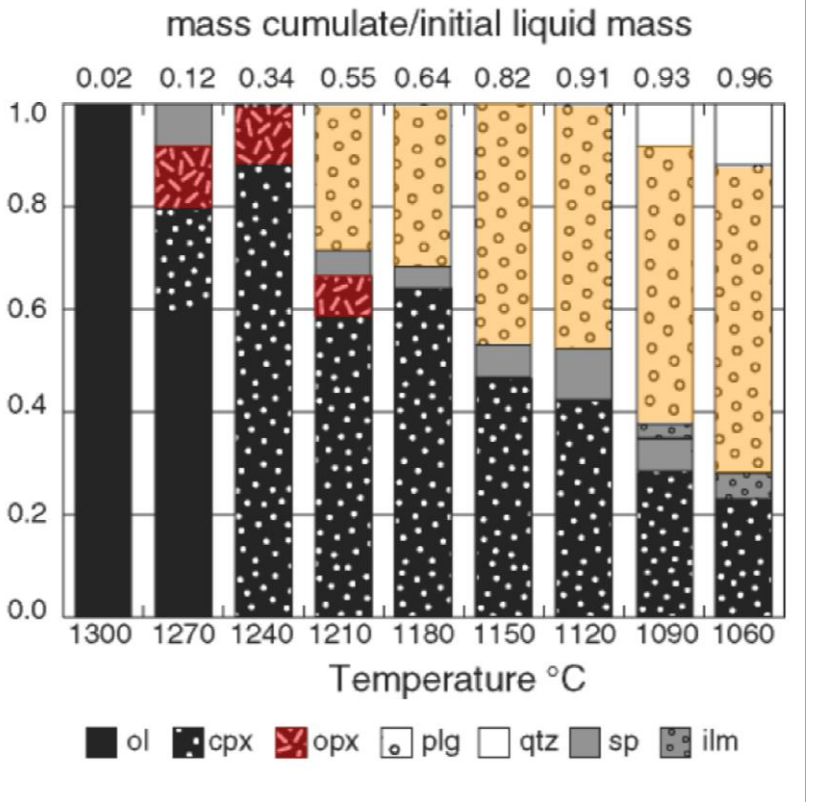

T solidus
Plag !
Hbl !
Grt !

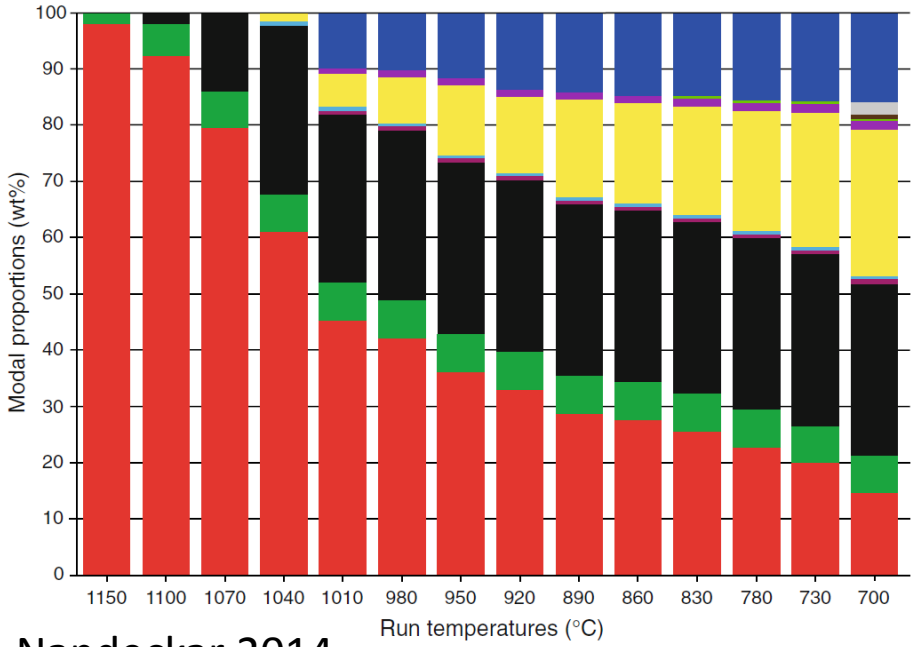

Grove 1982

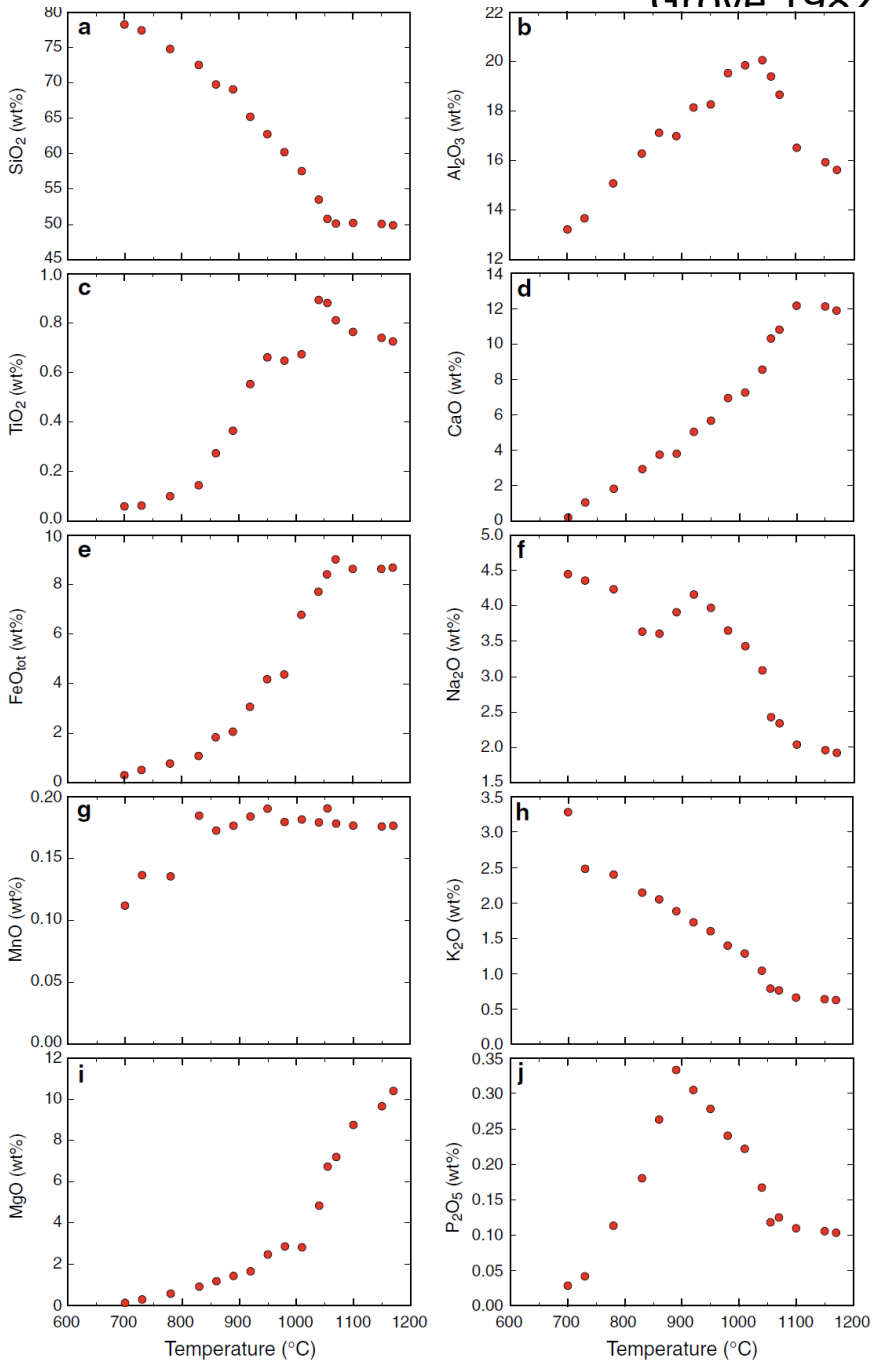

Nandeckar 2014

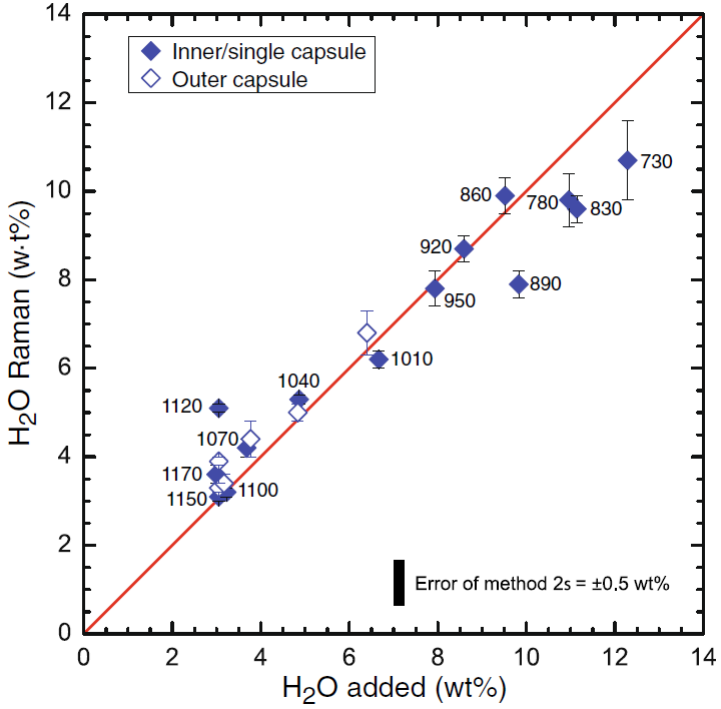

HAB

Foden 1992

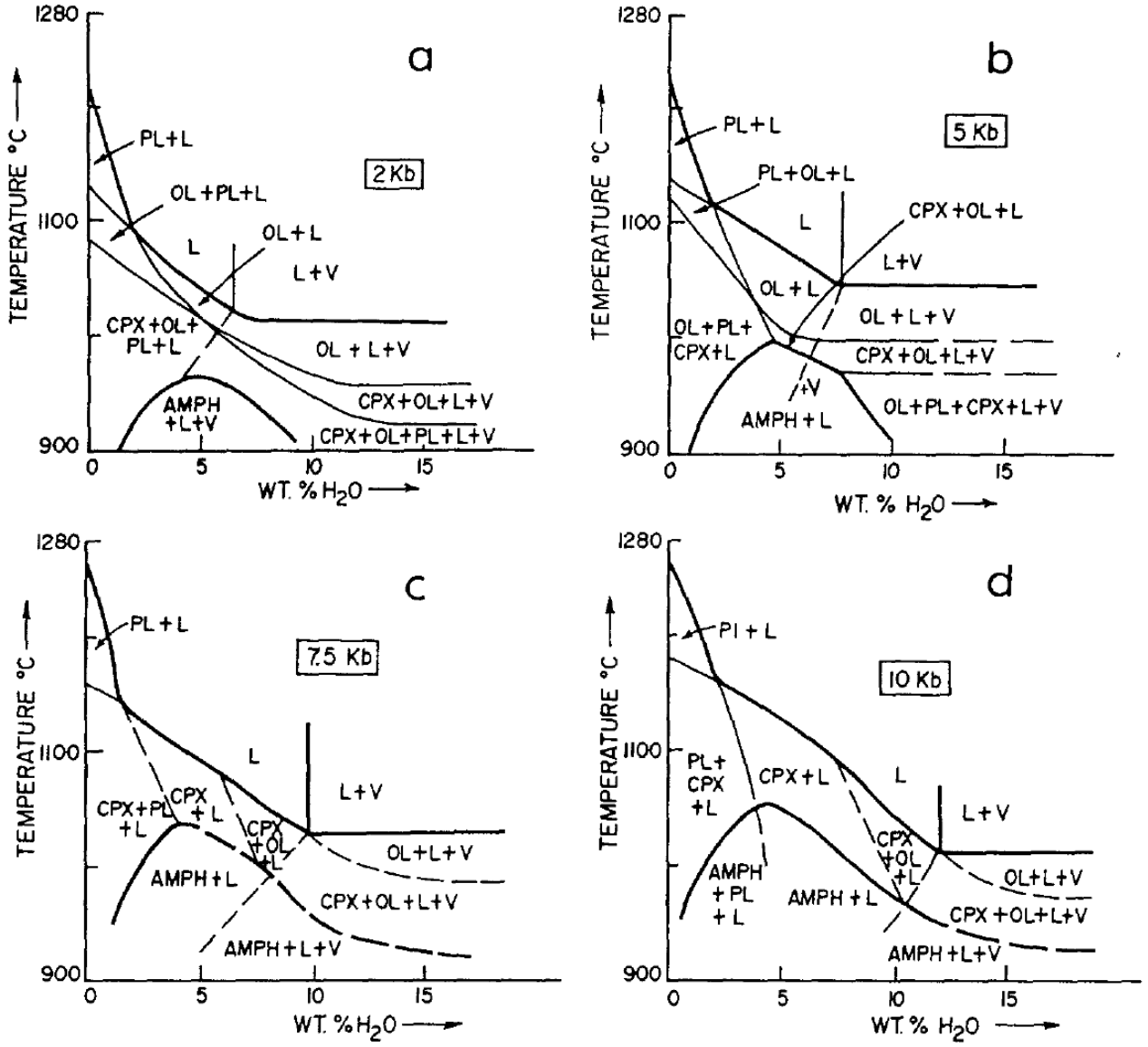

Fig. 2a–d. Summary isobaric T-wt% H_2O sections in the system HAB 41632-H_2O at various pressures. Water quoted as total percentage of the system. The amount of crystallisation in specific runs and calculated H_2O content of the liquid are given in Table 3

Foden 1992

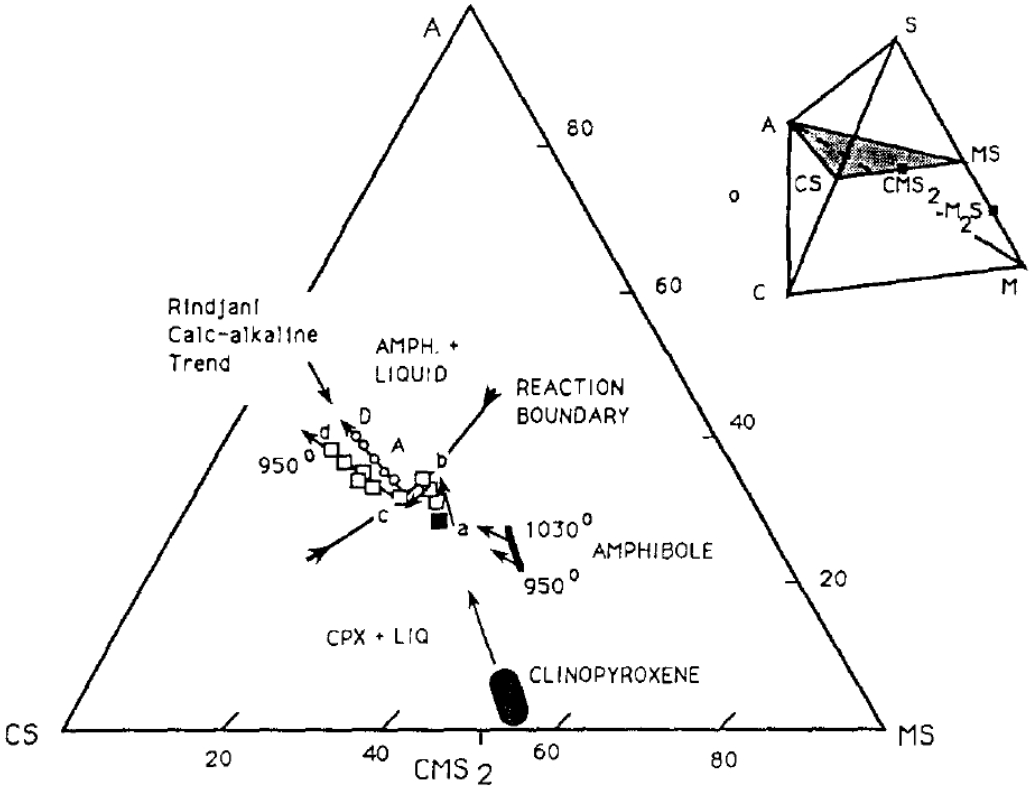

Fig. 5. The compositions of the same 10 kbar experimental liquids as plotted in Fig. 3, plotted in the system CMAS on the A-CS-MS section projected from silica. The *shaded square* is the starting basalt composition, 41632 (Table 1). The fields of synthesized clinopyroxenes and amphiboles are shown with arrows representing the direction of compositional control by these phases on the liquid; clinopyroxene control along segment a–b, buffering on the reaction boundary along segment b–c and amphibole control along segment c–d. The trend defined by circles represents the compositions of typical andesites (*A*) and dacites (*D*) from Rindjani volcano (Foden 1983). Also shown is the inferred position of the reaction boundary between the clinopyroxene + liquid and amphibole + liquid fields and its down-temperature directions

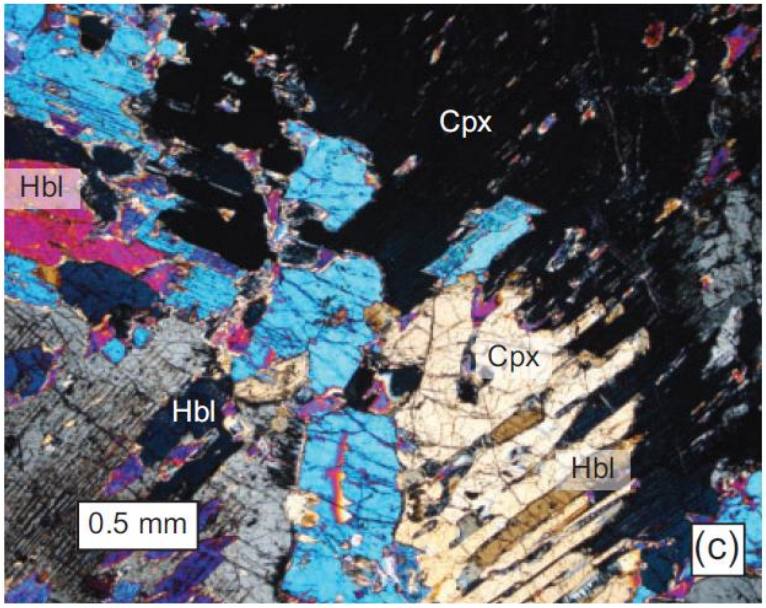

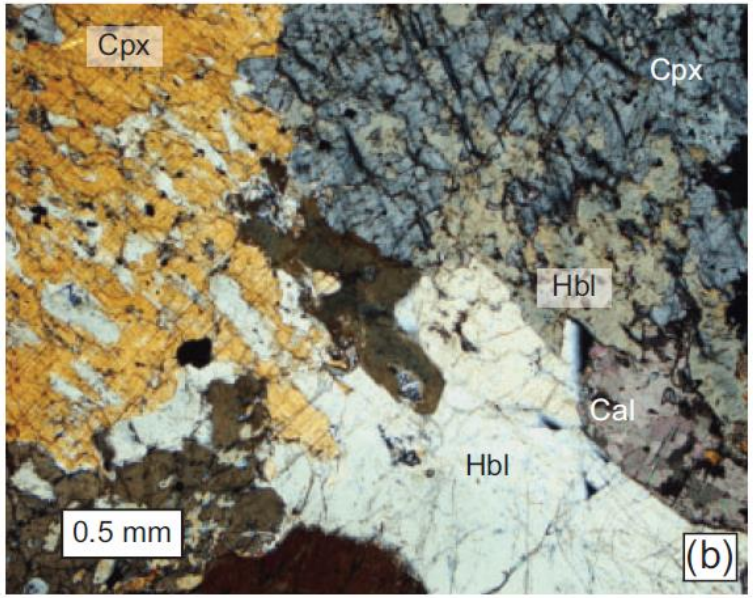

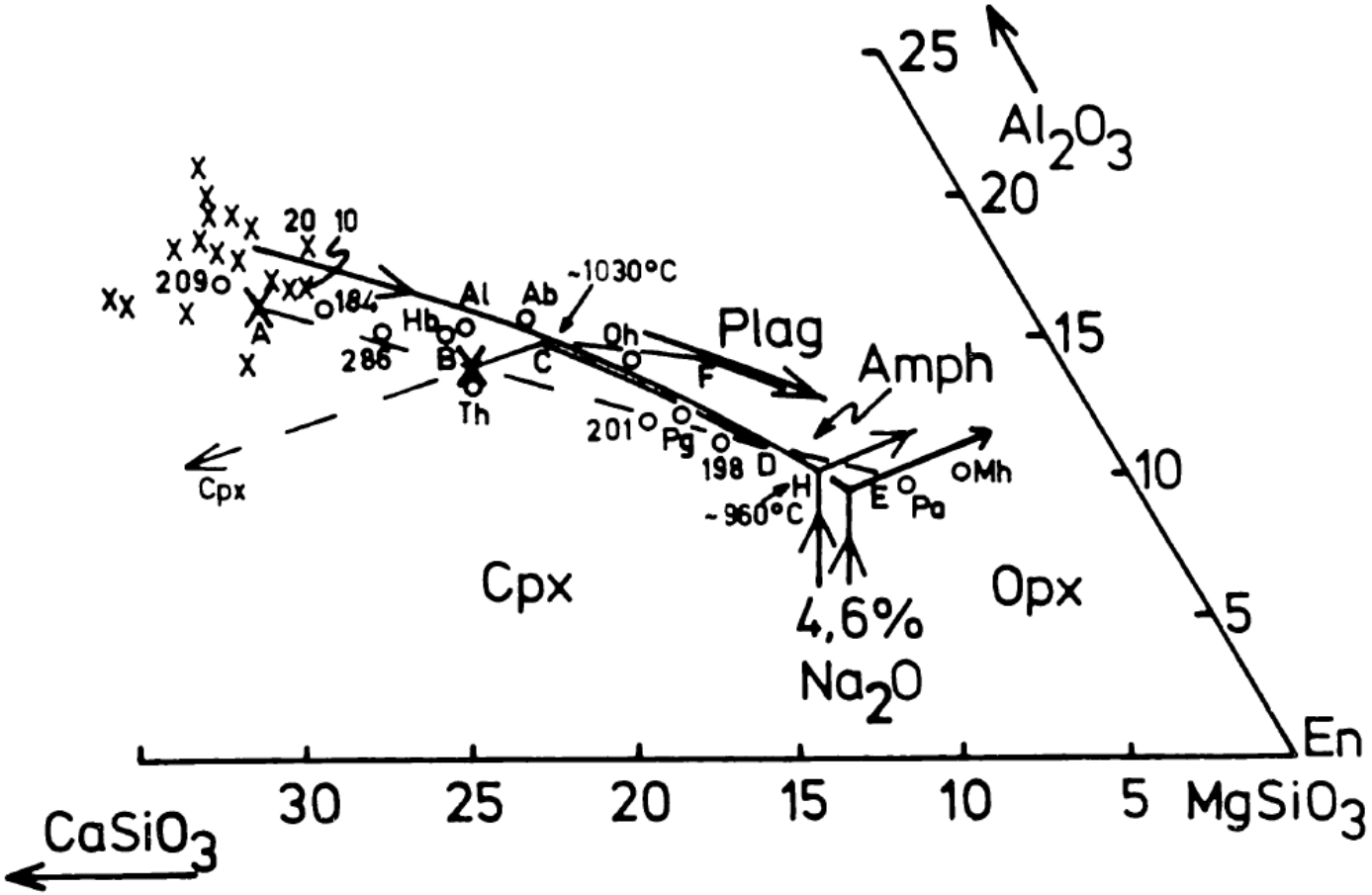

Fig. 2. Weight percent projection from olivine, vapor, and Na_2O into part of the plane $CaSiO_3$–$MgSiO_3$–Al_2O_3 (fig. 1B viewed from the Na_2O apex). Four and six percent Na_2O refer to the phase relations for liquids containing 4 and 6 percent Na_2O respectively. 5 kb hydrous experimental samples, after Yoder and Tilley (1962), Hb—high-alumina basalt; Th—tholeiite; Al—alkali basalt; Oh—oxidized hawaiite. After Helz (1973), PG—Picture George basalt; Ab—alkali basalt. After Cawthorn, Curran, and Arculus (1973), 209 and 184—basanitoids; 286—alkali basalt; 201 and 198—basaltic-andesites. After Eggler (1972a), Pa—Paracutin andesite. After Eggler and Burnham (1973), Mh—Mount Hood andesite. Crosses are amphiboles synthesized by Holloway and Burnham (1972); Eggler (1972b); Helz (1973); Cawthorn, Curran, and Arculus (1973). Amphiboles denoted "10" and "20" were produced at 10 and 20 kb respectively by Green (1973; tables 6 and 12). Liquid evolution trends B–C–D–E–F and points A and H are discussed in the text. Abbreviations as for figure 1.

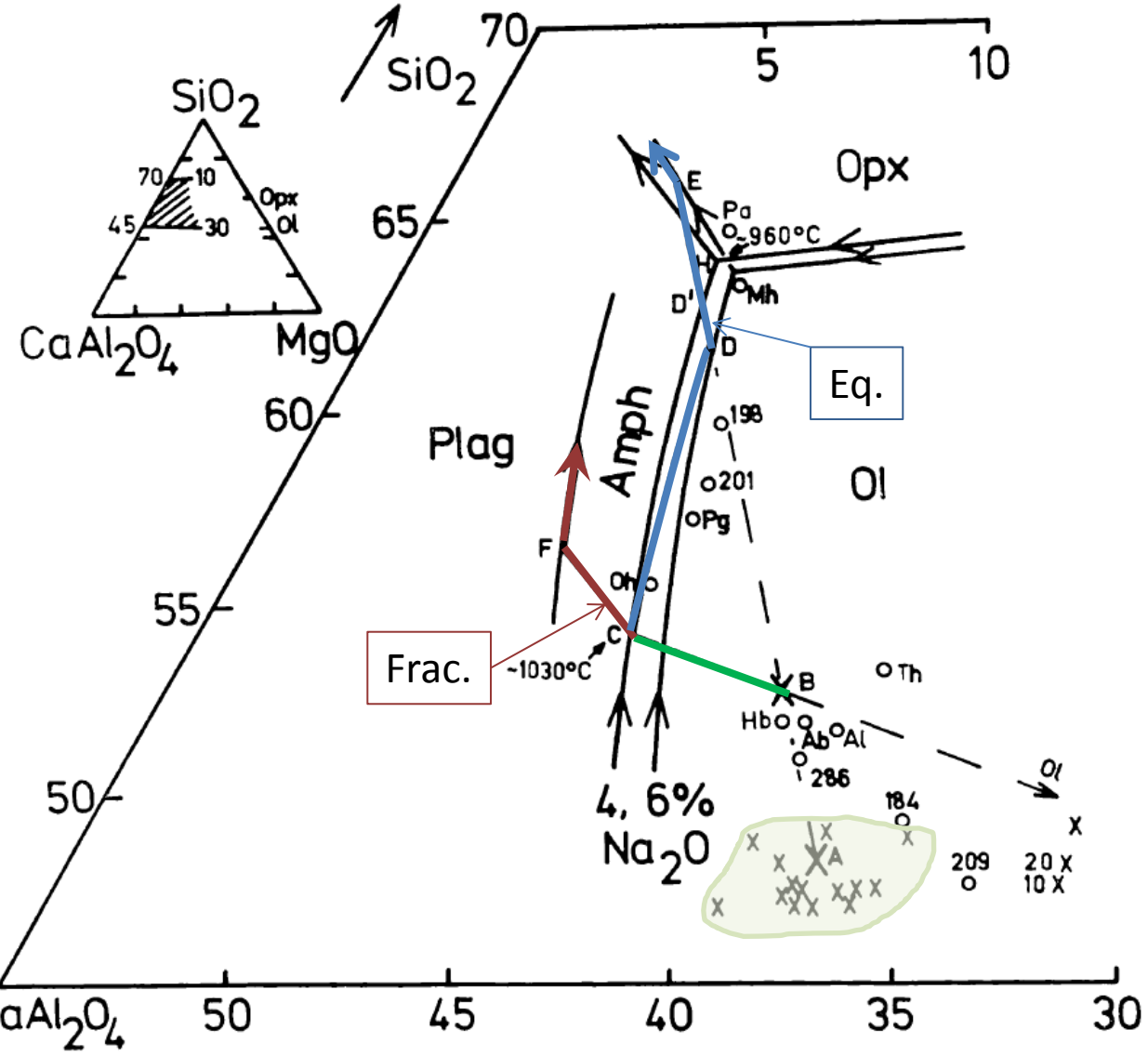

Fig. 3. Weight percent projection from diopside, vapor, and Na_2O into part of the plane $CaAl_2O_4$–MgO–SiO_2 (fig. 1A viewed from the Na_2O apex), shaded inset shows region presented in the main diagram. Explanation as for figure 2.

The major phases of interest in these diagrams are amphibole, orthopyroxene, and either clinopyroxene (in fig. 2) or olivine (in fig. 3). The boundaries between the liquidus fields of these phases have been located accurately in this simple system under 5 kb water pressure. The liquidus field of plagioclase has been less precisely defined in the study of the simple system. A spinel field lies toward the more Al_2O_3-rich region in figure 2 but has not been included, as it is not involved in the following discussion. The loci of the phase boundaries *in these diagrams* are not sensitive to changing Na_2O content from 4 to 6 percent Na_2O. The amphibole–clinopyroxene–olivine–liquid curve for 6 percent Na_2O has not been drawn in full on figure 2, as it coincides with the position of the curve for 4 percent Na_2O. However, two liquids projecting at the same point in these diagrams but containing 4 and 6 percent Na_2O respectively will have quite different normative mineral compositions.

To discuss the main features of the diagrams, consider a bulk composition (B) that contains 3 percent Na_2O in figures 2 and 3. The projection point of (B) is similar to that of tholeiitic basalt (examples of which are projected into figs. 4 and 5). It projects within the primary phase fields of olivine and clinopyroxene, and hence one of these will be the liquidus mineral and the other will precipitate next. By crystallization of these two phases, the residual liquid will migrate along the curve BC, increasing in Na_2O content. At point C, if about 25 percent crystallization has occurred the liquid may contain approximately 4 percent Na_2O, and the phase diagram constructed at this level may be used. (It is possible to calculate exactly the percent crystallinity of the bulk composition when the liquid composition reaches C, by using the lever rule, and hence to determine the Na_2O content of that liquid. However, approximate concentrations are sufficiently accurate for this discussion.)

Two liquid evolution paths are now possible, dependent upon whether fractional or equilibrium crystallization is considered, because there are reaction relationships involved. To test for a reaction relationship between a pair of coexisting phases and liquid, draw a tangent to the two phases-plus-liquid curve toward the tie-line joining the coexisting phase compositions. If the tangent intersects the tie-line between the phase compositions, the phases coprecipitate. If the tangent intersects an extension of the tie-line, the phase farther away from this intersection is in reaction relationship with the liquid. In figure 3 a tangent to the amphibole–olivine–liquid curve would not cut the amphibole–olivine tie-line between the two phases, but on an extension of the tie-line away from olivine. Hence, olivine reacts with liquid to produce amphibole. Likewise in figure 2 a tangent to the amphibole–clinopyroxene–liquid curve would not intersect the amphibole–clinopyroxene tie-line for most amphibole compositions. Hence, clinopyroxene is probably in reaction relationship with liquid to produce amphibole, although coprecipitation is possible.

Under equilibrium crystallization conditions the liquid will migrate along the olivine–clinopyroxene–amphibole–liquid–vapor curve CD precipitating amphibole (A). Olivine and clinopyroxene will be in reaction relationship with the liquid. The composition of amphibole crystallizing in these diagrams may be sensitive to the liquid composition and the nature of the accompanying crystallizing phases (Cawthorn, in press). However, for simplicity an average amphibole composition (A) may be used in this discussion. At point D (the intersection of the line from the amphibole composition (A) through the bulk composition (B) with the olivine–clinopyroxene–amphibole–liquid curve), the olivine and clinopyroxene will have been consumed, and amphibole only will continue crystallizing. (Olivine and clinopyroxene need not necessarily disappear simultaneously. Hence, point D may represent two slightly different compositions in the two diagrams.) The Na_2O content of the liquid will be changing along CD, and at D it may contain up to 6 percent Na_2O. The precise Na_2O content is difficult to estimate unless the Na_2O content of the bulk composition and of the crystallizing amphibole are accurately known. If the liquid did not increase significantly in Na_2O content because of higher Na_2O contents in the amphibole, the liquid composition when all olivine was consumed might be D′, which is not very different from D in figure 3. In figure 2, the olivine–clinopyroxene–amphibole–liquid locus for 4 and 6 percent Na_2O almost coincide, so D and D′ would be the same point.

With subsequent crystallization the liquid will precipitate amphibole alone and hence migrate through the amphibole stability volume along curve DE (directly away from the amphibole composition). The liquid may eventually reach the orthopyroxene stability field, and amphibole and orthopyroxene will coprecipiate. In figures 2 and 3 the clinopyroxene–amphibole–orthopyroxene–liquid and olivine–amphibole–orthopyroxene–liquid curves are presented. These will not be the same as the amphibole–orthopyroxene–liquid curve. Hence, we are not justified in using these diagrams to trace liquid evolution once orthopyroxene begins to crystallize. Point E, the limit for the legitimate use of these diagrams, corresponds to the typical andesite compositions. Hence, we can predict crystallization trends from basaltic compositions through andesitic but not beyond.

Under fractional crystallization conditions, liquids of composition C will crystallize amphibole only and migrate through the amphibole volume away from the amphibole composition along CF. Once the liquid begins to crystallize plagioclase as well as amphibole, these diagrams become strictly invalid. This is because the diagrams show the cotectic curves for amphibole–plagioclase–projection phase–liquid rather than the amphibole–plagioclase–liquid cotectic curve. Hence, the plagioclase field has not been shown in full. However, it may be seen schematically that coprecipitation of amphibole and plagioclase may produce a liquid trend toward andesitic compositions.

The liquid evolution paths, represented here by DE and CF are not necessarily straight. The amphibole composition will probably change as the liquid composition changes, and hence curved paths for DE and CF are more likely. It is not possible to predict changes in amphibole composition from available data, and hence simplified linear paths have been shown.

Gaetani&Grove 1993

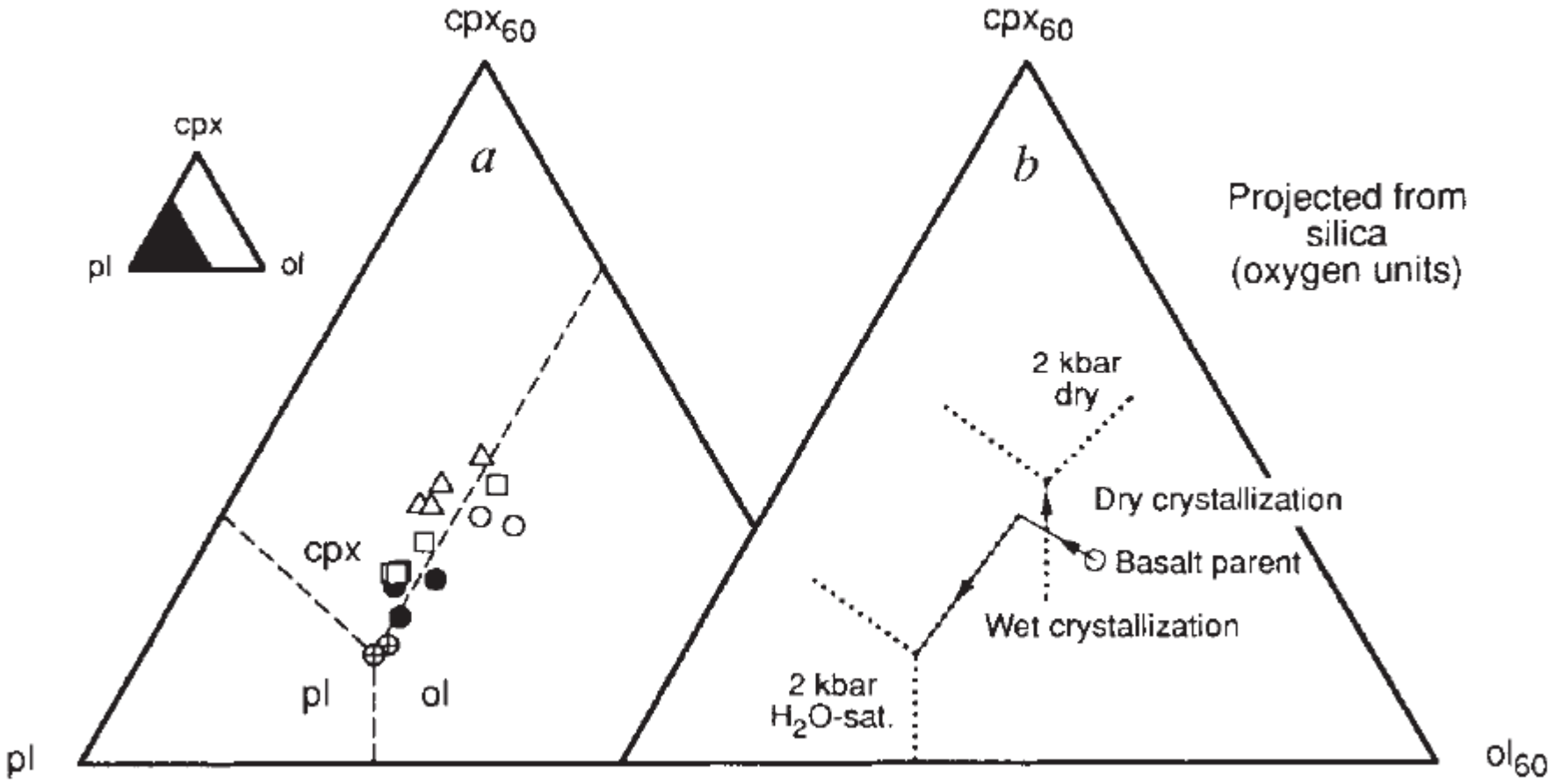

Foden 1992

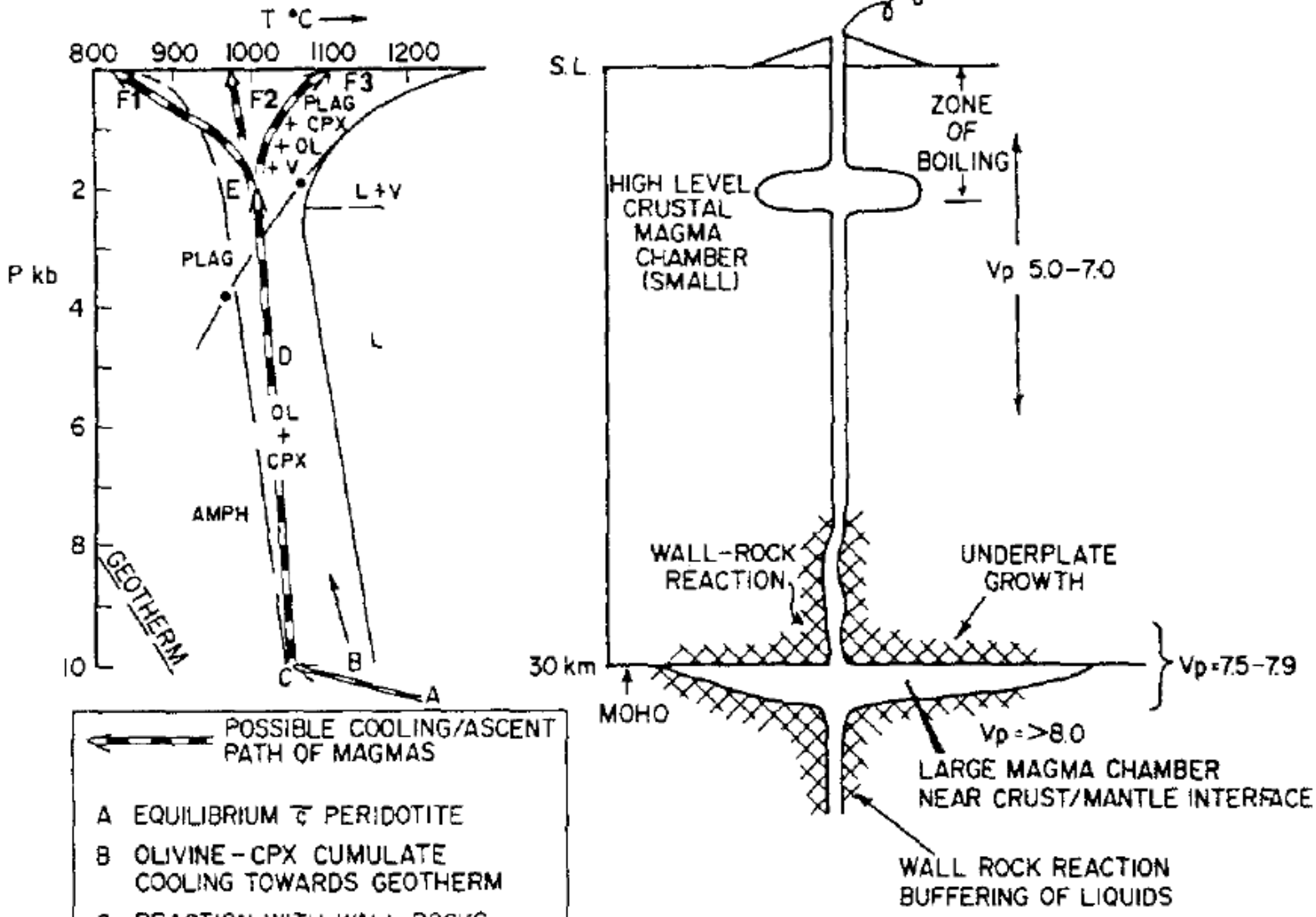

Fig. 7. A summary phase diagram (*left*) for the high-Al basalt system discussed in this paper with 5% H_2O showing possible cooling/ascent paths and the crystallisation products at each stage. The *right hand diagram* indicates a conceptual crustal section of an Indonesian-style (or Japanese, or Aleutian) island-arc

Evolution des magmas andesitiques

Alonso-Perez 2009

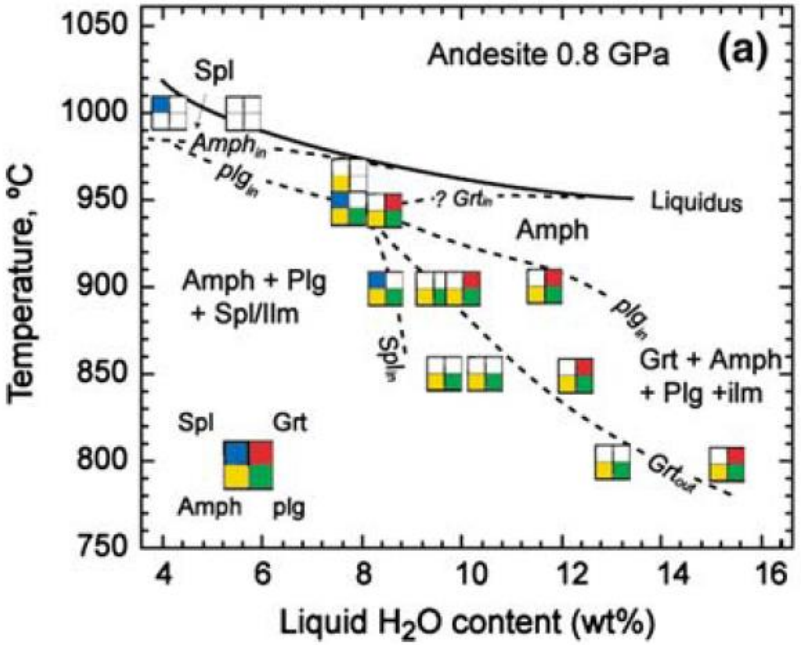

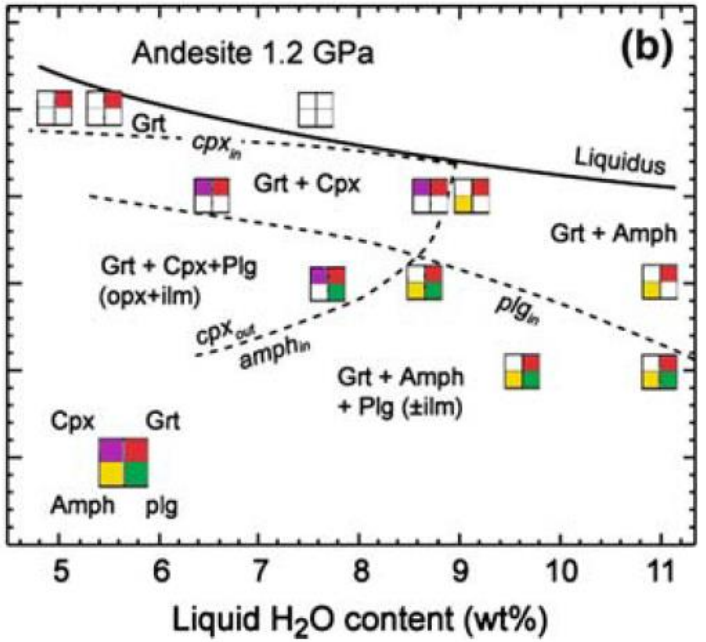

P	1.2	1.2	1.2	1.2	0.8	0.8	1.2	0.8	0.8
H_2O	8	8	6	8	8	8	4	4	4
xtal	0.5	17.6	38.7	35.3	33.1	51.3	60.0	31.7	46.4
ρ	3.81	3.59	3.18	3.29	3.03	3.02	3.10	2.97	2.91
Vp	8.68	8.09	7.24	7.45	7.03	6.99	6.89	6.95	6.86

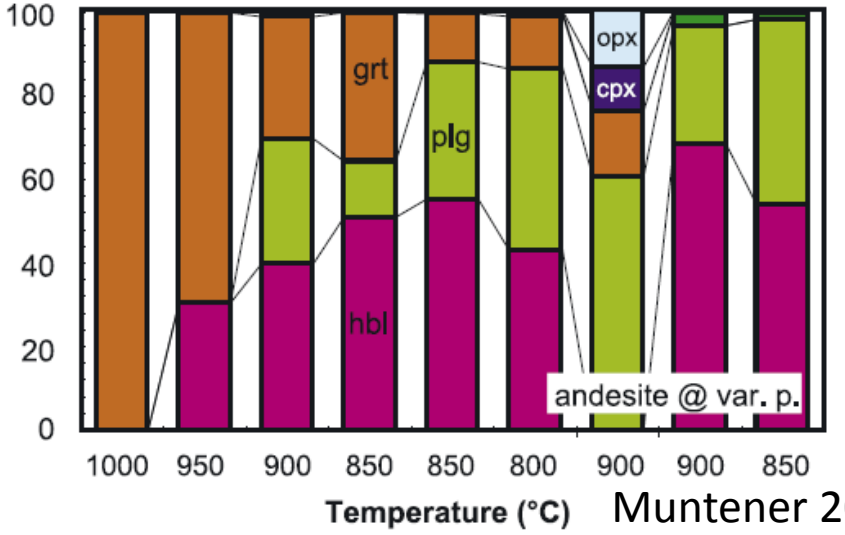

Muntener 2006

Grande variété de Cumulats

Fig. 3 *Phase diagram* showing all water-saturated experiments on the primitive magnesian andesite composition. Phase appearance *lines* for experiments at NNO are thin *black lines*, olivine disappearance is demarcated by a *long-dashed line*, and amphibole stability in NNO+3 experiments are the *short-dashed lines*. Mg# of Fe-Mg phases are also show in numbers next to each experiments, *black* for olivine, *green* for cpx, brown for opx, and *bold italic* for amphibole Mg#s. Amphibole is stabilized to higher T at oxidizing conditions. Above 500 MPa, there is a narrow zone of coexistence between olivine and amphibole and is denoted with a *gray field*

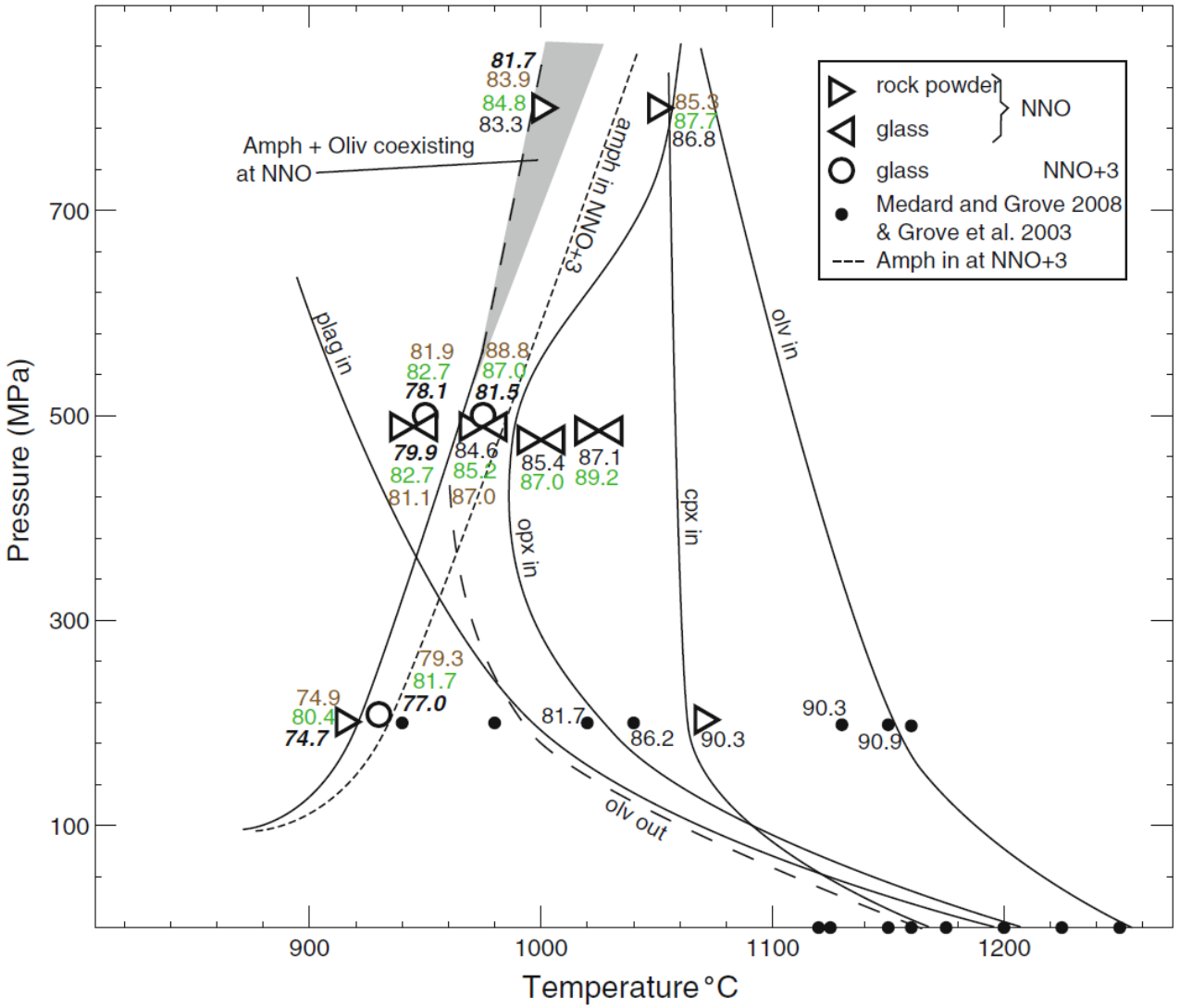

Krawczynski 2012

Evolution des magmas / En Résumé

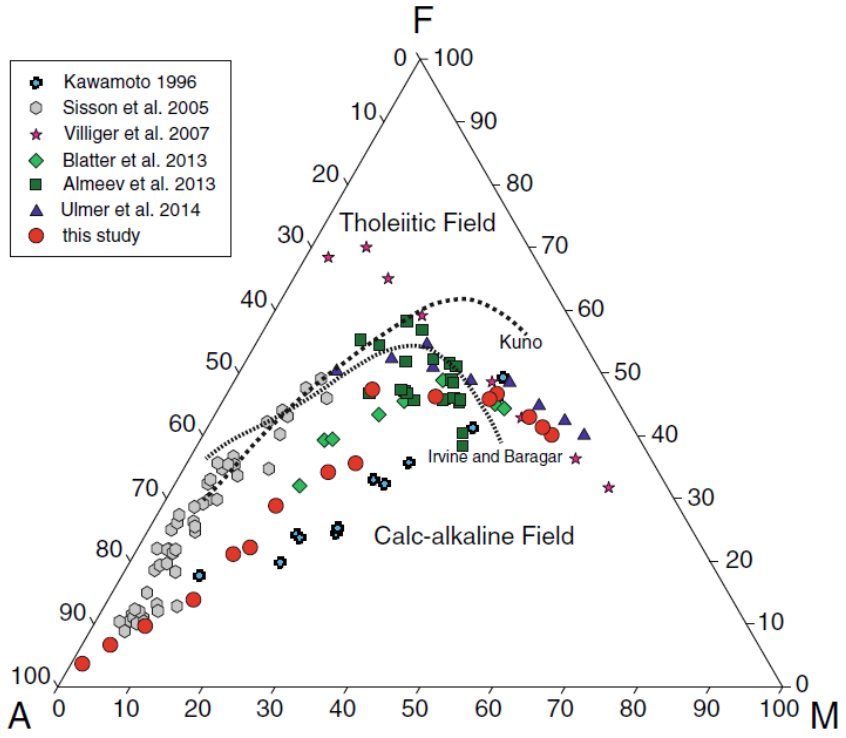

Fig. 9 AFM (A = $Na_2O + K_2O$, F = FeO, M = MgO; wt%) diagram discriminating tholeiitic and calc-alkaline magmatic series. Separation lines according to Kuno (1968) and Irvine and Barager (1971). Data sources and experimental conditions: Kawamoto (1996)—high-alumina basalt, 2 wt% H_2O, equilibrium crystallization, NNO +1.3, 0.5 GPa; Sisson et al. (2005)—basalt, 1.7–2.3 wt% H_2O, equilibrium crystallization, NNO −1.3 to +4, 0.7 GPa; Villiger et al. (2007)—ol–tholeiite, anhydrous, fractional crystallization, C-CO_2, 0.7 GPa; Blatter et al. (2013)—Mg–basalt, 2.1 wt% H_2O, equilibrium crystallization, Re-ReO_2, 0.7 GPa; Almeev et al., (2013)—basaltic andesite, 3.8–10.7 wt% H_2O, equilibrium crystallization, FMQ +2.7 − FMQ +4.1, 0.7 GPa; Ulmer et al. (2014)—picrobasalt, 2.6 wt% H_2O, fractional crystallization, NNO +0.4, 1.0 GPa

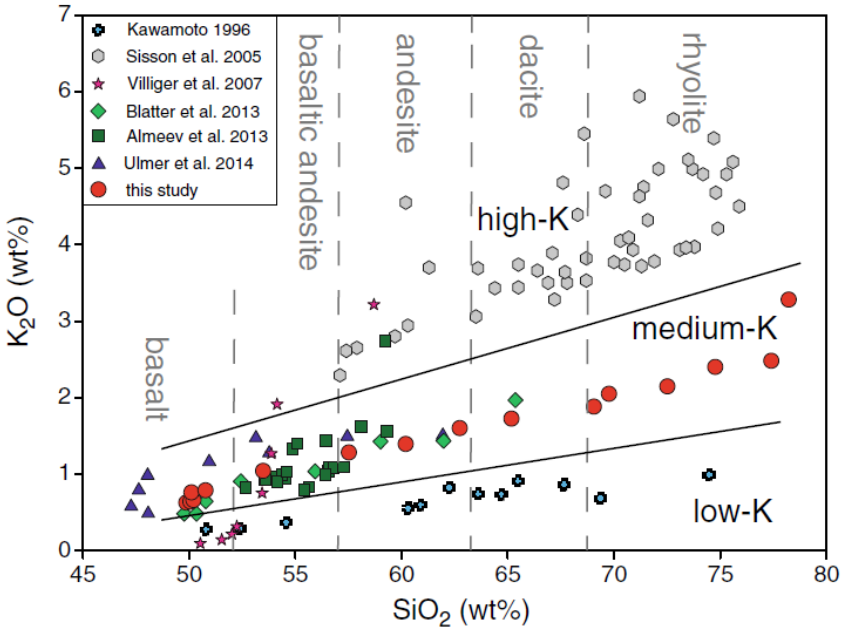

Fig. 10 K_2O–SiO_2 (wt%) diagram to discriminate low-, medium- and high-K calc-alkaline series. Diagram modified after Gill (1981) by extension to higher SiO_2 concentrations. Compositional boundaries of rock names used in this study for liquid compositions are indicated by gray labels and dashed lines. For data sources and experimental conditions, see Fig. 9

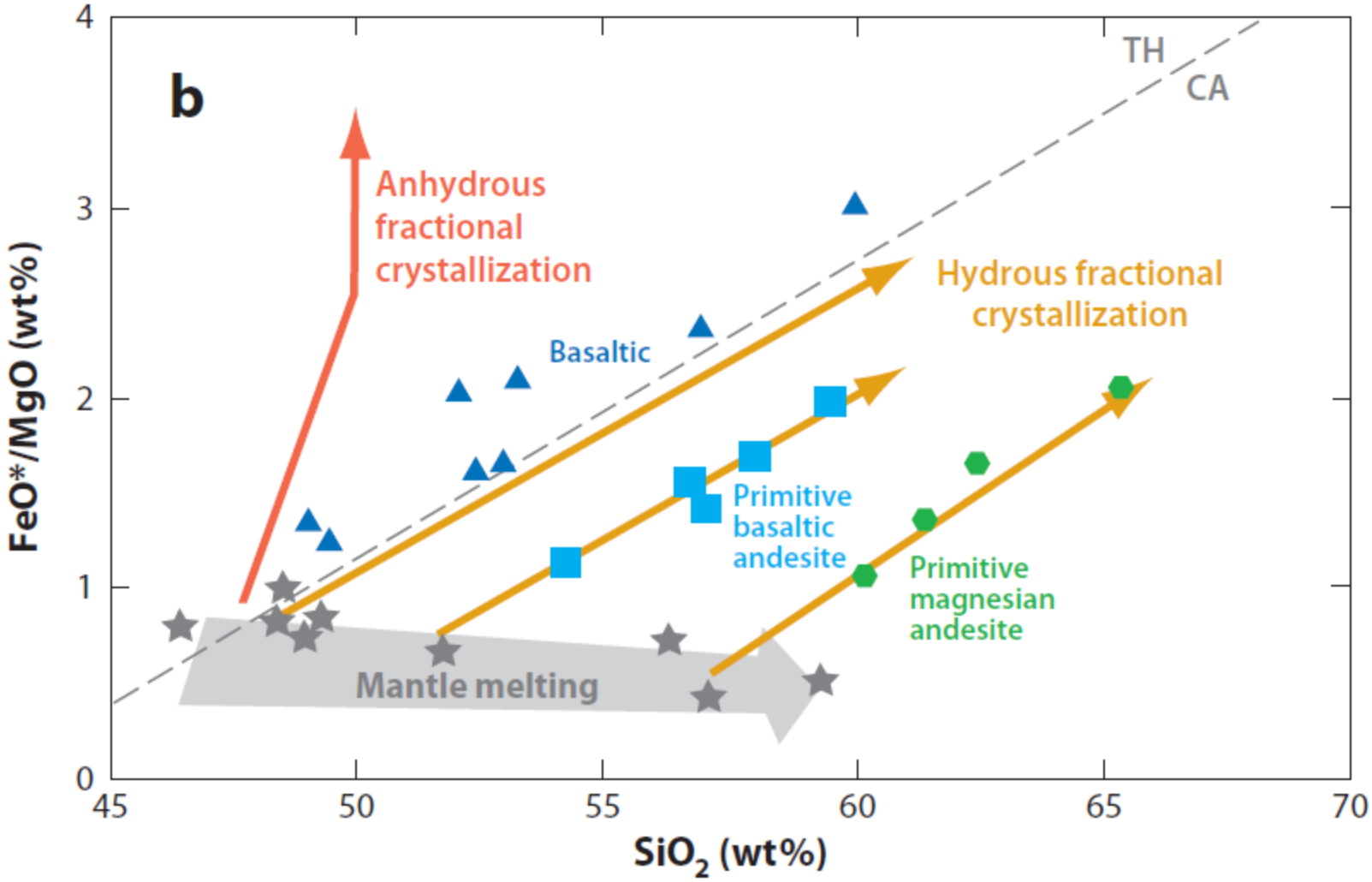
b
TH
CA
Anhydrous
fractional
crystallization
Hydrous fractional
crystallization
Basaltic
Primitive
basaltic
andesite
Primitive
magnesian
andesite
Mantle melting
FeO*/MgO (wt%)
SiO2 (wt%)
0
1
2
3
4
45
50
55
60
65
70

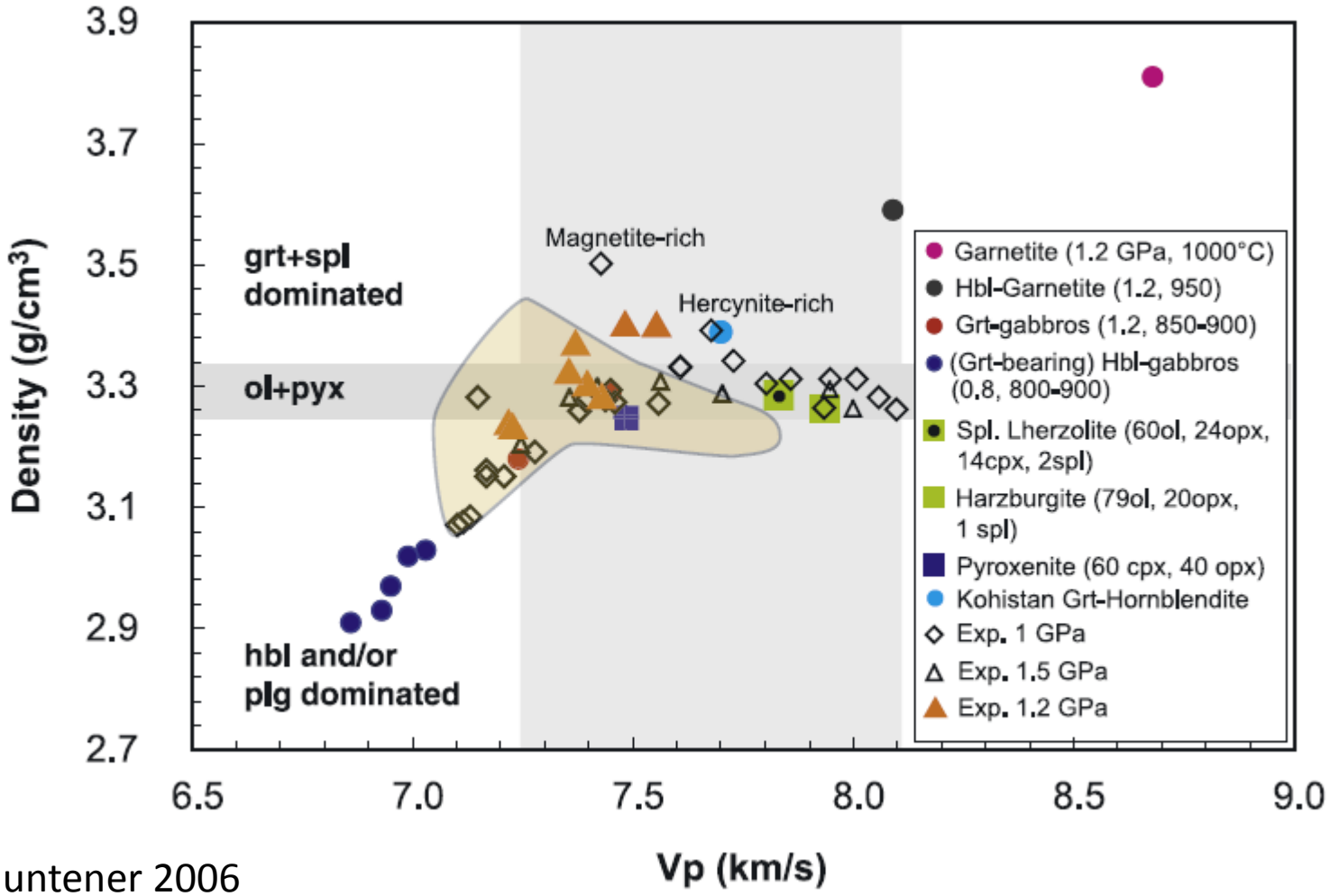

Muntener 2006

Grande varieté de Cumulats, avec des proprietes differentes

Kodaira 2007